

# **Development of the Analysis and Optimization Strategies for Prediction of Residual Stresses Induced by Turning Processes**

**Morteza Sadeghifar**

A Thesis

in the Department of

Mechanical, Industrial, and Aerospace Engineering

Presented in Partial Fulfilment of the Requirements

for the Degree of

**Doctor of Philosophy (Mechanical Engineering) at**

**Concordia University**

**Montreal, Quebec, Canada**

**July 2017**

© Morteza Sadeghifar, 2017

**CONCORDIA UNIVERSITY**  
**SCHOOL OF GRADUATE STUDIES**

This is to certify that the thesis prepared

By: Morteza Sadeghifar

Entitled: Development of the Analysis and Optimization Strategies for Prediction of Residual Stresses Induced by Turning Processes

and submitted in partial fulfillment of the requirements for the degree of

**Doctor of Philosophy (Mechanical Engineering)**

complies with the regulations of the University and meets the accepted standards with respect to originality and quality.

Signed by the final examining committee:

_____	Chair
Dr. Zhi Chen	
_____	External Examiner
Dr. Kamran Behdinan	
_____	External to Program
Dr. Amir Aghdam	
_____	Examiner
Dr. Ion Stiharu	
_____	Examiner
Dr. Sivakumar Narayanswamy	
_____	Thesis Co-Supervisor
Dr. Ramin Sedaghati	
_____	Thesis Co-Supervisor
Dr. Victor Songmene	

Approved by \_\_\_\_\_  
Dr. Ali Dolatabadi, Graduate Program Director

Thursday, August 31, 2017

\_\_\_\_\_  
Dr. Amir Asif, Dean  
Faculty of Engineering and Computer Science

## **Abstract**

### **Development of the Analysis and Optimization Strategies for Prediction of Residual Stresses Induced by Turning Processes**

**Morteza Sadeghifar, Ph.D.**

**Concordia University, 2017**

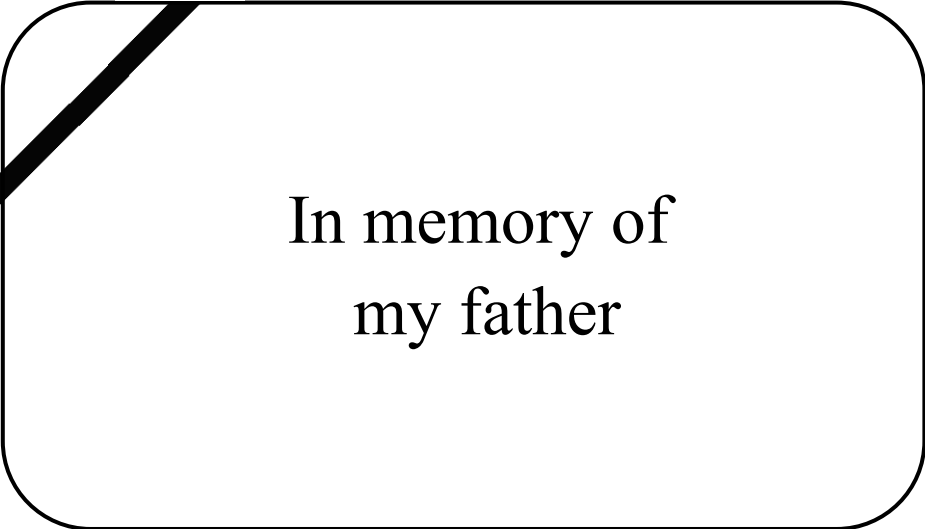
Difficult-to-machine materials are widely used in the aerospace and automotive industries including landing gears of aircrafts, drive-shafts of automobiles, and high strength bolts and frame parts of airplanes and motorsports due to their high toughness, less sensitivity to heat, and high resistance to fatigue and corrosion. Machining these materials is accompanied by high cutting temperatures and forces, which cause high residual stresses. It is known that high temperature leads to inaccuracies in component dimensions and causes phase transformation in the material. High cutting forces also raise the power consumption of turning machines and result in an excessive deflection and consequently breakage of the tool. Also, both large cutting temperatures and forces cause high tool wear. Most importantly, machining-induced tensile residual stresses have detrimental effects on the performance of components due to having the tendency to open tiny cracks and speed up crack propagation, which subsequently results in decreasing the resistance to fatigue and corrosion. In contrast, high compressive residual stresses have beneficial effects as they tend to close cracks and slow down crack propagation, which consequently increases the fatigue life considerably. The machining process is required to be efficient by removing as large amount of material as possible, meaning to have a high material removal rate.

Machining forces, temperature, residual stresses, and material removal rate depend highly on machining parameters including cutting conditions and tool geometry. Therefore, a thorough optimization study is required to be conducted to identify optimal machining parameters including cutting speed, feed rate, edge radius, rake angle, and clearance angle to improve response variables specially residual stresses, which will be highly desirable and of paramount importance to the industry. More particularly, when the optimization is carried out based on Finite Element Method

(FEM), by which the expensive, time-consuming process of experimental tests is avoided, the outcome will be more economical for the industry.

Finite Element (FE) modeling of orthogonal turning is considered as an open-ended subject as most of the phenomena involved in the orthogonal turning, which also exist in other machining operations, are not fully understood. In the present research work, first, a predictive high-fidelity finite element model is developed using Abaqus software to obtain response variables of cutting temperature, machining forces, and residual stresses induced by orthogonal turning 300M Steel. The validity of the developed FE model is then verified by comparing the predicted machining forces, chip thickness, and residual stresses with those of experimental tests obtained in turn using a piezoelectric dynamometer, a digital micrometer, and 'X-Ray diffraction apparatus, electropolishing equipment, and a profilometer machine'. The FE model is then utilized to systematically derive response functions (Meta or surrogate models) for desired FE outputs using D-optimal Design of Experiment (DoE) and Response Surface Method (RSM). The derived response functions explicitly relate the desired responses to identified design parameters, and therefore, can be effectively utilized for design optimization problems without using the FE model. Finally, multi-criteria optimization problems are formulated to reduce superficial residual stresses individually and improve a combination of residual stresses, cutting temperature, cutting and thrust forces, and material removal rate by obtaining optimum values of machining parameters including cutting speed, feed rate, edge radius, rake angle, and clearance angle. Special attention is devoted to minimizing the machining-induced residual stresses. Optimization is conducted using a hybrid method of Genetic Algorithm (GA) and Sequential Quadratic Programming (SQP) technique in order to accurately capture the global optimum values of machining parameters and response variables. The optimization results show considerable improvement in the total objective function and especially residual stresses.

Since there are no research studies on the finite element simulation, experimental test, and most importantly, constrained and unconstrained multi-performance optimization of machining characteristics and residual stresses for radial turning of 300M steel, the results of the present research can be utilized as a reference for future works along this field.



In memory of  
my father

## **Acknowledgements**

First of all, I would like to thank my supervisor, Professor Ramin Sedaghati, for his encouragement, valuable guidance, and continuous technical and financial supports throughout my research at Concordia University. It has been a great honor for me to work as his doctoral student for several years. In addition, I express my sincere gratitude to my Co-supervisor, Professor Victor Songmene at École de Technologie Supérieure, for his technical support during my PhD project. Conducting research under their supervisions was an invaluable experience for me.

Also, I would like to extend my appreciation to my thesis committee members, Professor Kamran Behdinin, Professor Amir G. Aghdam, Professor Ion Stiharu, and Professor Sivakumar Narayanswamy, for providing useful suggestions and constructive discussions in my PhD defense.

This PhD research project was conducted as a part of the industrial project entitled CRIAQ MANU510. I highly appreciate Consortium de Recherche et d'Innovation en Aérospatiale au Québec (CRIAQ), Natural Sciences and Engineering Research Council of Canada (NSERC), and particularly, companies Pratt & Whitney Canada (P&WC) and Héroux-Devtek Inc. (HD) as the industrial collaborators and sponsors, for funding my PhD research project. I also acknowledge the afore-mentioned companies for supplying component materials, inserts, and tool holders.

I extend my sincere thanks to the industrial partners and also professors, from Concordia University, École Polytechnique de Montréal, École de Technologie Supérieure, and McGill University, involved in MANU510 project for valuable and constructive discussions during the bi-annual meetings we had.

Many thanks go to Dr. Walid Jomaa, the research associate working as the machining and surface integrity expert in MANU510, who provided me with priceless comments and discussions. In addition, I am grateful to my teammates in MANU510. We had a large number of monthly student meetings full of useful discussions and challenges.

I would like to express my appreciation to Professor Phillippe Bocher at École de Technologie Supérieure for providing me with the advanced Pulstec and Proto XRD machines in his lab for measuring residual stresses. I also thank Dr. Yaser Zedan, the research associate at École de Technologie Supérieure, for his valuable technical instructions on working with X-Ray Diffraction, Electroplishing, and profilometer machines.

My appreciation extends to my friends and officemates at Concordia University, who made the university an enjoyable academic environment for me. I had many memorable moments with them. I would also like to acknowledge all the administrative staff in the Department of Mechanical, Industrial, and Aerospace Engineering (MIAE), especially Mrs. Leslie Hossein, the graduate program coordinator in MIAE, for her assistance with the administrative matters of PhD students. She is very competent, patient, and responsible. I sincerely thank Dr. Peter Tzenov, the laboratory coordinator in MIAE, for assigning me as a teaching assistant for several courses during the course of my PhD study. This job augmented my teaching experience considerably.

Finally, and most importantly, special thanks to my family. Words cannot express how grateful I am to my beloved mother, sisters, and brothers for their affection, endless love and encouragement. They have always been inciting me to strive towards my goal and been supporting me, unconditionally and continuously, throughout my life.

*To my beloved family*

## Table of Contents

<b>List of Figures</b> .....	<b>xii</b>
<b>List of Tables</b> .....	<b>xv</b>
<b>List of Abbreviations</b> .....	<b>xvii</b>
<b>List of Symbols</b> .....	<b>xix</b>
<b>CHAPTER 1 Research Objectives and Thesis Scope</b> .....	<b>1</b>
1.1. Motivation .....	1
1.2. Research objectives .....	3
1.3. Thesis outline .....	3
<b>CHAPTER 2 Research Background</b> .....	<b>6</b>
2.1. Introduction .....	6
2.2. Orthogonal machining .....	6
2.3. Finite element prediction of machining characteristics and residual stresses ....	9
2.3.1. <i>Chip morphology and tool-chip contact length</i> .....	9
2.3.2. <i>Machining forces</i> .....	11
2.3.3. <i>Cutting temperature</i> .....	14
2.3.4. <i>Residual stresses</i> .....	17
2.4. Optimization studies .....	26
<b>CHAPTER 3 Finite Element Modelling</b> .....	<b>28</b>
3.1. Introduction .....	28
3.2. Underlying concepts and methods in finite element modeling of orthogonal machining .....	28
3.2.1. <i>Geometrical modelling</i> .....	28
3.2.2. <i>Mechanical modelling and analysis</i> .....	30
3.2.3. <i>Thermal modelling and analysis</i> .....	31
3.2.4. <i>Material modelling</i> .....	34
3.2.5. <i>Frictional modelling</i> .....	37
3.2.6. <i>Chip formation modelling</i> .....	40
3.2.7. <i>Thermo-mechanical coupling</i> .....	42
3.2.8. <i>Finite element formulations</i> .....	42

3.2.9.	<i>Explicit and Implicit solvers</i> .....	43
3.3.	Comparison of commercial software and input models and materials .....	44
3.4.	Sources of error .....	58
3.5.	The present finite element modeling .....	59
3.5.1.	<i>Modeling, element, mesh, and boundary conditions</i> .....	59
3.5.2.	<i>Numerical integration and time increment</i> .....	61
3.6.	Optimal magnitudes of numerical parameters .....	63
3.6.1.	<i>Size and arrangement of elements</i> .....	63
3.6.2.	<i>Adaptive meshing</i> .....	65
3.6.3.	<i>Mass scaling</i> .....	67
<b>CHAPTER 4</b>	<b>Experimental Tests</b> .....	<b>68</b>
4.1.	Introduction .....	68
4.2.	Machining and cutting force measurements .....	68
4.3.	Residual stress measurements .....	71
4.3.1.	<i>Principles of X-Ray Diffraction Method</i> .....	71
4.3.2.	<i>Pulstec and Proto machines for residual stress measurements</i> .....	74
4.4.	Electropolishing method .....	76
4.5.	P-profile measurements .....	77
<b>CHAPTER 5</b>	<b>Regression Analysis and Optimization Strategy</b> .....	<b>79</b>
5.1.	Introduction .....	79
5.2.	D-optimal Design of Experiment .....	79
5.3.	Response surface method .....	80
5.4.	Genetic Algorithm .....	82
5.5.	Sequential Quadratic Programming Method .....	83
5.6.	Optimization strategy .....	84
5.7.	Solution procedure .....	85
<b>CHAPTER 6</b>	<b>Discussion of Results</b> .....	<b>88</b>
6.1.	Introduction .....	88
6.2.	Validation of the finite element model .....	88
6.3.	Explicit functions of response variables .....	93

6.4.	Multi-objective optimization problem formulation .....	100
6.5.	Optimization results .....	102
6.5.1.	<i>Optimization of residual stresses</i> .....	102
6.5.2.	<i>Optimization of residual stresses, cutting temperature, machining forces, and material removal rate</i> .....	109
<b>CHAPTER 7</b>	<b>Conclusions, Contributions, Future Works, and Outlook .....</b>	<b>112</b>
7.1.	Introduction .....	112
7.2.	Summary and conclusions .....	112
7.3.	Contributions .....	116
7.4.	Future works .....	119
7.5.	Recommendations for future works .....	120
7.6.	Outlook .....	121
<b>References</b>	<b>.....</b>	<b>122</b>

## List of Figures

Fig. 2-1. Applications of orthogonal turning [8] .....	7
Fig. 2-2. Experimental (a) disc-shaped [16] (b) tube-shaped [33] component set-up configuration of orthogonal turning .....	8
Fig. 2-3. Variation of (a,b) the cutting and feed forces with feed, and the cutting force with (c) tool edge radius and (d) rake angle, for materials AISI 52100, AISI H13, AISI D2, and AISI 4340 steels [79] .....	12
Fig. 2-4. A comparison between (a) the measured temperature profile and (b) the predicted one using DEFORM software, during cutting AISI 316L [11] .....	15
Fig. 2-5. Predicted temperature fields using Abaqus/Explicit for different shear stress limits: (a) unlimited, (b) 200 MPa, (c) 500 MPa, and (d) 700 MPa [16] .....	16
Fig. 2-6. The mechanisms of creation of residual stresses [92,93] .....	19
Fig. 2-7. The ways of residual stress extraction from a FE model .....	21
Fig. 2-8. The influence of (a) cutting speed (using the TiC/Al <sub>2</sub> O <sub>3</sub> /TiN coated carbide tool), (b) uncut chip thickness (feed), (c) rake angle and (d) edge radius on circumferential residual stresses [11] .....	23
Fig. 2-9. Effect of tool edge radius (a) on the tensile residual stress in the cutting direction (RS11) at different depths, (b) on in-depth residual stress RS11 [49] .....	24
Fig. 2-10. The variation of the maximum value of residual stresses in the cutting (circumferential) S11 and feed (axial) S22 directions with (a,b) cutting speed and (c,d) feed [32] .....	25
Fig. 3-1. Identification of tool geometry for FE modeling .....	29
Fig. 3-2. Influence of heat fraction $R_T$ on (I) temperature (°C) and (II) von Mises stress (Pa) distributions: (a) $R_T=0$ , (b) $R_T=0.4$ , and (c) $R_T=1$ [33] .....	33
Fig. 3-3. Comparisons of measured and predicted (a) axial and (b) circumferential residual stresses (cutting speed $V=200$ m/min, uncut chip thickness $b=0.1$ mm, width of cut $a_p=6$ mm) [57] .....	37
Fig. 3-4. Schematic distribution of shear stress on the tool rake face based on Zorev model provided in Table 3-2 .....	38

Fig. 3-5. The tree diagram summarizing the methods used for chip formation modelling .....	41
Fig. 3-6. Thermal and mechanical boundary conditions during the cutting process .....	60
Fig. 3-7. Arrangement of elements along the length and width of a rectangular workpiece .....	64
Fig. 3-8. Remeshing schemes: (a) original mesh, (b) r-adaptively: relocating the nodes, and (c) h-adaptively: reducing the size of elements .....	66
Fig. 4-1. Mazak CNC lathe used for machining of samples .....	69
Fig. 4-2. Directions of cutting and thrust forces in (a) the experiment and (b) the FE model .....	69
Fig. 4-3. (a) Measurement of circularity profile of the specimen using a coordinate measuring machine and (b) the circularity profile and valid zone required for residual stress measurements .....	70
Fig. 4-4. X-Ray waves: (a) Constructive interference and (b) Destructive interference...	72
Fig. 4-5. Bragg's law [143] .....	72
Fig. 4-6. (a) Pulstec $\mu$ -X360n equipment versus (b) Proto iXRD apparatus.....	75
Fig. 4-7. Electropolishing process.....	77
Fig. 4-8. P-profile measurement .....	78
Fig. 5-1. Optimization problem strategy: (a) an illustrative example and (b) a flowchart of the GA-SQP method .....	86
Fig. 5-2. The flowchart showing the solution procedure .....	87
Fig. 6-1. Variation of cutting and thrust forces with time during the cutting process (for 4.5-mm width of cut): (a) in experiment (Force signals) and (b) in FE modeling .....	90
Fig. 6-2. The distribution of cutting temperature in the workpiece and tool for the steady-state condition .....	91
Fig. 6-3. The predicted circumferential residual stresses versus the experimental ones ...	92
Fig. 6-4. FE predictions of cutting temperature for 27 design points in DoE .....	96
Fig. 6-5. FE predictions of cutting force for 27 design points in DoE .....	96
Fig. 6-6. FE predictions of thrust force for 27 design points in DoE .....	97

Fig. 6-7. FE predictions of superficial residual stress for 27 design points in DoE ..... 97

Fig. 6-8. FE predictions of material removal rate for 27 design points in DoE ..... 98

Fig. 6-9. Influence of cutting speed on cutting forces: (a) via affecting the frictional and plastic works, where  $F_f$  is frictional force,  $V_c$  cutting velocity,  $\sigma$  flow stress,  $\dot{\epsilon}$  strain rate, and  $W$  the work done, and (b) via affecting material removal rate and strain rate .... 107

Fig. 6-10. Competing effects of feed on cutting forces ..... 108

## List of Tables

Table 3-1 Material constitutive models utilized in FE modeling of orthogonal machining ( $\varepsilon$ : strain, $\dot{\varepsilon}$ : strain rate, $T$ : temperature) .....	35
Table 3-2 Friction models frequently employed in FE simulations of machining processes .....	38
Table 3-3 Explicit and Implicit time integration solvers .....	43
Table 3-4 Finite element software packages utilized in metal cutting simulations .....	44
Table 3-5 A summary of FE studies simulating the cutting process of orthogonal turning of metals .....	46
Table 3-6 A summary of FE studies simulating both cutting and stress relaxation processes of orthogonal turning of metals .....	55
Table 3-7 Comparison of the required features for modeling a rigid tool .....	59
Table 4-1 Constants and parameters for residual stress measurements using a Pulstec machine .....	75
Table 6-1 Comparison of average cutting force $F_c$ , thrust force $F_t$ , and chip thickness $t_c$ .....	89
Table 6-2 Cutting conditions and tool geometry .....	89
Table 6-3 Mechanical and thermal properties of the workpiece and tool .....	89
Table 6-4 Constants of Johnson-Cook material model of 300M steel [158] .....	89
Table 6-5 Factors and levels used for design of experiment .....	93
Table 6-6 Machining Parameters (MPs) using D-optimal DoE .....	95
Table 6-7 Regression coefficients and coefficients of determination $R^2$ for the quadratic functions of cutting temperature, machining forces, and residual stresses .....	99
Table 6-8 The upper and lower bounds of the design variables in the optimization process .....	101
Table 6-9 Optimum values of machining parameters and objective and constraint functions .....	104
Table 6-10 Weighting coefficients of the individual objective functions for multi-objective optimization of residual stresses, cutting temperature, machining forces, and material removal rate .....	110

Table 6-11 Optimum values of machining parameters and the corresponding objective and constraint functions ..... 111

## List of Abbreviations

ALE	Arbitrary Lagrangian Eulerian
BCs	Boundary Conditions
BFGS	Broyden-Fletcher-Goldfarb-Shanno
CCD	Central Composite Design
CF	Constraint Function
CMM	Coordinate Measuring Machine
DoE	Design of Experiment
E	Eulerian
FE	Finite Element
FEA	Finite Element Analysis
FEM	Finite Element Method
GA	Genetic Algorithm
GSS	Golden Section Search
HSM	High Speed Machining
J-C	Johnson-Cook
mJ-C	modified Johnson-Cook
MRR	Material Removal Rate
mZ-A	modified Zerilli-Armstrong
OF	Objective Function
OM	Orthogonal Machining
PCBN	Polycrystalline Cubic Boron Nitride
PCD	Polycrystalline Diamond
PL	pure Lagrangian
QP	Quadratic Programming
RS	Residual Stress

RSM	Response Surface Method
SA	Simulated Annealing
SEM	Scanning Electron Microscopy
SHPB	Split Hopkinson Pressure Bar
SQP	Sequential Quadratic Programming
UL	updated Lagrangian
XRD	X-Ray Diffraction

## List of Symbols

$A$	Initial yield strength in J-C model
$B$	Hardening modulus in J-C model
$b$	body force
$C$	Strain rate sensitivity coefficient in J-C model
$C_d$	Damping matrix
$C_T$	Volumetric heat capacity matrix
$c$	Specific heat capacity
$c_d$	Dilatational wave speed
$d$	Lattice spacing of crystal planes
$d_0$	Lattice spacing of stress-free state of material
$E$	Young's modulus of elasticity
$E_f$	Thermal effusivity
$F_c$	Cutting force
$F_t$	Thrust force
$f$	feed rate
$h$	Convection heat transfer coefficient
$h_{\text{int}}$	Thermal conductance coefficient
$K_s$	Stiffness matrix
$K_T$	Thermal conduction matrix
$k$	Thermal conductivity
$L_{\text{min}}$	Smallest element dimension in model
$l_p$	Length of sticking region

$l_c$	Tool-chip contact length
$M$	Mass matrix
$m$	Thermal softening coefficient in J-C model ; Shear friction factor
$n$	Hardening coefficient in J-C model ; Order of diffraction in Bragg's law
$OF_{optimum}$	Optimum value of total objective function
$OF_{smallest}$	Smallest value of total objective function in 27 design points
$\dot{Q}_g$	Heat generation in machining process
$R_{ext}$	External force vector
$R_{int}$	Internal force vector
$R^2$	Coefficient of determination
$r_\beta$	Edge radius
$T$	Temperature
$T_m$	Melting temperature
$T_{room}$	Room temperature
$t$	Time ; Tool
$t_c$	Chip thickness
$\dot{T}$	Temperature rate
$U$	Material displacement vector
$\dot{U}$	Material velocity vector
$\ddot{U}$	Material acceleration vector
$V$	Cutting speed
$V_{ch}$	Chip velocity along the tool-chip interface
$w_i$	Weighting coefficient of response $i$ in the total objective function
$wp$	Workpiece

$\dot{W}_F$	Rate of frictional work per unit contact area
$\dot{W}_P$	Rate of plastic work per unit material volume
$X$	Design matrix
$x - y$	Reference coordinate system
$y$	True response
$\hat{y}$	Approximation of true response
$\hat{y}_i$	Approximate response computed from RSM
$\bar{y}$	Average of true response
$\alpha$	Thermal diffusivity ; Thermal expansion coefficient
$\alpha_0$	Clearance angle
$\beta$	Heat generation partition of workpiece ; Vector of unknown coefficients of quadratic model
$\gamma_0$	Rake angle
$\Delta t$	time step (time increment)
$\Delta t_{m-cr}$	Critical stable time increment for a pure mechanical analysis
$\Delta t_{t-cr}$	Critical stable time increment for a pure thermal analysis
$\varepsilon$	Plastic strain ; error between true response and its approximation
$\dot{\varepsilon}, \dot{\varepsilon}_p$	Effective Plastic strain rate
$\dot{\varepsilon}_0$	Reference plastic strain rate
$\eta_p$	Fraction of plastic work converted to heat
$\eta_F$	Fraction of frictional work converted to heat
$\theta$	Diffraction angle
$\theta_0$	Diffraction angle of stress-free state of material
$\lambda$	Wavelength of X-Ray beams

$\mu$	Coulomb friction coefficient
$\nu$	Poisson's ratio
$\rho$	Density
$\sigma$	Cauchy stress ; Flow stress
$\sigma_n$	Normal compressive stress
$\sigma_{surf}$	Superficial residual stress
$\tau$	Frictional shear stress at the tool-chip contact face
$\tau_y$	Shear flow stress

# **CHAPTER 1    Research Objectives and Thesis Scope**

## **1.1. Motivation**

The economic competition between companies in the aerospace and automotive industries on the one hand and the financial problems in the today's competitive world on the other hand, have forced the manufacturing industries to increase the productivity and reliability while reducing their costs. Mostly, the components in industry are lastly manufactured by machining operations, specifically turning processes. As a result, the performance and durability of these components are aimed to be increased via improving the outputs of the turning process. Currently, the selection of optimum machining parameters is mostly made by trial and error, which would be expensive and time- and energy-consuming.

Many experimental research studies have been conducted on the effects of cutting conditions and tool geometry on the machining characteristics and residual stresses induced by turning process. These studies include statistical or empirical modeling to obtain output response variables such as residual stresses in terms of input design variables including cutting conditions. To reduce the cost of experimental tests, the analytical or numerical models have received much attention in the last decade. These models can be effectively used to study the cutting process and residual stress distribution for a broad range of machining parameters. Although analytical or semi-analytical models can be used to predict the cutting and stress relaxation variables, they cannot provide accurate results due to many simplifying assumptions. Therefore, researchers turned their

attention to finite element models in recent years as these numerical models are capable of providing more accurate results and a better understanding of what occurs in and between the workpiece and tool during the cutting process and in the workpiece during the stress relaxation process. In addition, the FE method is able to predict physical quantities which are not measurable or difficult to measure by experiments such as cutting temperature at the tool-chip interface, distribution of temperature in the workpiece and tool, stress-strain fields in the workpiece, and contact stresses on the tool rake face. Nevertheless, it is necessary to calibrate and validate the predictive finite element tools using a number of experimental tests in order to generate reliable simulation results. The calibrated FE model can then be explicitly utilized for multi-performance optimizations of machining characteristics and residual stresses.

300M steel is a difficult-to-machine material frequently used in the aerospace and automotive industries including in landing gears of aircrafts and drive-shafts of automobiles due to its high strength and resistance to fatigue and corrosion. It is also commonly employed in high strength bolts and frame parts of airplanes and motorsports. Machining 300M steel is accompanied by high cutting temperatures and forces, inducing residual stresses in components. Large temperature causes inaccuracies in component dimensions and phase transformation. High machining forces also raise the power consumption of turning machines and causes breakage of the tool. Moreover, both large cutting temperatures and forces result in high tool wear. Most importantly, tensile residual stresses reduce the resistance to fatigue and corrosion, while high compressive residual stresses increase the fatigue life significantly. The machining process is also required to be efficient by removing material as much as possible. On the other hand, the above-mentioned response variables are highly dependent on machining parameters.

Accordingly, optimization of cutting conditions and tool geometry including cutting speed, feed rate, edge radius, rake angle, and clearance angle to improve machining characteristics and residual stresses are very important to the industry in order to produce high-quality products efficiently. More specifically, when the optimization is performed using an experimentally validated finite element model, by which conducting a large number of costly, time-consuming experiments is avoided, the result will be more desirable and economical to the industry.

## **1.2. Research objectives**

Based on the forgoing discussion, the main objectives of the present PhD research are defined:

- 1- To develop a predictive finite element model using Abaqus software so as to simulate the cutting process to model chip formation and obtain machining forces, and then simulate stress relaxation process in order to extract residual stresses remained in the workpiece.
- 2- To plan a design optimization strategy using a combination of Genetic Algorithm (GA) and Sequential Quadratic Programming (SQP) method to accurately capture global optimal cutting conditions and tool geometry to improve response variables specially the residual stresses induced by orthogonal turning operation.

## **1.3. Thesis outline**

This PhD thesis comprises seven chapters which are briefly described below:

**Chapter 1** provides the motivation for finite element modeling and multi-criteria optimization of machining characteristics and residual stresses in radial orthogonal turning of 300M steel. Accordingly, it explains the research objectives of the present thesis and outlines the thesis scope.

**Chapter 2** is devoted to the fundamentals of orthogonal machining operation. It also summarizes most published research works on finite element prediction of machining and surface integrity characteristics in orthogonal turning process, with a special focus on chip morphology, machining forces, cutting temperature, and residual stresses. Moreover, it briefly explains the optimization studies performed on orthogonal machining of metals available in the literature.

**Chapter 3** presents the underlying methods and concepts in finite element modelling of orthogonal machining operation. The chapter starts with geometrical modelling of workpiece and tool. Then, it explains two interrelated mechanical and thermal analyses and modelling. The chapter continues with two important tasks in FE simulations namely material modelling and frictional modelling. It is then followed by a discussion on thermo-mechanical coupling. Next, the methods for chip separation modelling, which is the most challenging task in FE simulations of machining operations, is described. It goes on with discussions on finite element formulations and Explicit and Implicit solvers commonly used for solving FE problems.

In the second part of this chapter, the developed finite element model of orthogonal turning is described in detail. First, mesh characteristics and boundary conditions of the FE model are explained. Then, numerical integration and time increment utilized for solving thermo-mechanical dynamic problems are discussed. Finally, the chapter ends with a discussion about optimal magnitudes of numerical parameters including size and arrangement of elements, adaptive remeshing, and mass scaling.

**Chapter 4** is dedicated to experimental set-ups and tests conducted in this project. It explains the experimental tests including machining of 300M steel sample using a CNC lathe, machining force measurements using a piezoelectric dynamometer, and surface and subsurface residual stress

measurements in the component using X-Ray Diffraction apparatus with the assistance of Electropolishing and profilometer machines. It also deals with the principles of residual stress measurements using two different XRD machines.

**Chapter 5** describes two main types of Design of Experiment (DoE) and their applications. It then explains Response Surface Method (RSM) and the way it can be applied. The discussion is followed by explaining the optimization methods and strategy utilized in this research to obtain global optimal solutions. At the end of the chapter, the solution procedure to optimize machining parameters including cutting speed, feed rate, edge radius, rake angle, and clearance angle and response variables including cutting temperature, machining forces, and residual stresses is illustrated.

**Chapter 6** is assigned to discussion of the results of the present research dissertation. First, the validation of the FE model using the experimental tests is described. Then, explicit functions of response variables obtained using DoE and RSM are presented. The multi-objective optimization problem formulation based on five quantities including residual stress, cutting temperature, cutting force, thrust force, and material removal rate is presented. Lastly, results of constrained and unconstrained single-objective optimization of residual stresses and multi-objective optimization of residual stresses, cutting temperature, machining forces, and material removal rate are discussed.

**Chapter 7** highlights the main conclusions of the present study and the major contributions to the advancement of knowledge in this field. In addition, it presents the future works of the present PhD dissertation and proposes some possible future works along this area of research. Finally, it briefly explains the outlook for the FE-based multi-performance optimization studies.

## **CHAPTER 2    Research Background**

### **2.1. Introduction**

This chapter briefly defines the basics of orthogonal machining operation. It then explains significant findings of pertinent published research studies on finite element simulation of machining characteristics and residual stresses. Finally, it describes the previous optimization studies conducted on orthogonal turning of metals.

### **2.2. Orthogonal machining**

Turning is one of the most important manufacturing operations to generate a cylindrical shape by removing material from a rotating workpiece using a cutting tool with a single cutting edge. The rotational motion of the workpiece is the primary motion of the cutting process, while the translational motion of the tool is the secondary motion of the cutting process. Orthogonal Machining (OM) is a fundamental material removal process in which the tool nose does not participate in the cutting process, which can be realized when the width of the workpiece is smaller than the cutting edge. In addition, the cutting speed direction is perpendicular to the cutting edge. Also, the undeformed (uncut) chip thickness (feed) should be at least five times smaller than the width of cut to ensure plane-strain condition in the cutting zone.

Finite Element (FE) modeling of machining processes has received growing attention by numerous researchers in the last decades. Orthogonal machining can particularly assist to better understand most machining processes such as nose turning, milling [1-3], and drilling [4-6].

Grinding can also be simulated using orthogonal cutting when each grain of the grinding wheel is considered as a wedge cutting the workpiece [7]. Most specifically, plunge turning, grooving, and parting (cutting off), some of which are displayed in Fig. 2-1, are direct applications of orthogonal turning.

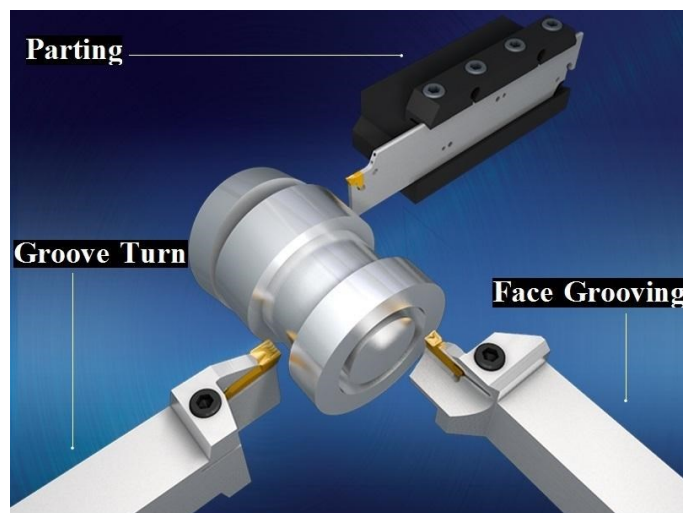
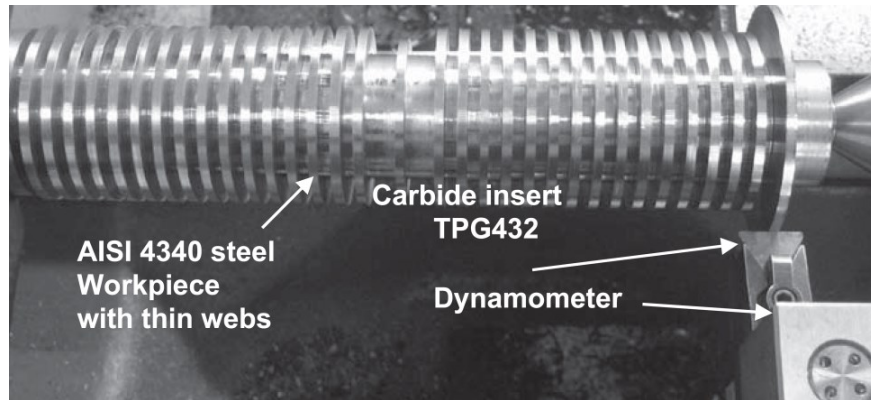


**Fig. 2-1.** Applications of orthogonal turning [8].

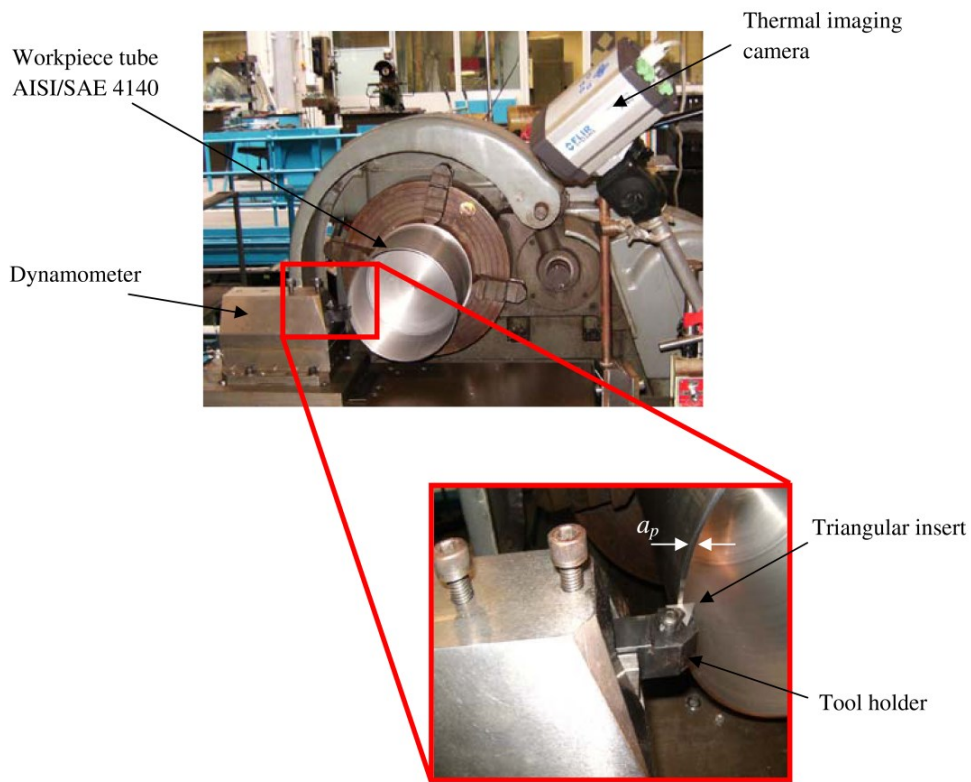
Generally, two types of set-up can be utilized to conduct orthogonal machining. These setups differ based on the workpiece geometry:

- Set-up 1: involves a disc-shaped workpiece [9-22] (Fig. 2-2a)
- Set-up 2: uses a tube-shaped (tube-end or pipe-shaped) workpiece [23-34] (Fig. 2-2b)

Both set-ups were frequently used by researchers for calibration and validation of the finite element model.



(a)



(b)

**Fig. 2-2.** Experimental (a) disc-shaped [16] (b) tube-shaped [33] component set-up configuration of orthogonal turning.

Although there is a large amount of experimental research performed on machining processes, many physical quantities in the cutting zones are still difficult to measure and the main phenomena governing the cutting process still are not fully understood. This makes the role of FE modeling of machining operations more important. The main issues in the FE simulations are:

- To utilize or provide accurate material constitutive and damage models which are valid in a wide range of strain (0.1 to 10), strain rate ( $10^5$ - $10^6$  s<sup>-1</sup>), and temperature (800-900 °C or even higher during machining difficult-to-cut materials) (representing high material nonlinearity)
- To define mechanical and thermal contacts at the tool-chip-workpiece interfaces correctly and accurately
- To overcome the severe element distortion due to chip formation (indicating high geometrical nonlinearity)
- To calculate simultaneously both temperatures and displacements in a highly nonlinear, coupled thermo-mechanical dynamic process (involving a large volume of computations)

## **2.3. Finite element prediction of machining characteristics and residual stresses**

### ***2.3.1. Chip morphology and tool-chip contact length***

Depending on machining conditions and workpiece material, various types of chip can be generated during the machining process. Chips have the potential to be continuous or be segmented (also known as serrated and saw-tooth chips) when ductile metals or hard-to-cut materials such as hardened steels and super-alloys are machined. For specific cutting conditions, elemental chips can also be formed.

The finite element simulation of continuous chips was carried out either with the chip separation criterion [20,28,35-41] such as the Johnson-Cook and Cockraft-Latham damage models or with the adaptive remeshing process based on the pure deformation method [21,34,41-51]. Finite element modeling of saw-tooth chips was mostly done by implementing damage/fracture models [10-12,19,21,27,31,52-59], and by using a sacrificed layer defined ahead of the tool tip to realize chip separation [28,58]. There are also few research works on FE simulation of saw-tooth chips using upgrading/modifying material constitutive models [55,60-64] or combining/coupling two different constitutive models [13], without employing a damage model.

Among the chip morphology parameters, chip thickness is a parameter mostly used for validation of the FE model. Different instruments such as optical microscope [9,10,25,31,65-67], toolmaker's microscope [16,24], Scanning Electron Microscopy (SEM) [29,46,62], digital micrometer [21,68], and a digital caliper [22] were used to measure chip thickness.

Tool-chip contact length is a critical parameter in machining operations because the interfacial friction is produced [69] and the highest temperature often occurs at this contact zone. Various experimental types of equipment including optical microscope [9,25,65-68] and scanning electron microscope [13,33,62] were used for measuring the tool-chip contact length. The worn area left by the chip on the tool rake face, which could be visually detected by an instrument, was mostly used as the main criterion for identifying the tool-chip contact length [62,67,70].

A larger contact length means that a higher driving force is required to form the chip [71,62]. Moreover, a larger contact length means a larger contact area, which leads to more heat generation due to friction at the tool-chip interface, and thus, results in a larger cutting temperature [71]. Despite of these important contributions to the cutting process, the tool-chip contact length was

not frequently used for FE validation purposes as large errors were generally reported between the simulation and experimental results [24,25,65,72]. Some researchers [22] believed that the employed friction model which was not able to capture the sticking-sliding frictional behavior at the tool-chip interface, was the main reason for this discrepancy, while some others [25,62,72] had other views. Haglund et al. [72] stated that this large mismatch might be due to the chip behavior at the earlier stage of the cutting process. During this stage, the tool-chip contact length can be high due to the unstable chip curling, material bonding [72] and/or oxidized layers [72]. It is worth recalling that the chip thickness is often predicted more precisely than the tool-chip contact length [72-74].

### ***2.3.2. Machining forces***

It is well recognized that large cutting forces cause high tool wear, increase the power consumption of turning machines, and result in an excessive deflection and consequently breakage of the tool. In addition, machining forces can produce both compressive and tensile residual stresses [75]. Cutting forces are among the machining data that were mostly used for validation of the finite element simulation of machining processes because they are relatively easy to measure through a simple setup often involving a piezoelectric dynamometer [11-19,21-28,30,31,33,43,47, 54,57,58,65,66,69,76,77].

The influence of cutting parameters on cutting and feed forces was the subject of several numerical studies. In 2004, Yen et al. [78] conducted finite element modeling of orthogonal turning AISI 1020 steel with a tungsten carbide tool using DEFORM software. They found that the cutting and thrust forces rose as the tool edge radius and the tool chamfer width and angle were increased.

Later on, Qian and Hossan [79] carried out the FE simulation of machining four materials namely AISI 52100, AISI H13, AISI D2, and AISI 4340 steels with PCBN (Polycrystalline Cubic Boron Nitride) inserts using AdvantEdge software. The results showed that the cutting and feed forces increased with increasing feed rate, tool's edge radius, and negative rake angle, as shown in Fig. 2-3.

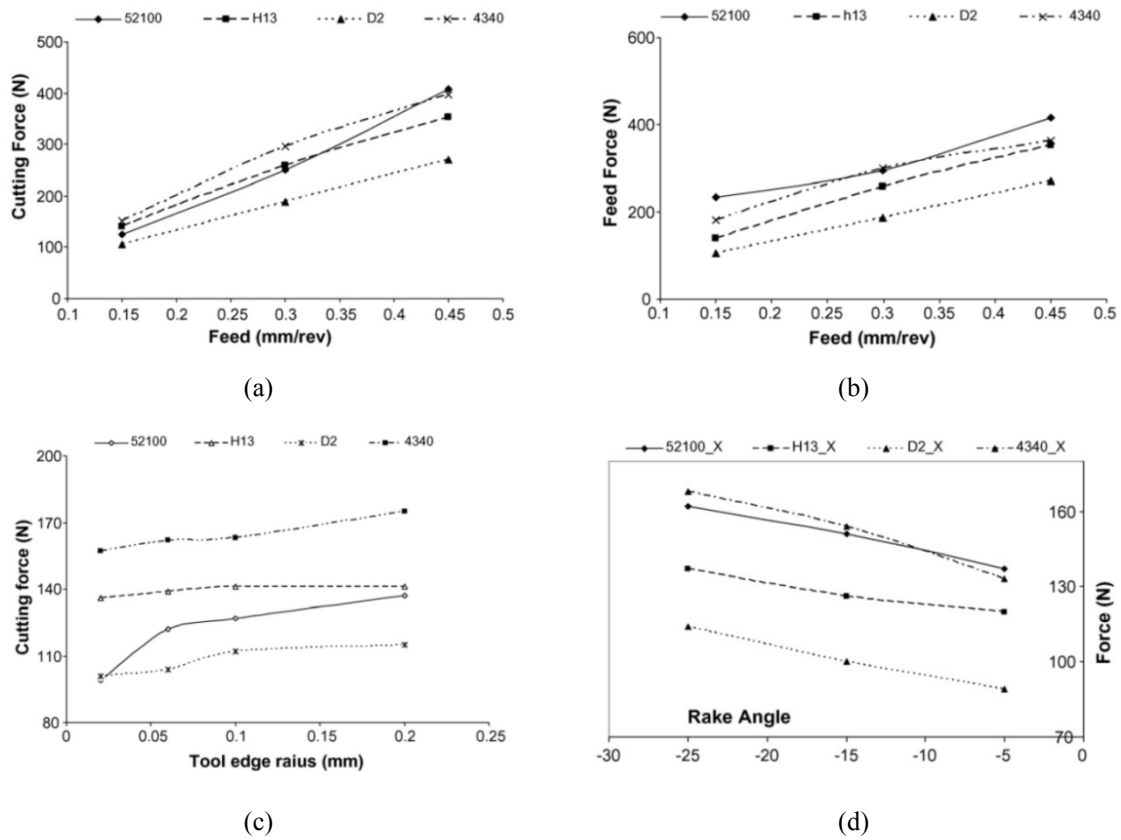


**Fig. 2-3.** Variation of (a,b) the cutting and feed forces with feed, and the cutting force with (c) tool edge radius and (d) rake angle, for materials AISI 52100, AISI H13, AISI D2, and AISI 4340 steels [79].

In 2008, Subbiah and Melkote [28], using FE modelling based on the Abaqus/Explicit program, found that both cutting and thrust forces increased with the uncut chip thickness for different edge radii in micro-cutting of aluminum alloy Al2024-T3 with polycrystalline diamond tool. One year later, Khalili and Safaei [45] utilized DEFORM software to conduct the FE simulation of orthogonal machining of AISI 1045 steel using tungsten carbide insert with various chamfer widths and angles. They found that the thrust force was significantly influenced by the tool edge's chamfer width and angle, while the cutting force was found to be less affected. The results also showed that as the cutting speed increased, the cutting force changed slightly at constant chamfer width and angle. In 2013, Jiang et al. [19] carried out the FE simulation of cutting AISI D2 steel with a TiAlN coated carbide tool using AdvantEdge software. They reported that the cutting forces increased with raising feed. The invers was true for the cutting speed. More recently, Menezes et al. [80] employed LS-DYNA FE code to simulate orthogonal turning of an aluminum workpiece with a high-speed steel tool. The results demonstrated that the cutting force significantly varied with the rake angle and friction coefficient in comparison to the cutting velocity.

In general, the cutting force component is more accurately predicted than the feed (thrust) force component [14,15,20,26,30,33,42,54,61,71,73,76,81,82]. Only a small number of studies reported an acceptable/good accuracy in predicting the feed force component [13,74,82,83]. Haglund et al. [72] found that if the cutting force was in good agreement with the experimental one, then the feed force was underestimated; if the feed force agreed well, then the cutting force was overestimated [72]. Klocke et al. [54] attested that there was a general trend to systematically underestimate the thrust force when using FE modelling and this was true for all the commercial software packages. Recently, Jomaa et al. [84] confirmed this statement. They demonstrated that this phenomenon

was independent of the material constitutive model, showing that the ratios of the predicted thrust force using DEFORM software to the measured one remained roughly constant with three material models including Marusich and Johnson-Cook constitutive equations. Some researchers explained this trend by numerical issues or material anisotropies in the secondary shear zone [54], while some others [85] mentioned the negligence of the flank wear as the reason.

### ***2.3.3. Cutting temperature***

Cutting temperature is one of the most critical quantities in cutting processes as high cutting temperature leads to inaccuracies in component dimensions, phase transformation, and most importantly, creation of tensile residual stresses. Several research works have been carried out to predict the distribution of temperature in the cutting zone by taking advantage of the capability of finite element modeling. Although validation of any FE model using experimental data is a crucial, unavoidable step, only a couple of research studies on FE modeling of machining processes were validated using experimentally measured cutting temperature. This is because it is technically very difficult to measure the cutting temperature during machining. However, there are some research studies which claimed to have measured the temperature at the cutting zone, most of which used infrared thermal imaging camera [33,46,57,69] or a thermocouple embedded in the tool [20,25].

In orthogonal turning, the maximum cutting temperature was found to be at the tool-chip interface [17,26,30,33-37,42,66,83,86,87], around the cutting edge [14,48], or inside the chip [86]. The location at which the maximum temperature occurs depends mostly on the workpiece material's conductivity and cutting conditions. Ozel and Zeren [86] conducted FE modeling of high speed machining of AISI 1045 steel, AISI 4340 steel, and Ti-6Al-4V titanium alloy using

tungsten carbide inserts with round cutting edge. They observed that the maximum temperature occurred inside the chip for the Ti-6Al-4V alloy due to its low thermal conductivity, avoiding the heat to be conducted to the chip boundaries. In contrast, the maximum temperatures took place at the tool-chip interface in machining of AISI 1045 and AISI 4340 steels. Outeiro et al. [11] numerically and experimentally compared temperature distributions during orthogonal turning of AISI 316L steel, as displayed in Fig. 2-4. Obviously, the predicted results with DEFORM software were underestimated by about 200 °C. The authors attributed this discrepancy to the fact that the predicted profile of cutting temperature was obtained after a very short simulation time, which was not sufficient to reach the steady-state condition [11,88].

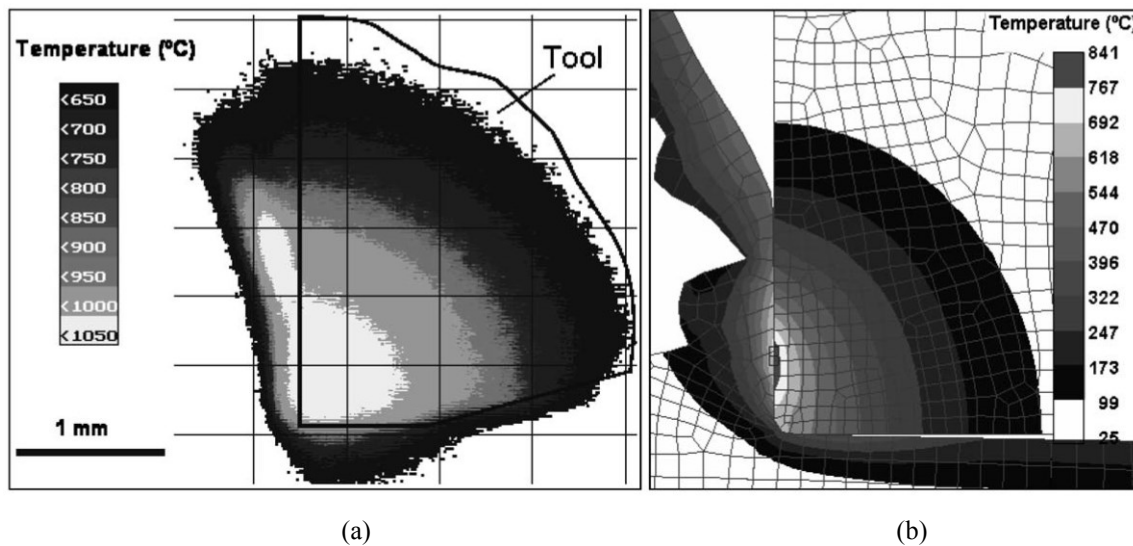


**Fig. 2-4.** A comparison between (a) the measured temperature profile and (b) the predicted one using DEFORM software, during cutting AISI 316L [11].

Arrazola and Ozel [16] obtained the temperature fields in the workpiece and tool during orthogonal turning of AISI 4340 steel with a tungsten carbide tool using Abaqus FE software. On the one hand, when the shear stress at the tool-chip interface was unlimited, 500, or 700 MPa, a second hot spot appeared at the bottom part of the tool next to the cutting edge and a maximum temperature of about 1544 K was seen for all the three cases (Fig. 2-5a,c,d). On the other hand, when a shear limit of 200MPa was applied, the maximum temperature decreased to 1222K and the second hot spot vanished (Fig. 2-5b). It was thus concluded that the shear stress limit in the Zorev model should be employed with care to obtain an accurate machining temperature.

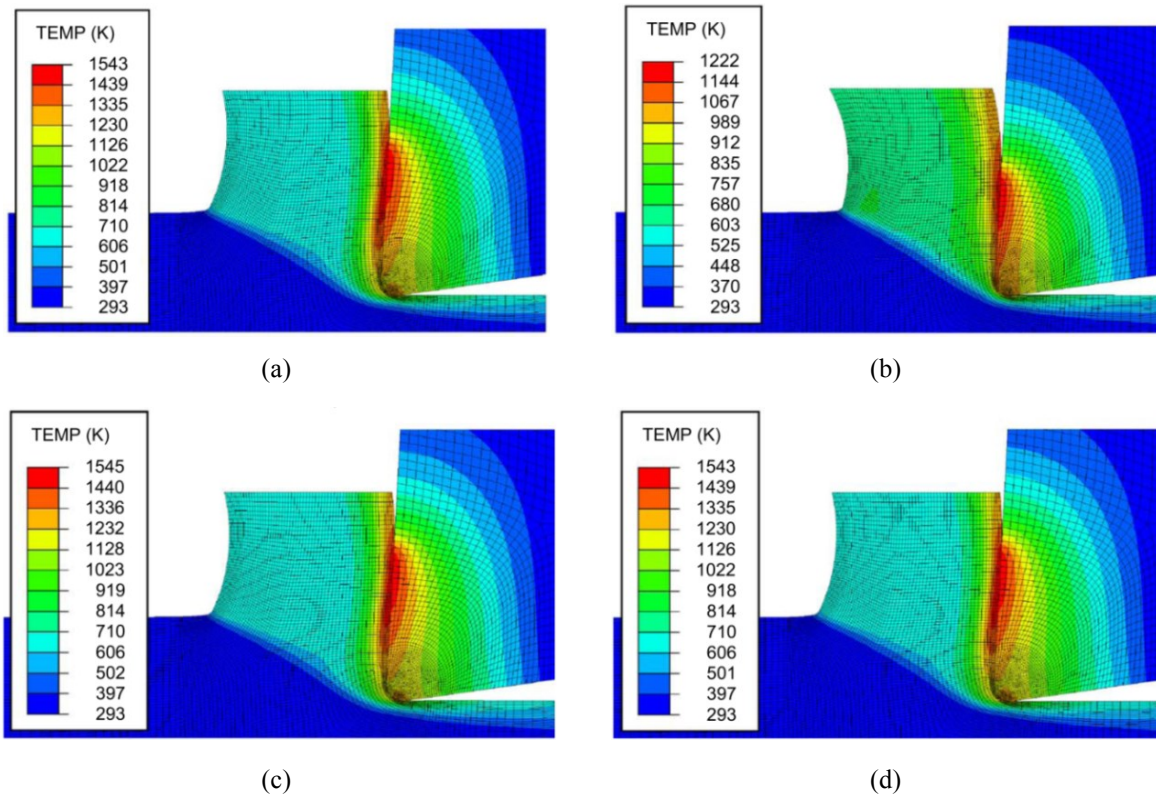


**Fig. 2-5.** Predicted temperature fields using Abaqus/Explicit for different shear stress limits: (a) unlimited, (b) 200 MPa, (c) 500 MPa, and (d) 700 MPa [16].

The influence of machining parameters including cutting speed, feed or depth of cut (uncut chip thickness), edge radius, and rake angle on the cutting temperature was examined in several finite element studies. Majumdar et al. [87] observed that the predicted cutting temperature using ANSYS software increased with increasing cutting speed during cutting free-machining steel with a carbide insert. Ozel and Zeren [89] reported that larger depth of cut and edge radius led to higher machining temperature in cutting of AISI 4340 steel with a carbide tool. Al-Zkeri et al. [30] modeled orthogonal turning AISI 4142H steel with TiAlN coated tools using DEFORM software. They found that the predicted maximum tool temperatures on the rake face were similar for all the edge radii considered, while the temperature at the tool tip rose with increasing the tool edge radius. Tang et al. [90] employed Abaqus/Explicit FE code to simulate orthogonal cutting of AISI D2 steel with CBN inserts. They observed that the maximum temperature on the machined surface firstly declined and then rose with the depth of cut. They also found that the effect of the depth of cut on the temperature profile was much less than that of the cutting speed.

#### ***2.3.4. Residual stresses***

The machinability aspects have been investigated with different finite element tools and numerical methods. The interest in machinability aspects is governed by the concern to improve the productivity of the machining processes. While efforts on predicting cutting variables still continue and understanding the interactions among these variables and input parameters is an active research area, the residual stresses are the end goal [91] as they highly affect the fatigue life of machined components. Residual stresses remain when the original causes of the stresses such

as external forces and heat gradient in a manufacturing process have been removed. Residual stresses are formed through three mechanisms as follows [92,93]:

i. A volume change due to phase transformation:

If the phase change reduces the material volume, the surface layer is under tension and a tensile residual stress is formed. In contrast, an increase in volume leads to compressive residual stresses (Fig. 2-6a).

ii. Plastic deformation due to thermal loads:

Heat due to thermal load causes the surface layer to expand more than the bulk material, which leads to plastic (permanent) deformation in the near-surface material. After cooling, the expanded part contracts and tends to return to the original position due to the elastic recovery. At the same time, the layer contraction is partially prevented by the adjacent material (bulk material) which already underwent plastic deformation. This results in creation of tensile residual stress (Fig. 2-6b).

iii. Plastic deformation due to mechanical loads:

Machining forces compact the surface layer, which yields plastic deformation in the region. After machining and removing the forces, the contracted surface layer expands and tends to come back to the initial location owing to the elastic recovery. However, the layer's material expansion is prevented by the neighboring material which experienced permanent deformation. The resulting effect is formation of compressive residual stress (Fig. 2-6c).

Mechanisms (ii) and (iii) simultaneously occur in most machining operations, whereas Mechanism (i) exists depending on the generated heat during cutting and the evacuated heat from

the cutting zone. It needs mentioning that according to Ref. [75], the mechanical load may produce tensile residual stresses as well as compressive ones.

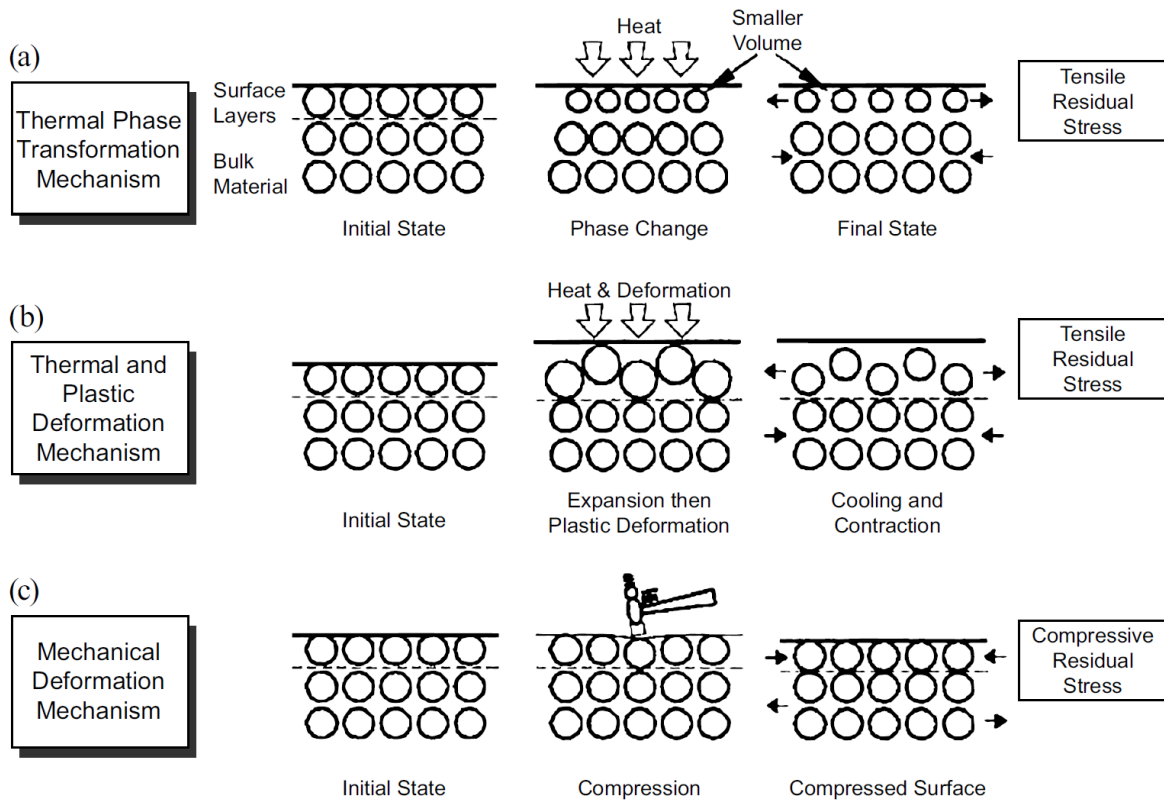


**Fig. 2-6.** The mechanisms of creation of residual stresses [92,93].

In recent years, a growing attention has been paid to the prediction of residual stresses using numerical tools calibrated using experimental tests. It needs mentioning that the residual stresses are difficult to measure and model [94]. No standard procedure in calculating and extracting the residual stresses from the FE model was described by most of the previous research works [95]. In this section, an insight into how to obtain residual stresses from the FE model and the latest studies and results on finite element modeling of residual stresses are provided.

The finite element prediction of residual stresses is a critical, important task because the magnitudes of the predicted residual stresses are highly sensitive to and dependent on the applied boundary conditions and loads. However, only a couple of published papers provided some insight about the tool-workpiece interactions, the thermal and mechanical boundary conditions and loads, the cooling procedure, and the way of extracting stresses in modeling the residual stress step. A number of research studies [11,26,57,66,89,96] reported that the residual stresses were extracted from the FE model after the tool was retracted/released from the workpiece. This ensures that no surfaces of the tool are in contact with the workpiece (known as tool unloading or eliminating cutting forces) in the residual stress step. In a few FE analyses, it was mentioned that the tool was brought to a complete stop after being retracted [26] and the loads applied to the boundaries of the workpiece in the cutting step were removed (known as releasing boundary constraints or unloading clamping force) [22,26,34,36,40,66]. The lower edge of the workpiece was fixed in the vertical direction, and only one node on this edge was fixed in both directions [18] to avoid rigid body motion [97]. Lastly, the workpiece was allowed to cool down to room temperature for strain and stress relaxation (also called thermal unloading) [26,36,49,50,57,66,96,98].

Likewise, only a couple of FE research studies presented procedures for extracting residual stresses from the nodes or elements of the cut workpiece. Ee et al. [99] extracted residual stresses from a region far enough away from the chip root to exclude the localized stress field created by the tool tip at the chip root (Fig. 2-7a). Nasr et al. [49,50] computed the residual stresses by taking the average of ten elements at each depth in the mid-length of the workpiece. They claimed that this procedure avoided misleading results which might be caused due to the transient effects in the beginning and end of the cutting process. Schulze et al. [100] also chose a similar part of the

workpiece to that of Nasr et al. [50] for extracting the residual stresses (Fig. 2-7b). Muñoz-Sanchez et al. [34] averaged the residual stresses distribution over a small zone of the workpiece being in the region with the stationary (steady state) conditions and far away from the chip root. Similarly, Outeiro et al. [95,101] presented a procedure by which the predicted residual stresses were extracted and averaged in a region (Region III in Fig. 2-7c) far enough from the chip root. Pu et al. [102] employed a similar way to Outeiro and his co-workers [101] for residual stress predictions. On the other hand, Tang et al. [90] extracted the residual stresses from the nodes which were situated in a 0.85-mm length of cut (Fig. 2-7d). Stenberg and Proudian [96] obtained the residual stresses from 10 equally spaced nodes distributed throughout the newly formed surface and subsurface of the workpiece (Fig. 2-7e).

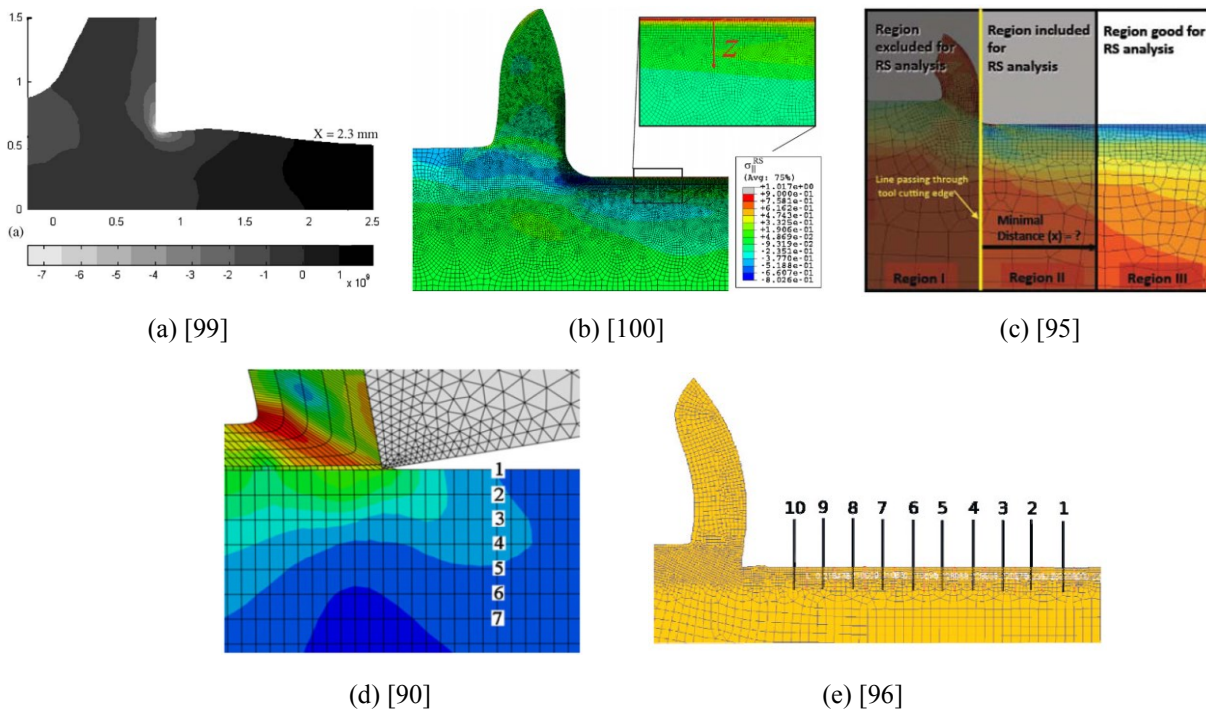


**Fig. 2-7.** The ways of residual stress extraction from a FE model.

Residual stresses are of great importance and the main objective is to reduce the detrimental tensile residual stresses or generate/increase beneficial compressive residual stresses in the machined components. The residual stresses are strongly influenced by cutting conditions, tool geometry, and workpiece and tool materials. Residual stresses were mostly reported to have been tensile on the machined surface [11,18,22,26,34,49,50,76,86]. However, there is a small number of research studies reporting the occurrence of compressive residual stresses on the surface for specific conditions [26,50,90]. It was also frequently observed that the peak tensile stress occurred on the surface, while the peak compressive stress happened below the surface [26,34,49,50,66,76,90].

The impacts of machining parameters on residual stresses were assessed by a number of research works. Due to the great importance of residual stresses, these impacts will be discussed here in detail. In 2006, Outeiro et al. [11] studied the variation of residual stresses with respect to cutting parameters in orthogonal turning of AISI 316L steel with uncoated and TiC/Al<sub>2</sub>O<sub>3</sub>/TiN coated tungsten carbide tools. With increasing the cutting speed, the superficial circumferential residual stresses did not change and increased (Fig. 2-8a) when uncoated and coated tools were used, respectively. Also, the circumferential residual stress at the surface (Fig. 2-8b) and the thickness of the tensile layer increased when the uncut chip thickness was raised. For uncoated tools, both superficial circumferential residual stresses (Fig. 2-8c) and thickness of the tensile layer declined with increasing the rake angle. Moreover, the superficial circumferential residual stresses rose (Fig. 2-8d) and the thickness of the tensile layer decreased with increasing the cutting edge radius.

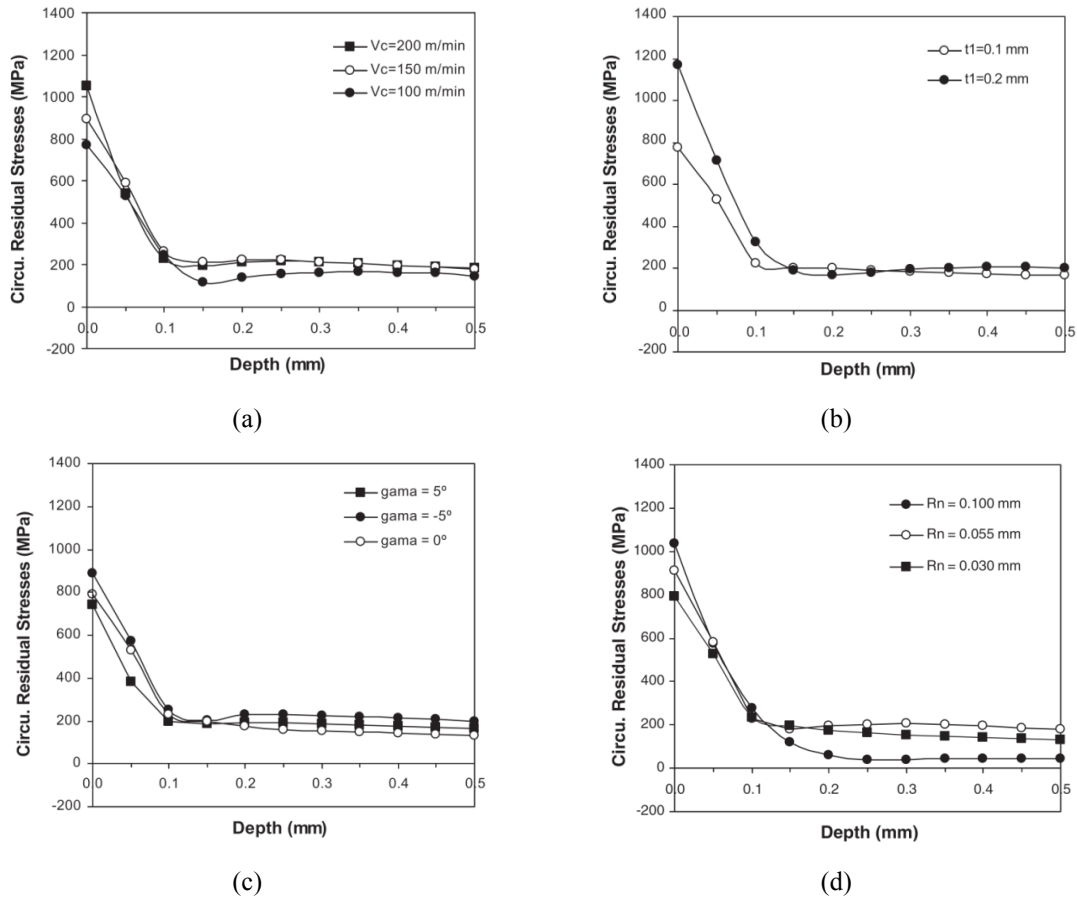


**Fig. 2-8.** The influence of (a) cutting speed (using the TiC/Al<sub>2</sub>O<sub>3</sub>/TiN coated carbide tool), (b) uncut chip thickness (feed), (c) rake angle and (d) edge radius on circumferential residual stresses [11].

One year later, Nasr et al. [49] investigated the impact of a cutting edge radius on the residual stresses induced by orthogonal dry cutting of austenitic stainless AISI 316L steel using Abaqus software and an Arbitrary Lagrangian Eulerian (ALE) formulation. It was found that higher tensile residual stresses were created in the near-surface layer with increasing the edge radius (Fig. 2-9a), which was attributed to increasing the workpiece temperature. The results also demonstrated that the low thermal conductivity of stainless AISI 316L steel, compared to carbon or alloy steels, confined the heat flow generated by the friction at the tool-workpiece interface into the near-

surface layer, yielding that the thickness of the tensile layer was not affected by changing the edge radius (Fig. 2-9b).

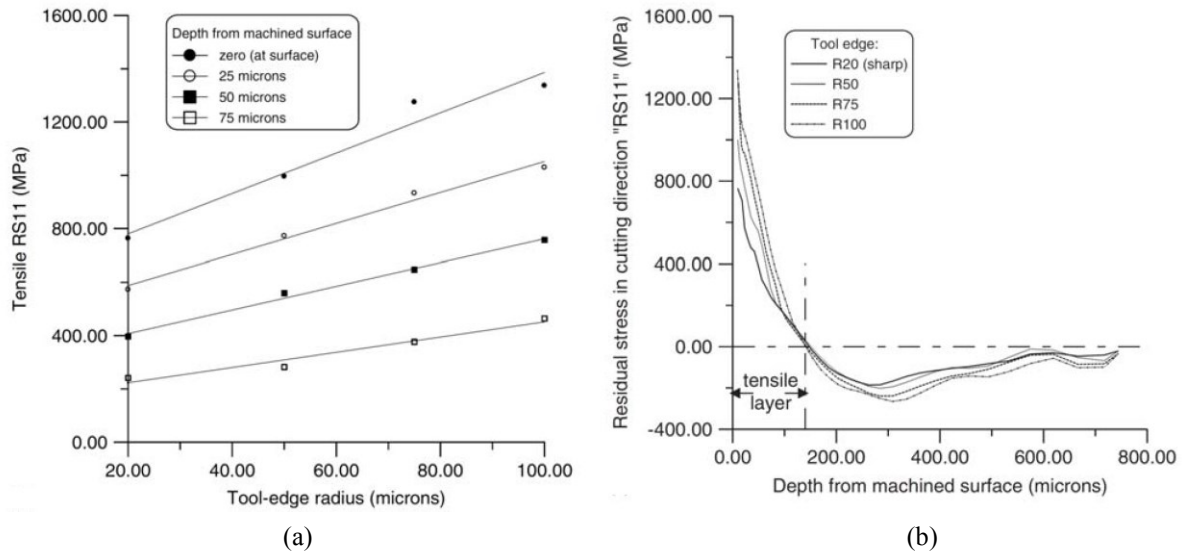


**Fig. 2-9.** Effect of tool edge radius (a) on the tensile residual stress in the cutting direction (RS11) at different depths, (b) on in-depth residual stress RS11 [49].

Next, Maranhao and Davim [76] found by conducting the FE simulation of orthogonal cutting of AISI 316 steel using AdvantEdge software that the lower the feed rate was, the smaller the residual stresses were. These researchers also observed that the cutting edge radius did not affect the circumferential residual stresses. Mohammadpour et al. [32] analyzed the impact of cutting speed and feed on the distribution of residual stresses induced by orthogonal turning of AISI 1045 steel with a tungsten carbide tool using SuperForm software. They found that the maximum value of tensile residual stresses generally increased with raising cutting speed and feed rate as shown in Fig. 2-10.

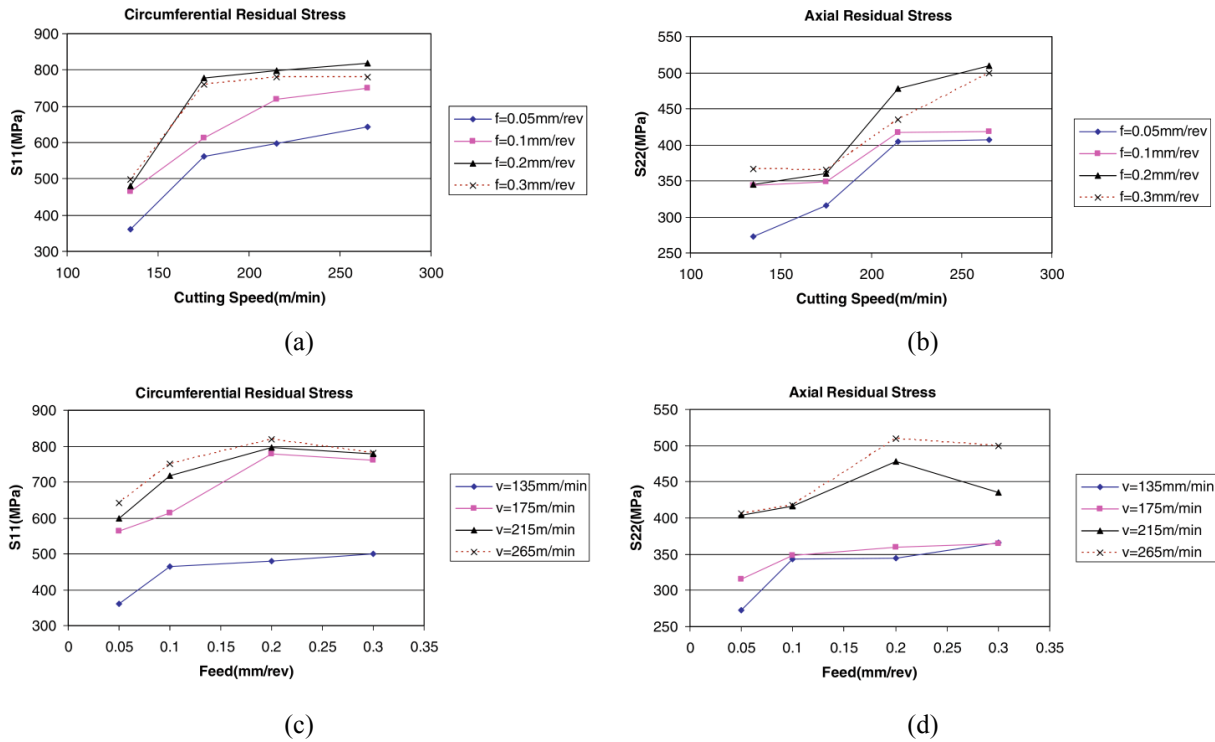


**Fig. 2-10.** The variation of the maximum value of residual stresses in the cutting (circumferential) S11 and feed (axial) S22 directions with (a,b) cutting speed and (c,d) feed [32].

It was also reported in the literature that a higher cutting edge radius led to a deeper penetration of tensile residual stresses induced by orthogonal cutting of AISI 1045 steel with a tungsten carbide tool [100]. Muñoz-Sanchez et al. [34] investigated the effect of tool wear on residual stresses in machining AISI 316L steel. The results demonstrated that the residual stress increased when worn tools were employed compared to the fresh ones. For the same material, another study by Moussa et al. [18] showed that the magnitude of the tensile residual stress in the machined subsurface declined when the cutting speed increased and depth of cut decreased. Also, the machining affected layer thickness decreased gradually with increasing the cutting speed.

## 2.4. Optimization studies

Many of the past machining and surface integrity studies have focused on the experimental analysis and optimization of machining parameters including cutting conditions and tool geometry. Among these optimization studies, the objective function was often based on surface roughness, material removal rate, and production cost/time/rate, as mentioned in Ref. [103]. In recent years, there have been some attempts to develop predictive models for machining and surface integrity characteristics using finite element simulations and perform optimization studies on these models to avoid conducting a large number of expensive, time-consuming experimental tests. However, a few studies dealt with the improvement of residual stresses.

In 2009, Al-Zkeri et al. [30] examined the influence of edge radius of a honed TiAlN coated carbide tool on cutting forces and tool temperature and stresses generated during orthogonal turning of AISI 4142H steel. The cutting forces and chip thickness were measured experimentally and were then utilized for calibration of the FE model created with DEFORM software. The results demonstrated that finite element analysis could be utilized to optimize the edge geometry of coated tools through the prediction of tool temperatures and stresses, which are hard to measure experimentally. More recently, in 2013, Prete et al. [104] presented an optimization procedure in iSight environment interfaced with AdvantEdge software for orthogonal turning process of Waspaloy. They sought the optimal machining parameters including feed rate, cutting speed and rake angle using Genetic Algorithm (GA) and Simulated Annealing (SA) algorithm to maximize the material removal rate as the objective function subjected to the constraints of cutting temperature and forces. In the optimization process, the feed rate and cutting speed were confined to upper and lower bounds, while only three values of  $-10^\circ$ ,  $0^\circ$ , and  $15^\circ$  were considered for the

variation of the rake angle. Finally, the authors recommended that the residual stress optimization should be done for future works along this field. The optimization of residual stresses was also suggested in a research work by Stenberg and Proudian [96]. In 2016, Sadeghifar et al. [51] conducted the optimization of machining parameters including cutting speed, feed rate, edge radius, and rake angle based on the finite element analysis. They captured the global minimum value of cutting temperature against the resultant cutting force constraint in orthogonal turning of AISI 4340 steel. The results demonstrated that low feed and edge radius along with a roughly small magnitude of cutting speed and an intermediate value of rake angle in the given bounds yielded the smallest cutting temperature in the presence of a confined resultant cutting force.

## **CHAPTER 3    Finite Element Modelling**

### **3.1. Introduction**

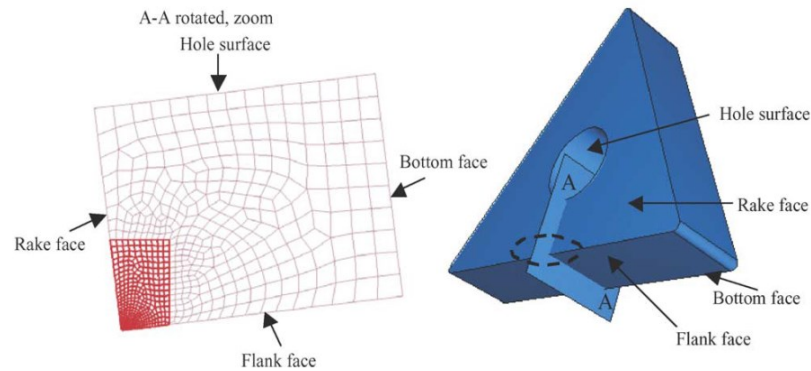
Metal cutting is a highly nonlinear, coupled thermo-mechanical dynamic process. Due to its inherent complexity, a successful finite element simulation of cutting processes depends highly on the selection and creation of appropriate and reliable geometrical, mechanical, thermal, material (flow stress), frictional, and chip formation models and parameters.

In this chapter, the fundamental methods and concepts related to the above-mentioned models and parameters in the finite element simulation of machining operations particularly orthogonal turning are presented. Then, the theory and techniques in the finite element modelling of orthogonal turning utilized in the present study are described.

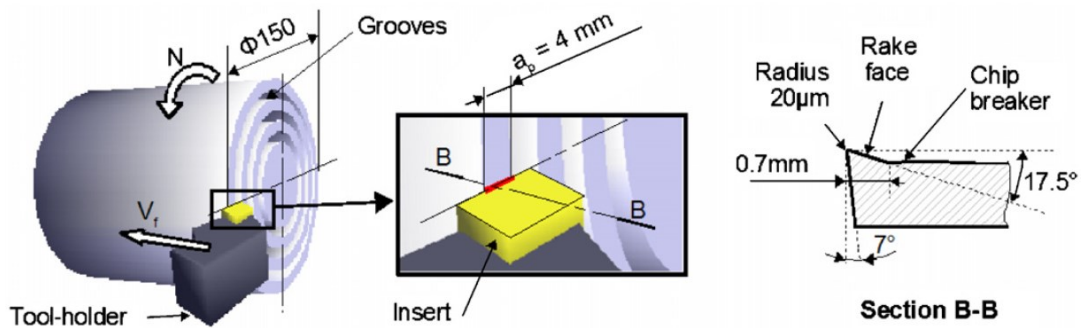
### **3.2. Underlying concepts and methods in finite element modeling of orthogonal machining**

#### ***3.2.1. Geometrical modelling***

From a geometrical viewpoint, for simplicity, only a portion of the workpiece is modeled as a planar rectangle (for 2D problems) with a relatively short length. The length of the workpiece should be large enough to reach the steady-state conditions during the cutting process. As mentioned earlier, the plane strain condition was usually assumed in orthogonal turning tests when the undeformed/uncut chip thickness (feed) was much smaller [27,33,35] (at least five times [36,39,105] or ten times [23,44,106]) than the width of cut. Similar to the workpiece, a part of the cutting tool is often modeled as shown in Fig. 3-1a [42] and 3-1b [27].



(a) [42]



(b) [27]

**Fig. 3-1.** Identification of tool geometry for FE modeling.

The tool is mostly considered as a rigid body [11,12,17,23-25,32,33,35-39,42-46,52-54,60-63, 65,71,73,78,80,81,98,105-111] due to its high stiffness compared with the workpiece [33,37]. This can significantly reduce the computational time of the FE model by avoiding the calculation of the displacements in the tool nodes [63]. However, there are some research works [28,42,43,47,55,56,70,71,74,83,97] in which the tool was modeled as an elastic, deformable body, allowing to obtain stresses, strains and wear in the tool. Al-Zkeri et al. [30] compared the results obtained using rigid and elastic tools. The simulation was launched with a rigid tool to minimize the simulation time, and after reaching steady-state cutting temperature and forces, the tool was

switched to an elastic body and the elastic tool stresses were computed. The results showed slight changes being less than 2% in the workpiece's stresses and the tool's cutting forces, attesting the validity of the FE modeling with the assumption of considering the tool as a rigid part.

### 3.2.2. Mechanical modelling and analysis

The equations of motion for 2D cutting problems can be written as [112,113]:

$$\begin{aligned} \frac{\partial \sigma_{xx}}{\partial x} + \frac{\partial \sigma_{xy}}{\partial y} + \rho b_x &= \rho \frac{\partial^2 U_x}{\partial t^2} \\ \frac{\partial \sigma_{yx}}{\partial x} + \frac{\partial \sigma_{yy}}{\partial y} + \rho b_y &= \rho \frac{\partial^2 U_y}{\partial t^2} \end{aligned} \quad (3-1)$$

where  $\sigma$  is the Cauchy stress,  $\rho$  density,  $b$  body force,  $t$  time,  $U$  is the material displacement, and  $x - y$  is the reference coordinate system. By applying weak formulation and finite element discretization [112], Eq. (3-1) may be written in matrix form as follows:

$$[M] \{\ddot{U}\} + \{R_{int}\} = \{R_{ext}\} \quad (3-2)$$

in which  $[M]$  is the mass matrix,  $\{\ddot{U}\}$  is the acceleration vector, and  $\{R_{int}\}$  and  $\{R_{ext}\}$  are the vectors of internal and external forces, respectively. Here, the effect of damping is ignored [114], and as a result,  $\{R_{int}\}$  is equal to

$$\{R_{int}\} = [C_d] \{\dot{U}\} + [K_s] \{U\} \cong [K_s] \{U\} \text{ where } [C_d] \cong 0 \quad (3-3)$$

where  $[C_d]$  and  $[K_s]$  are the damping and stiffness matrices, respectively. Also,  $\{R_{ext}\}$  involves the external forces applied during cutting including the reaction forces at the supports.

### 3.2.3. Thermal modelling and analysis

Heat transfer during machining process is governed by the energy equation as [113,115]:

$$\rho c \left( \frac{\partial T}{\partial t} + V_x \frac{\partial T}{\partial x} + V_y \frac{\partial T}{\partial y} \right) = k \left( \frac{\partial^2 T}{\partial x^2} + \frac{\partial^2 T}{\partial y^2} \right) + \dot{Q}_g \quad (3-4)$$

where  $c$  and  $k$  are the specific heat capacity and thermal conductivity, respectively, and  $V$  ( $\dot{U}$ ) is the material velocity. Also,  $\dot{Q}_g$  is the sum of two sources of heat generation in machining process, i.e. plastic work in the primary and secondary deformations zones and frictional work between the tool-workpiece and tool-chip interfaces. Therefore, the heat generation is calculated as [47,113,115,116]:

$$\dot{Q}_g = \eta_P \dot{W}_P + \eta_F \dot{W}_F = \eta_P (\sigma \dot{\epsilon}_p) + \eta_F (\tau V_{Ch}) \quad (3-5)$$

in which  $\eta_P$  and  $\eta_F$  are the fraction of plastic work converted to heat (known as Taylor-Quinney coefficient or inelastic heat fraction) and the fraction of frictional work converted to heat, respectively, and  $\dot{W}_P$  and  $\dot{W}_F$  are in turn the rate of plastic work per unit material volume and the rate of frictional work per unit contact area. In addition,  $\sigma$ ,  $\dot{\epsilon}_p$ ,  $\tau$ , and  $V_{Ch}$  are flow stress, effective plastic strain rate, frictional shear stress at the tool-chip contact face, and chip velocity along the tool-chip interface, respectively.

A discretized weak form of Eq. (3-4) is given as [112]:

$$[C_T] \{\dot{T}\} + [K_T] \{T\} = \{\dot{Q}_g\} \quad (3-6)$$

where  $[C_T]$  and  $[K_T]$  are the volumetric heat capacitance and thermal conduction matrices, respectively, and  $\{T\}$  is the vector of nodal temperatures, and  $\{\dot{T}\}$  is the vector of nodal temperature rates.

Thermal Effusivity is a measure of the ability of the material to exchange thermal energy with its surroundings, which is utilized to calculate the portion of the frictional heat distributing to the workpiece (heat generation partition of the workpiece  $\beta$ ) as follows [18,47]:

$$\beta = \frac{Ef_{wp}}{Ef_{wp} + Ef_t} \quad (3-7)$$

where  $Ef = \sqrt{\rho kc}$  is the thermal effusivity. Also, the subscripts  $wp$  and  $t$  refer to the workpiece and tool, respectively. Obviously,  $1 - \beta$  is the portion of the frictional heat distributing to the tool.

A study was carried out by Akbar et al. [33] to investigate the effect of heat generation partition on some cutting variables during machining AISI 4140 steel. It was observed that decreasing the value of the heat partition into the cutting tool ( $R_T$ ) reduced the temperature in the cutting part of the tool (Fig. 3-2A), whereas it did not considerably influence the von Mises stress in the primary and secondary deformation zones (Fig. 3-2B). It was also found that both tool-chip contact length and average temperature along this length rose when  $R_T$  increased. This study showed the importance of accurately determining the value of the heat partition coefficient in a FE model.

Thermal conductance between the tool and workpiece is the heat conduction through the tool-chip contact face from the chip with higher temperature to the tool with lower temperature during the cutting process. This conducted heat is calculated as [47]:

$$Q = h_{int} (T_{wp} - T_t) \quad (3-8)$$

in which  $h_{int}$  is thermal conductance coefficient (known with various names in the literature such as ‘heat/thermal’ ‘transfer/conductance’ ‘partition/coefficient’),  $T_{wp}$  and  $T_t$  are the workpiece and

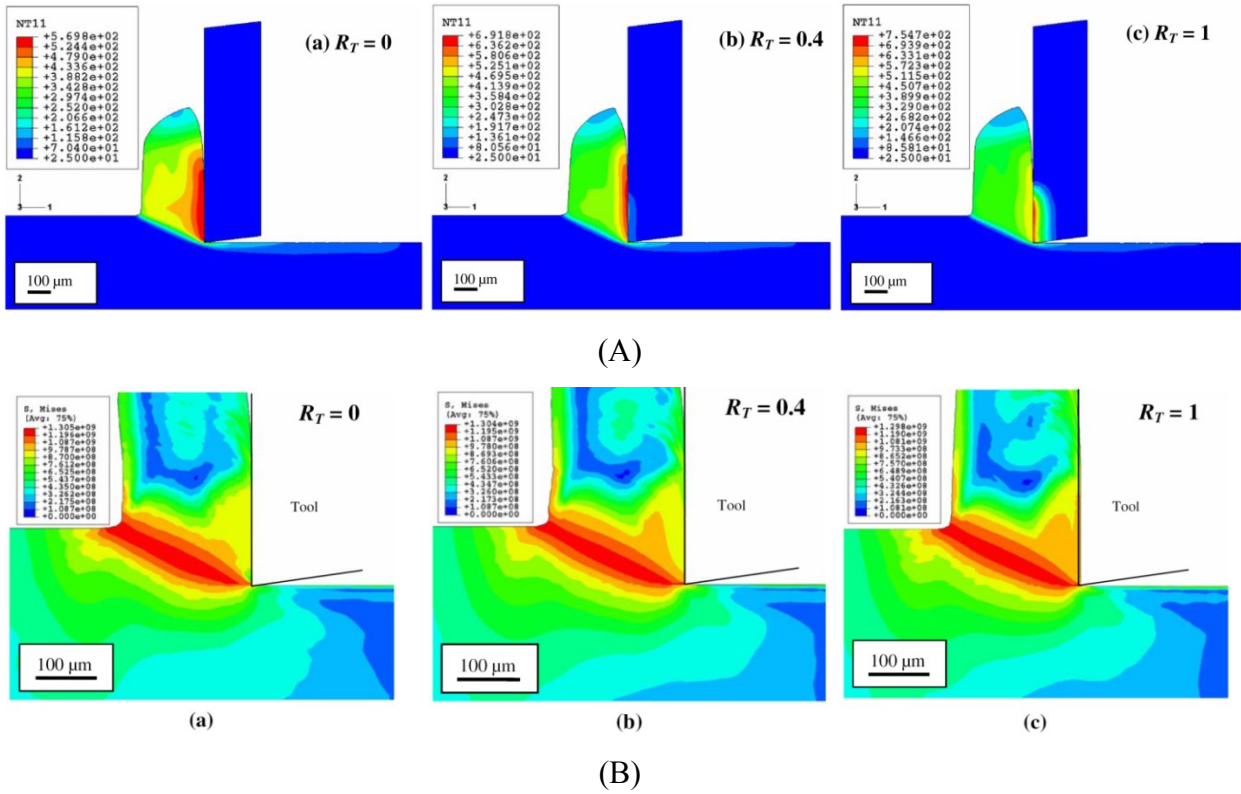


**Fig. 3-2.** Influence of heat fraction  $R_T$  on (A) temperature ( $^{\circ}\text{C}$ ) and (B) von Mises stress (Pa) distributions: (a)  $R_T = 0$ , (b)  $R_T = 0.4$ , and (c)  $R_T = 1$  [33].

tool's temperature at the tool-chip interface, respectively.

Thermal conductance is applied to reach a thermal balance between the tool and workpiece during cutting. In practice, thermal conductance is a function of the gap, contact temperature and contact pressure between the tool and chip [47]. In metal cutting, the gap is often considered to be near zero and the values of pressure and temperature are very high. However, thermal conductance is applied as a constant value in metal cutting simulations for simplicity or lack of having experimental information. High magnitudes of thermal conductance including 500 [47], 1000 [11,18,25,31,45,50,57,61,97],  $10^4$  [21], and  $10^5$  ( $\text{kW} \text{)/(m}^2\text{C}$ ) [16] were reported to have been utilized for calibration of the FE model for different combinations of tool and workpiece's

materials. This parameter was chosen as a very high value because the high pressure of the chip on the tool rake face makes a perfect (thermal) contact between the tool and chip [11,57,64,78,82,111]. Another reason for assigning a large value to thermal conductance was to reach a steady-state condition quickly [18,21,25,45,113,117] so as to shorten the cutting time to avoid encountering an excessive distortion of elements. Besides, the numerical results obtained were in good agreement with the experimental results [25,31,57].

For the residual stress step, convection heat transfer occurs between the workpiece surface and the ambient as:

$$Q = h (T_{wp} - T_a) \quad (3-9)$$

in which  $h$  is convection heat transfer coefficient, and  $T_{wp}$  and  $T_a$  are the workpiece and ambient (room) temperature. This heat evacuation allows the workpiece to cool down to room temperature and relax the stresses.

#### **3.2.4. Material modelling**

It is well recognized that the material models used in finite element modeling of machining processes cannot be identified using quasi-static tests. This is due to the fact that the workpiece material undergoes high strain, strain rate, and temperature during machining. Hence, alternative techniques such as high speed compression tests, impact tests, and Split Hopkinson Pressure Bar (SHPB) tests were extensively used in the identification of material constitutive/damage equations dedicated to FE modeling of machining processes. Several material constitutive equations were commonly used in FE simulation of machining. These models are summarized in Table 3-1.

**Table 3-1**

Material constitutive models for FE modeling of machining operations ( $\varepsilon$  : strain,  $\dot{\varepsilon}$  : strain rate,  $T$  :temperature)

Model	Constitutive equation	Constants
Johnson-Cook	$\sigma = (A + B \varepsilon^n) \left( 1 + C \ln \left( \frac{\dot{\varepsilon}}{\dot{\varepsilon}_0} \right) \right) \left[ 1 - \left( \frac{T - T_0}{T_{melting} - T_0} \right)^m \right]$	$A, B, n, C, m$
Power law	$\sigma = \sigma_0 \left( \frac{\varepsilon}{\varepsilon_0} \right)^n \left( \frac{\dot{\varepsilon}}{\dot{\varepsilon}_0} \right)^m \left( \frac{T}{T_0} \right)^p$	$\sigma_0, n, m, p$
Zerilli-Armstrong	$\sigma = C_0 + C_1 \exp \left[ -C_3 T + C_4 T \ln \left( \frac{\dot{\varepsilon}}{\dot{\varepsilon}_0} \right) \right] + C_5 \varepsilon^n \quad \text{for bcc crystal structures}$ $\sigma = C_0 + C_2 \varepsilon^n \exp \left[ -C_3 T + C_4 T \ln \left( \frac{\dot{\varepsilon}}{\dot{\varepsilon}_0} \right) \right] \quad \text{for fcc crystal structures}$	$C_0, C_1, C_3, C_4, C_5$
Usei-Maekawa-Shirakashi	$\sigma = \sigma_0(T, \dot{\varepsilon}) \left( \int_{path} e^{n \frac{K}{T} \frac{1}{\dot{\varepsilon}} - \frac{m}{n}} d\varepsilon \right)^n$	$K, n, m$
Oxley	$\sigma = \sigma_0(T, \dot{\varepsilon}) \varepsilon^{n(T, \dot{\varepsilon})}$	-
Marusich	$\left( 1 + \frac{\dot{\varepsilon}_p}{\dot{\varepsilon}_0} \right) = \left( \frac{\sigma}{g(\varepsilon_p)} \right)^{m_1} \quad \text{if } \dot{\varepsilon}_p < \dot{\varepsilon}_t$ $\left( 1 + \frac{\dot{\varepsilon}_p}{\dot{\varepsilon}_0} \right) \left( 1 + \frac{\dot{\varepsilon}_t}{\dot{\varepsilon}_0} \right)^{\frac{m_2}{m_1} - 1} = \left( \frac{\sigma}{g(\varepsilon_p)} \right)^{m_2} \quad \text{if } \dot{\varepsilon}_p > \dot{\varepsilon}_t$ $g(\varepsilon_p) = [1 - \alpha(T - T_0)] \sigma_0 \left( 1 + \frac{\varepsilon_p}{\varepsilon_0} \right)^{\frac{1}{n}}$	$m_1, m_2, \alpha, \sigma_0, n$

The influence of material constitutive models on cutting process variables was examined by a small number of researchers. In 2004, Raczky et al. [23] utilized the Eulerian FE approach to simulate orthogonal cutting of commercial purity ETP copper (C11000) based on hydrodynamic

(Material Type 10 within LS-DYNA software) and Johnson-Cook material models. The results showed that the maximum equivalent strain, size of secondary deformation zone, and stresses in the primary deformation zone predicted by the J-C model were higher than those obtained with the hydrodynamic model. Recently, Paturi et al. [46] formulated two constitutive models namely modified Johnson-Cook (mJ-C) and modified Zerilli-Armstrong (mZ-A) material models for AA7075-T6 aluminum alloy by conducting isothermal uniaxial tensile tests. The predicted chip thickness, shear plane angle, and tool-chip contact temperature using mZ-A model were slightly more accurate than those obtained by using mJ-C model.

The Johnson-Cook material model was extensively utilized in finite element modeling of machining operations. The effect of J-C model's constants on FE results was studied by [12,57]. In 2007, Umbrello et al. [57] experimentally and numerically examined the impacts of five different sets of J-C material constants on the cutting variables and residual stresses for orthogonal turning of AISI 316L steel. The residual stress distributions predicted with these sets of model constants called M1 [118], M2 [118], M3 [119], M4 [120], and M5 [121] were compared with those measured experimentally in Fig. 3-3. The results showed that a reasonable prediction of the aforementioned quantities was obtained when the material constants of set M5, which were identified through analytical modeling of orthogonal cutting process together with metal cutting experiments, were utilized. Umbrello [12] conducted a FE analysis of orthogonal machining of TiAl6V4 alloy for conventional and high speed cutting regimes using DEFORM software. It was observed that for three different sets of Johnson-Cook constants, a reasonable prediction of machining forces and chip morphology was obtained only when an appropriate set of constants was employed.

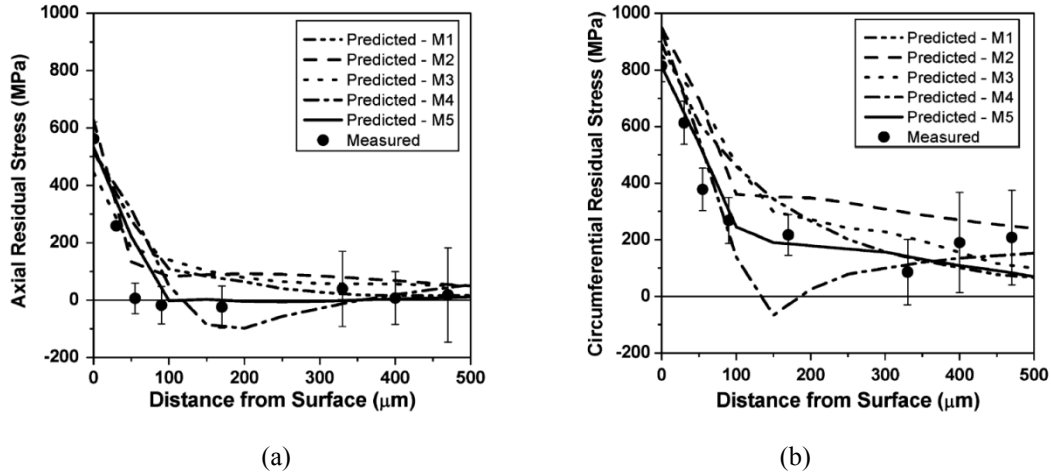


**Fig. 3-3.** Comparisons of measured and predicted (a) axial and (b) circumferential residual stresses (cutting speed  $V=200$  m/min, uncut chip thickness  $b=0.1$  mm, width of cut  $a_p=6$  mm) [57].

### 3.2.5. Frictional modelling

Modeling of frictional behavior at the tool-workpiece contact areas is a great challenge in finite element simulations. To date, the material behavior under high strain rates and temperatures at the tool-chip interface is not fully understood. Several attempts were made to measure friction coefficient in machining by using split-tool and photo elastic methods [71,83] and a ball-on-disk friction test using high-speed tribometer [19]. Based on the difficulty and inaccuracy of friction coefficient measurements, this coefficient was often determined by calibrating the FE model based on comparing and matching the FE results with the corresponding experimental ones.

Three main frictional models commonly used in FE modeling of machining processes are presented in Table 3-2. It is worth noting that Zorev model is considered as the most reliable one compared to Coulomb and shear friction models. In fact, Zorev model estimates the friction at the

**Table 3-2**

Friction models frequently employed in FE simulations of machining processes

Model	Formulae <sup>1</sup>
Coulomb friction model: Constant Coulomb friction coefficient at the entire tool-chip interface	$\tau = \mu \sigma_n$
Shear friction model <sup>2</sup> : Constant shear friction coefficient at the entire tool-chip interface	$\tau = m \tau_Y$
Zorev model <sup>3</sup> : Constant shear friction coefficient in sticking region and constant Coulomb friction coefficient in sliding region	$\tau = \tau_Y$ when $\mu \sigma_n \geq \tau_Y, 0 < x \leq l_p$ $\tau = \mu \sigma_n$ when $\mu \sigma_n < \tau_Y, l_p < x \leq l_c$

<sup>1</sup>  $\tau$  is shear stress,  $m$  shear friction factor,  $\mu$  Coulomb friction coefficient,  $\sigma_n$  normal compressive stress,  $\tau_Y$  shear flow stress,  $l_p$  and  $l_c - l_p$  are the lengths of the sticking and sliding regions

<sup>2</sup> Also known in the literature as Tresca shear friction model [60]

<sup>3</sup> Also known as the hybrid model, modified Coulomb friction model, Coulomb-Orowan friction model [20], or Coulomb-Tresca friction model [60]

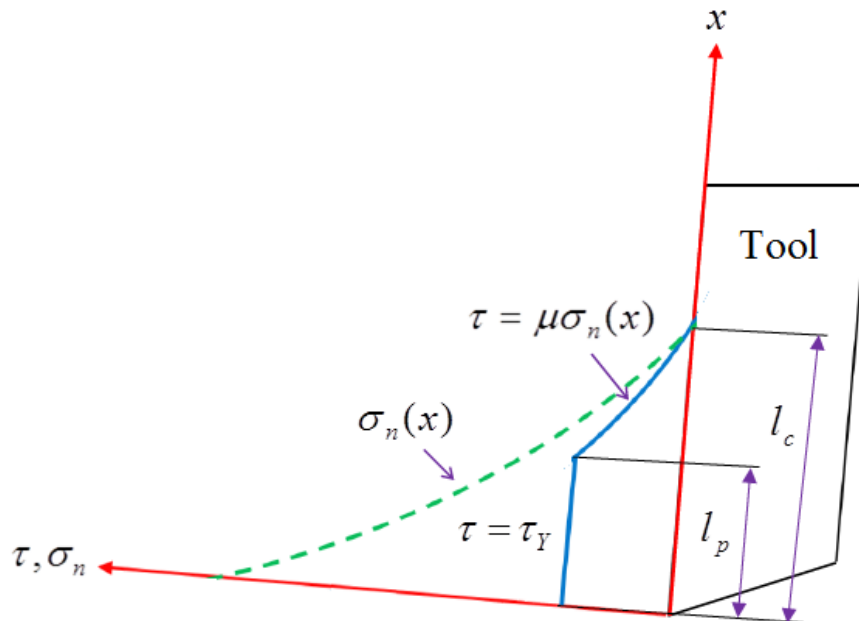


**Fig. 3-4.** Schematic distribution of shear stress on the tool rake face based on Zorev model provided in Table 3-2.

tool-chip interface more realistically by separating the contact region in two distinct zones known as sticking and sliding zones, as shown in Fig. 3-4. According to this model, the normal compressive stress  $\sigma_n$  on the tool rake face is very large, causing the friction stress  $\mu\sigma_n$  between the rake face and chip to exceed the shear flow stress  $\tau_y$  (instantaneous shear yield strength) of the workpiece ( $\mu\sigma_n \geq \tau_y$  where  $\mu$  is friction coefficient). This leads to the material to yield and deform plastically rather than slip at the contact surface. On the other hand, relative motion between the tool rake face and chip called slipping or sliding motion occurs based on Coulomb law when  $\mu\sigma_n < \tau_y$ . In mathematical representation, Zorev model is expressed as:

$$\tau = \min (\mu\sigma_n, \tau_y) \quad (3-10)$$

The correctness of Zorev's friction model was experimentally confirmed using the split tool method [122,123]. The effects of friction coefficient ( $\mu$ ) and shear stress limit ( $\tau_y$ ) in the Zorev model on finite element predictions were evaluated by a few research studies. Shi et al. [37] investigated the impact of friction coefficient on cutting outputs during orthogonal machining of AISI 4340 steel using Abaqus/Explicit software. They found that shear angle decreased and contact length, cutting force and maximum cutting temperature rose with increasing the friction coefficient. Later on, Arrazola and Ozel [16] examined the impact of shear stress limit on machining forces and temperature and also stress and velocity fields during orthogonal turning AISI 4340 steel using Abaqus/Explicit FE code. The results showed that for the ALE model with Eulerian boundaries, if the stress limit was higher than 500 MPa, approximately the same results were obtained for both Coulomb and Zorev models. In contrast, when the ALE model with Lagrangian boundaries was employed, the predicted forces rose with increasing the shear stress

limit. Accordingly, these studies demonstrate the importance of precisely calibrating the parameters of Zorev model so as to obtain accurate results.

Friction as a function of temperature and contact pressure, which is more realistic, is available in some FE packages such as Abaqus and DEFORM software. More complicated friction models that depend on the sliding velocity of the chip on the tool rake face as well as the contact pressure and temperature between the tool and chip, which are often obtained using extensive experimental tests, can be implemented into the commercial FE packages by developing subroutines.

### ***3.2.6. Chip formation modelling***

Chip formation/separation is the most challenging issue in the finite element simulation of cutting processes. There are two methods namely chip separation criterion method and pure deformation method to model chip formation/separation during machining [39].

The chip separation criterion method facilitates the chip formation process by reducing the element distortion during the simulation. This method uses either geometrical or physical separation criteria [44,99]. On the one hand, in the geometrical separation criterion, the chip is separated when the distance between the tool tip and the nearest node ahead of the tool tip exceeds a specified threshold. The geometrical criterion has no physical meaning because the magnitude of the afore-mentioned distance depends on the element size [124]. On the other hand, in the physical separation criterion, a pair of coincident nodes are separated (Node-Splitting Technique) or an element is deleted (Element Deletion Technique) when the critical value of a selected physical variable such as stress or equivalent plastic strain in the closest node or element to the tool tip is satisfied. In this case, a reliable, precise damage model is required. Although the

numerical prediction of machining forces was not generally affected by the chip separation criterion [40,125], the residual stresses were found to be strongly influenced by this criterion [99,125].

In contrast, the pure deformation method deals with the cutting process as a pure deformation process, in which nodes of the workpiece move on the rake and flank faces of the tool, and elements deform around the tool tip as the tool is moving forwards [44]. Consequently, no chip separation criterion is required. However, the deformation in the cutting process is large and involves severe element distortion. Therefore, Adaptive Remeshing and Rezoning/Remapping techniques should be employed in order to make the simulation progress. Fig. 3-5 summarises the available methods for chip formation modelling during the machining process.

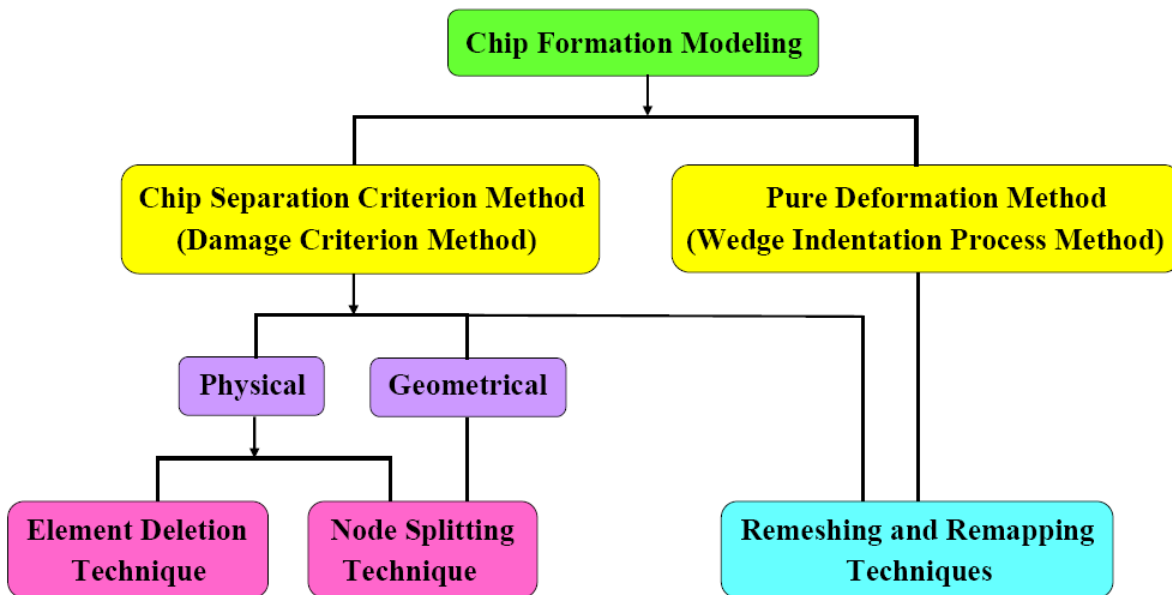


Fig. 3-5. The tree diagram summarizing the methods used for chip formation modelling.

### ***3.2.7. Thermo-mechanical coupling***

The turning operation is a coupled thermal-mechanical process, in which both mechanical and thermal analyses should be solved simultaneously. However, they are often solved in a staggered fashion for numerical convenience [115]. During a time increment, the stress analysis is first solved as an isothermal process based on the temperature distribution obtained from the previous increment. Then, the thermal analysis is solved as an isostress process and temperatures are updated based on the heat generated during this increment [114,115]. The thermo-mechanical coupling is conducted by the plastic deformation work [126] and the frictional work in Eq. (3-5) and the thermal softening effect on flow stress magnitudes in material constitutive models provided in Table 3-1 [126].

### ***3.2.8. Finite element formulations***

Various formulations have been used in finite element modeling of metal cutting processes, including pure Lagrangian (PL), updated Lagrangian (UL), Eulerian (E), and Arbitrary Lagrangian-Eulerian (ALE) formulations. In the pure and updated Lagrangian approaches, the mesh follows the material and the cutting process can be simulated from the incipient to the steady state. As a result, the chip formation process can be simulated without the need for a predefined chip shape. It is worth noting that the PL formulation requires a geometrical or physical criterion for modelling chip separation, which is not the case for the UL formulation as it takes advantage of a remeshing scheme. In contrast, in the Eulerian formulation, the mesh is fixed in space and the material flows through the mesh, eliminating the element distortion and reducing the computational time considerably. However, the Eulerian formulation needs a predefined chip and

residual stresses cannot be predicted because the material elasticity is not considered. To overcome these drawbacks, an ALE formulation is developed by taking advantage of both Lagrangian and Eulerian formulations. In the ALE formulation, the mesh can be fixed in space in some regions (Eulerian) and it can follow the material in others (Lagrangian), thus avoiding the frequent remeshing for the chip separation process [83].

### 3.2.9. *Explicit and Implicit solvers*

The FE software packages generally utilize Implicit or Explicit procedures to solve coupled dynamic, temperature-displacement equations governing the material behavior during metal cutting processes. The Implicit and Explicit solvers are compared in Table 3-3. Main characteristics of the available software packages used in metal cutting simulations are also provided in Table 3-4. The finite element modeling can be divided into two main steps: i. Cutting step and ii. Stress relaxation (residual stress) step. In most research studies, either Explicit or Implicit solution procedure is employed for modeling both cutting and stress relaxation processes.

**Table 3-3**

Explicit and Implicit time integration solvers

Explicit	Implicit
At each increment, requires the values of field variables and their time derivatives at <i>previous</i> increment.	At each increment, requires the values of field variables and their time derivatives at <i>previous and current</i> increments.
Requires a <i>large</i> number of very <i>small</i> time steps, in which <i>little</i> computation is performed.	Requires a <i>small</i> number of <i>large</i> time steps, in which <i>considerable</i> computation is performed.
Is <i>conditionally</i> stable - the size of the time step is limited by consideration of <i>numerical stability</i> .	Is <i>unconditionally</i> stable - the size of the time step is limited by consideration of <i>accuracy</i> .
A set of FE equations is solved <i>directly</i> to determine the solution at the end of each increment <i>without iteration</i> .	A set of FE equations is solved by <i>performing iterations</i> until a <i>convergence criterion</i> is satisfied for each increment.

**Table 3-4**

Finite element software packages utilized in metal cutting simulations

Software	Solver	FE formulation	Type of application
Abaqus/Explicit	Explicit	Updated Lagrangian and ALE	Specific purpose: Nonlinear dynamic, temperature-displacement problems
DEFORM	Implicit	Updated Lagrangian and ALE	Specific purpose: Metal forming problems
AdvantEdge	Explicit	Updated Lagrangian	Specific purpose: Machining problems
Marc	Implicit	Updated Lagrangian	General purpose
Forge	Implicit	Updated Lagrangian	Specific purpose: Metal forming problems
LS-DYNA	Explicit	Updated Lagrangian and ALE	General purpose
Abaqus/Standard	Implicit	Updated Lagrangian	General purpose
NIKE	Implicit	Updated Lagrangian	General purpose
SuperForm	Implicit	Updated Lagrangian	Specific purpose: Manufacturing problems
ANSYS	Implicit/ Explicit	Updated Lagrangian and ALE	General purpose

### 3.3. Comparison of commercial software and input models and materials

The finite element study of the orthogonal turning process has been begun using non-commercial (in-house) FE codes [12,46,50,57,118,119,127]. Gradually, these codes were replaced by commercial FE software packages because these commercial programs eliminate the time-consuming, computationally expensive process of coding, and consequently, facilitate the procedure of model building by their user-friendly graphical user interface. These packages contain the most common mechanical, thermal, material, frictional, and chip formation models, a library of various families of elements with different capabilities, a broad range of types of loads and boundary conditions, and adaptive remeshing and remapping schemes necessary for FE modeling of machining processes.

Many FE and FE-experimental studies simulating the output variables of the cutting and stress relaxation processes in orthogonal turning of metals using different software packages are summarized in Tables 3-5 and 3-6. The key information of input models and materials including the type of material, frictional and chip formation models, workpiece and tool materials as well as the employed software and outstanding result(s) of each research work are presented in these tables. A comparison of Tables 3-5 and 3-6 demonstrates that the number of analyses modeling the cutting step is roughly three times that of the works simulating both cutting and residual stress steps, showing the difficulty in, and therefore, the great value of, modeling residual stresses. Abaqus/Explicit and DEFORM FE packages were utilized much greater than the other software in modeling orthogonal turning operation. AdvantEdge and Marc programs were the second most popular FE software packages, followed by Forge FE program. Tungsten carbide was often used as the tool material in simulations, followed by coated Tungsten carbide, compared with the other tool materials such as PCBN and ceramics. The material constitutive models listed in these tables reveal that the original and modified versions of the Johnson-Cook model were extensively used for modeling of orthogonal turning. The Power law model was in the second place. When it comes to the friction model, all Coulomb, shear, and Zorev friction models with constant coefficients received much attention. In contrast, a few studies based on commercial software utilized temperature-dependent or velocity-dependent frictional models. Both pure deformation method and chip separation criterion were widely employed for simulating chip formation/separation in the orthogonal cutting process. Moreover, researchers showed much interest to use the Johnson-Cook and Cockroft-Latham damage models available in software packages for the chip separation criterion.

**Table 3-5**

A summary of FE studies simulating the cutting process of orthogonal turning of metals

<b>- Author(s)/ Reference</b> <b>- Publication year/ Software</b> <b>- Workpiece/Tool materials</b>	<b>- Material model</b> <b>- Friction model</b> <b>- Chip formation model</b>	<b>Outstanding result(s)</b>
- Shet and Deng [35] - 2000/ Abaqus/Explicit - AISI 4340 steel/ A rigid tool	- Power law model - Zorev friction model - A stress-based chip separation criterion	The overall temperature distribution in the chip was determined by plastic work rather than by friction along the tool-chip interface.
- Ozel and Altan [9] - 2000/ DEFORM - P20 mold steel/ Tungsten carbide	- Maekawa-Shirakashi-Usei model [128] - Zorev friction model - Pure deformation method	The constants of flow stress and friction models were determined by comparing predicted and measured cutting forces.
- Mamalis et al. [39] - 2001/ Marc - Mild steel/ Tungsten carbide	- Usei-Maekawa-Shirakashi model - Tangential force as a function of Coulomb friction coefficient, normal force, and relative sliding velocity - A distance-based separation criterion	Maximum magnitudes of plastic strain and temperature were at the secondary shear zone, while that of plastic strain rate was at the primary deformation zone.
- MacGinley and Monaghan [43] - 2001/ Forge - Inconel 718/ Uncoated and four coated TiN, TiC, Al <sub>2</sub> O <sub>3</sub> and TiN/Al <sub>2</sub> O <sub>3</sub> tungsten carbides	- Not mentioned - Coulomb friction model - Pure deformation method	Coated carbides had less tool wear at higher cutting speeds than uncoated ones. Cutting forces were lower for the coated tools than for the uncoated ones.
- Klocke et al. [64] - 2001/ DEFORM - AISI 1045 steel/ SiC-reinforced oxide ceramics	- Original and modified El-Magdand Treppmann's material models - Coulomb friction model - Pure deformation method	Continuous and discontinuous chips were modeled using the original and modified El-Magdand Treppmann's material models, respectively.
- Shi et al. [37] - 2002/ Abaqus/Explicit - AISI 4340 steel/ A rigid tool	- Power law model - Zorev friction model - A stress-based separation criterion	When friction coefficient increased, shear angle diminished and contact length, cutting force and maximum temperature rose. When rake angle increased, the reverse occurred.
- Yen et al. [78] - 2004/ DEFORM - AISI 1020 steel/ Tungsten carbide	- Usei-Maekawa-Shirakashi model - Shear friction model - Pure deformation method	Machining forces rose and normal and shear stresses on the rake face did not change as the edge radius of a hone tool and chamfer width and angle of a chamfer tool increased.

**Table 3-5**

A summary of FE studies simulating the cutting process of orthogonal turning of metals (*continued*)

<b>- Author(s)/ Reference</b> <b>- Publication year/ Software</b> <b>- Workpiece/Tool materials</b>	<b>- Material model</b> <b>- Friction model</b> <b>- Chip formation model</b>	<b>Outstanding result(s)</b>
- Guo and Yen [52] - 2004/ Abaqus/Explicit - AISI 4340 steel/ A rigid tool	- Johnson-Cook model - Zorev friction model - Johnson-Cook damage criterion	Discontinuous chips were produced due to the internal crack initiation and propagation in front of the tool and above the cutting edge, rather than from the free surface.
- Raczy et al. [23] - 2004/ LS-DYNA - Commercially pure Copper (C11000)/ Si <sub>3</sub> N <sub>4</sub> based ceramics	- Hydrodynamic and Johnson-Cook models - Inherent friction in the hydrodynamic model and also Coulomb friction model - Pure deformation method	The maximum equivalent strain, secondary deformation zone, and stresses in the primary deformation zone predicted by the Johnson-Cook model were larger than those obtained with the hydrodynamic model.
- Yen et al. [82] - 2004/ DEFORM - AISI 1045 steel/ TiN/Al <sub>2</sub> O <sub>3</sub> /TiC coated tungsten carbide	- A thermo-visco-plastic model [129] - Shear friction model - Pure deformation method	The two individual and composite coating layer models for the coated tool yielded almost identical predictions for cutting forces and chip geometry.
- Bil et al. [24] - 2004/ Marc, AdvantEdge, DEFORM - C15 steel/ High speed steel	- Marc, DEFORM: A tabulated flow stress model available in Marc ; AdvantEdge: Power law model - Marc, DEFORM: Shear friction model ; AdvantEdge: Coulomb friction model - Marc, AdvantEdge: Pure deformation method ; DEFORM: Cockroft-Latham damage criterion	Although the predicted cutting outputs could individually match with the experimental results for all three software packages, they failed to show satisfactory correlation with the measured ones altogether.
- Majumdar et al. [87] - 2005/ ANSYS - Free machining steel/ Tungsten carbide	- Oxley model - NOT mentioned - Pure deformation method	The maximum temperature in the tool increased as cutting speed rose and decreased when the convection heat transfer coefficient increased.
- Barge et al. [38] - 2005/ Abaqus/Explicit - AISI 4142 steel/ A rigid tool	- Johnson-Cook model - Frictionless contact - Johnson-Cook damage criterion	Mesh density and hourglass treatment affected chip geometry, but had less effect on cutting forces, temperature, and stress fields.

**Table 3-5**

A summary of FE studies simulating the cutting process of orthogonal turning of metals (*continued*)

<b>- Author(s)/ Reference</b> <b>- Publication year/ Software</b> <b>- Workpiece/Tool materials</b>	<b>- Material model</b> <b>- Friction model</b> <b>- Chip formation model</b>	<b>Outstanding result(s)</b>
- Grzesik et al. [48] - 2005/ AdvantEdge - AISI 1045 steel/ Uncoated, and TiC, TiC/TiN and TiN/Al <sub>2</sub> O <sub>3</sub> /TiC coated tungsten carbides	- Power law model - Coulomb friction model - Pure deformation method	Coatings caused that the maximum interface temperature occurred in the first part of the tool-chip contact length.
- Xie et al. [42] - 2005/ Abaqus/Explicit- Standard - AISI 1045 steel/ Tungsten carbide	- A model by Vohringer [130] - Coulomb friction model - Pure deformation method	By implementing a Python subroutine program, calculation of tool wear based on a wear rate model was realized.
- Wu et al. [44] - 2005/ Abaqus/Explicit - Aluminum/ Diamond	- A yield strength - plastic strain model - Coulomb friction model - Pure deformation method	The chip morphology modeled with a round-edge tool during cutting agreed well with those presented in the previous studies.
- Rhim and Oh [106] - 2006/ DEFORM - AISI 1045 steel/ High-speed steel (H11)	- A model based on a combination of models by [131] and [132] - Coulomb friction model - Cockroft-Latham damage criterion	The temperature rise in the shear band initiated dynamic recrystallization, which reduced the flow stress, leading to forming adiabatic shear bands and serrated chips.
- Baker [117] - 2006/ Abaqus/Standard - Ti-6Al-4V/ Tungsten carbide	- An idealized generic model - Frictionless contact - Pure deformation method	Cutting force decreased with cutting speed and then leveled off at high cutting speeds, which mainly caused by a change in the shear angle due to thermal softening.
- Ozel [83] - 2006/ DEFORM - Low carbon free-cutting steel/ Tungsten carbide	- A simplified Usei-Maekawa- Shirakashi model - Five models based on 'constant or variable' shear and/or Coulomb frictions - Pure deformation method	Among the friction models examined, the cutting variables had better agreement with the published experimental results when variable shear or Coulomb friction models were utilized.
- Guo et al. [10] - 2006/ Abaqus/Explicit - AISI 52100 steel/ PCBN	- Baumann-Chiesa-Johnson (B-C-J) [127,133] and Johnson-Cook (J-C) models - Zorev model - J-C damage model with J-C constitutive model and pure deformation method with B-C-J model	Contrary to the J-C model, the predicted chip morphology using the B-C-J model was consistent with the measured one.

**Table 3-5**

A summary of FE studies simulating the cutting process of orthogonal turning of metals (*continued*)

<b>- Author(s)/ Reference</b> <b>- Publication year/ Software</b> <b>- Workpiece/Tool materials</b>	<b>- Material model</b> <b>- Friction model</b> <b>- Chip formation model</b>	<b>Outstanding result(s)</b>
- Sartkulvanich et al. [71] - 2007/ DEFORM - AISI 1045 steel/ Tungsten carbide	- Power law model - Shear and Coulomb friction models - Pure deformation method	Changing the slope of thermal softening term over temperature in the power law model, contrary to strain and strain-rate hardening terms, changed the chip thickness.
- Liu and Melkote [109] - 2007/ Abaqus/Standard and ANSYS' remeshing module - Al5083-H116/ Diamond	- A modified Johnson-Cook model based on Taylor-based non-local theory of plasticity - Zorev friction model - Pure deformation method	Edge radius contributed to the size effect by changing material flow pattern around the tool tip by expanding plastic shear zone and by dissipating a higher energy.
- Coelho et al. [47] - 2007/ Abaqus/Explicit - AISI 4340 steel/ Uncoated and monolayer coated TiAlN, TiAlN-nanocoating and AlCrN PCBN	- Johnson-Cook model - Zorev friction model - Pure deformation method	The TiAlN-nanocoating tool performed better in terms of tool wear and surface roughness due to a combination of high hardness in the cutting temperature range and the presence of an oxidizing layer.
- Filice et al. [25] - 2007/ DEFORM - AISI 1045 steel/ Tungsten Carbide	- Oxley model - Five models based on 'constant or variable' shear and/or Coulomb frictions - Pure deformation method	Mechanical outputs including cutting forces and tool-chip contact length were not sensitive to the friction model as much as thermal outputs such as cutting temperature.
- Hortig and Svendsen [53] - 2007/ Abaqus/Explicit - Inconel 718/ A rigid tool	- Johnson-Cook model - Coulomb friction model - A damage model based on equivalent plastic strain	Chip geometry and cutting forces were dependent strongly on the element size and orientation.
- Qian and Hossain [79] - 2007/ AdvantEdge - AISI 52100, AISI H13, AISI D2, and AISI 4340 steels/ PCBN	- Power law model - Coulomb friction model - Pure deformation method	The highest cutting and feed forces were accompanied by cutting AISI 4340 and AISI 52100 steels, respectively. The lowest cutting and feed forces were obtained for cutting AISI D2 steel.
- Haglund et al. [72] - 2008/ Abaqus/Explicit - AISI 4140 steel/ Tungsten carbide	- Johnson-Cook model - Six models based on 'constant and temperature-dependent' Coulomb friction coefficients and shear stress limits - Pure deformation method	Among the friction models investigated, using a temperature-dependent friction coefficient provided more precise results.

**Table 3-5**

A summary of FE studies simulating the cutting process of orthogonal turning of metals (*continued*)

<b>- Author(s)/ Reference</b> <b>- Publication year/ Software</b> <b>- Workpiece/Tool materials</b>	<b>- Material model</b> <b>- Friction model</b> <b>- Chip formation model</b>	<b>Outstanding result(s)</b>
- Subbiah and Melkote [28] - 2008/ Abaqus/Explicit - Al2024-T3/ Polycrystalline diamond (PCD)	- Johnson-Cook model - Zorev friction model - Johnson-Cook damage criterion	The tensile character of all stress components during cutting were consistently lower for the honed tool than the sharp tool.
- Bonnet et al. [74] - 2008/ Abaqus/Explicit - AISI 316L steel/ TiN coated tungsten carbide	- Johnson-Cook model - Velocity-dependent Coulomb model - Pure deformation method	Contrary to a large constant Coulomb Friction Coefficient (CFC), a velocity-dependent CFC and a small constant CFC produced accurate results.
- Woon et al. [110] - 2008/ Abaqus/Explicit - AISI 4340 steel/ Tungsten carbide	- Johnson-Cook model - Zorev friction model - Pure deformation method	The ratio of undeformed chip thickness to tool edge radius greatly affected the chip formation and stress distributions.
- Umbrello [12] - 2008/ DEFORM - Ti-6Al-4V/ Tungsten carbide	- Johnson-Cook model - Shear friction model - Cockroft-Latham damage criterion	A reasonable prediction of cutting force and chip morphology was obtained when an appropriate set of constants in the Johnson-Cook equation was used.
- Calamaz et al. [60] - 2008/ Forge - Ti-6Al-4V/ Tungsten Carbide	- TANH model (Upgraded Johnson-Cook) - Zorev friction model - Pure deformation method and also Cockroft-Latham damage criterion	Contrary to the Johnson-Cook model, the TANH model considering the material strain softening effect could predict segmented chips under low cutting speeds and feeds.
- Khalili and Safaei [45] - 2009/ DEFORM - AISI 1045 steel/ Tungsten carbide	- Oxley model - Zorev and shear friction models - Pure deformation method	The influence of chamfer width and angle was more pronounced on the thrust force than the cutting force.
- Lorentzon et al. [31] - 2009/ Marc - Inconel 718/ Tungsten carbide	- A piecewise plasticity model - Zorev friction model - Fracture strain energy (Cockroft-Latham) and accumulated plastic strain models	A transition from continuous chips to segmented chips was caused by both thermal softening and material fracture.
- Kountanya et al. [13] - 2009/ DEFORM - AISI 52100 steel/ PCBN	- A coupled model based on a combination of models by [107] and [134] - Zorev friction model - Pure deformation method	Edge radius did not change chip geometry parameters. Cutting forces decreased and chip formation frequency linearly increased with the cutting speed.

**Table 3-5**A summary of FE studies simulating the cutting process of orthogonal turning of metals (*continued*)

- Author(s)/ Reference - Publication year/ Software - Workpiece/Tool materials	- Material model - Friction model - Chip formation model	Outstanding result(s)
- Davim et al. [14] - 2009/ AdvantEdge - AISI D2 steel/ Tungsten carbide	- Johnson-Cook model - Coulomb friction model - Pure deformation method	The friction coefficient did not considerably affect the difference between the experimental and simulated cutting force compared with the thrust force.
- Deng et al. [111] - 2009/ DEFORM - AISI 1020 steel/ Tungsten carbide	- Usei-Maekawa-Shirakashi model - Shear friction model - Cockroft-Latham damage criterion	The size of burr declined by decreasing the exit angle, rake angle, and feed rate, and also by sharpening the cutting edge.
- Al-Zkeri et al. [30] - 2009/ DEFORM - AISI 4142H steel/ TiAlN coated tungsten carbide	- Johnson-Cook model - Shear friction model - Pure deformation method	Predicted cutting and thrust forces agreed well with the experimental ones when a tool with a larger hone radius was used.
- Ranganath et al. [29] - 2009/ Abaqus/Explicit - IN100/ Tungsten carbide and CBN	- A 'piece-wise' Johnson-Cook model - Not mentioned - Pure deformation method	The ratio of the edge radius to uncut chip thickness was the most critical parameter in controlling plastic strains in the machined surface.
- Klocke et al. [77] - 2010/ DEFORM - AISI 316L steel/ (Ti <sub>0.35</sub> ,Al <sub>0.65</sub> )N coated tungsten carbides	- Johnson-Cook model - Shear friction model - Pure deformation method	High contact stress due to chip sliding on the rake face led to partial removal of coating material. Large positive rake angles reduced the tendency towards coating delamination.
- Sima and Ozel [61] - 2010/ DEFORM - Ti-6Al-4V/ Uncoated and TiAlN coated tungsten carbides	- Three modified Johnson-Cook models - Three contact regions based on shear and Coulomb friction models - Pure deformation method	Flow softening increased the degree of chip serration but produced more curved chips due to weakening the strain-hardening influence.
- Calamaz et al. [62] - 2010/ Forge - Ti-6Al-4V/ Tungsten carbide	- TANH model - Coulomb friction model - Pure deformation method	The TANH model significantly improved the prediction of geometrical chip characteristics, compared with the Johnson-Cook model.
- Arrazola and Ozel [16] - 2010/ Abaqus/Explicit - AISI 4340 steel/ Tungsten carbide	- Johnson-Cook model - Both Coulomb and Zorev models - Pure deformation method	Limited shear stress should be used with caution because it affected cutting outputs considerably.

**Table 3-5**

A summary of FE studies simulating the cutting process of orthogonal turning of metals (*continued*)

<b>- Author(s)/ Reference</b> <b>- Publication year/ Software</b> <b>- Workpiece/Tool materials</b>	<b>- Material model</b> <b>- Friction model</b> <b>- Chip formation model</b>	<b>Outstanding result(s)</b>
- Akbar et al. [33] - 2010/ Abaqus/Explicit - AISI 4140 steel/ Tungsten carbide	- Johnson-Cook model - Zorev friction model - Johnson-Cook damage criterion	Accuracy of outputs of the FE model depended strongly on the magnitude of heat partition into the cutting tool.
- Jiang et al. [15] - 2010/ AdvantEdge - Al7050-T7451/ Kennamattel top-notch inserts	- Power law model - Friction coefficient as a function of rake angle and machining forces - Pure deformation method	The use of the Power-law material model of Al7050-T7451 obtained by the SHPB test provided accurate simulated machining forces and chip thickness.
- Calamaz et al. [63] - 2011/ Forge - Ti-6Al-4V/ Tungsten carbide	- A modified Johnson-Cook (J-C) model - Low and high Coulomb frictions in turn for sliding and sticking contacts - Pure deformation method	Contrary to the original J-C model, the modified J-C model with a strain softening term predicted cutting process outputs in good agreement with the experimental ones.
- Uzun and Aslantas [17] - 2011/ DEFORM - AISI 4340 steel/ Uncoated, TiCN/Al <sub>2</sub> O <sub>3</sub> /TiN and Al <sub>2</sub> O <sub>3</sub> coated tungsten carbides	- Johnson-Cook model - Shear friction model - Pure deformation method	Cutting temperature in the workpiece, tool-chip contact length, and stress in the tool were in turn higher, lower, and higher when cutting was done with the Al <sub>2</sub> O <sub>3</sub> coated tool.
- Vaziri et al. [41] - 2011/ Abaqus/Explicit - AISI 1045 steel/ Tungsten carbide	- Johnson-Cook model - Zorev friction model - Both pure deformation method and Johnson-Cook damage criterion	Cutting process outputs obtained by damage model were more reasonable with less computational cost and less software crash compared to pure deformation method.
- Long and Guo [81] - 2012/ Abaqus/Explicit - Ti-6Al-4V, AISI 4340 steel and Al2024-T3/ A rigid tool	- Johnson-Cook model - Coulomb friction model - A model based on equivalent plastic strain	Workpiece material properties significantly affected burr formation and type of burrs including positive and negative burrs.
- Klocke et al. [54] - 2013/ DEFORM - AISI 316L steel/ Tungsten Carbide	- Johnson-Cook model - Zorev friction model - Cockroft-Latham damage criterion	An inverse approach was employed to obtain the constants of Johnson-Cook material and Cockroft-Latham damage models by comparing predicted and measured results.
- Jiang et al. [19] - 2013/ AdvantEdge - AISI D2 steel/ TiAlN coated carbide	- Power law model - Coulomb friction model - Failure strain model	Maximum shear stress between the coating and substrate of the tool was on the cutting edge close to the flank face of the tool.

**Table 3-5**

A summary of FE studies simulating the cutting process of orthogonal turning of metals (*continued*)

<b>- Author(s)/ Reference</b> <b>- Publication year/ Software</b> <b>- Workpiece/Tool materials</b>	<b>- Material model</b> <b>- Friction model</b> <b>- Chip formation model</b>	<b>Outstanding result(s)</b>
- Xi et al. [58] - 2013/ Abaqus/Explicit - Ti-6Al-4V/ Tungsten carbide	- Johnson-Cook model - Coulomb friction model - Johnson-Cook damage criterion	Increasing initial workpiece temperature reduced the cutting force, whereas it slightly affected the frequency of the force variation.
- Ducobu et al. [55] - 2014/ Abaqus/Explicit - Ti-6Al-4V/ Tungsten carbide	- Johnson-Cook (J-C) and TANH models - Coulomb friction model - A tensile failure model	Among the three models including ALE with TANH model, Lagrangian with J-C model, Lagrangian with TANH model, the 3 <sup>rd</sup> model produced more accurate saw-tooth chips.
- Atlati et al. [20] - 2014/ Abaqus/Explicit - AA2024-T351/ Tungsten carbide	- Johnson-Cook model - Zorev friction model - Johnson-Cook damage criterion	Different couples of velocity-dependent heat partition and independent heat transfer coefficients could give the same heat flux transmitted into the tool.
- Preš et al. [73] - 2014/ Abaqus/Explicit - AISI 1045 steel/ Tungsten carbide	- Johnson-Cook model - Coulomb friction model - Ductile damage criterion	Cutting speed had a great effect on the length of burr, while it had negligible impact on the burr decrease and burr height.
- Menezes et al. [80] - 2014/ LS-DYNA - Aluminum/ Steel	- An elastic visco-plastic model in LS-DYNA [135] - Coulomb friction model - A model proposed by Lemaitre [136]	Cutting force varied with the rake angle and friction coefficient more significantly than with the cutting velocity.
- Paturi et al. [46] - 2014/ DEFORM - AA7075-T6/ Tungsten carbide	- Modified Johnson-Cook and modified Zerilli-Armstrong models - Shear friction model - Pure deformation method	Predicted cutting results agreed well with the experimental ones at moderate cutting speeds, while the formulated models might not work effectively at high cutting speeds.
- Haddag et al. [113] - 2015/ Abaqus/Explicit - AA2024-T351/ Tungsten carbide	- Johnson-Cook model - Zorev friction model - Johnson-Cook damage criterion	A piece-wise evolution law in terms of sliding velocity at the tool-chip interface was proposed for the heat conductance.
- Ducobu et al. [56] - 2015/ Abaqus/Explicit - Ti-6Al-4V/ Tungsten carbide	- TANH model - Coulomb friction model - A tensile failure model	The results of a model with adaptive mass scaling were very similar to those of a model without it, with much less computational time of about 70%.

**Table 3-5**

A summary of FE studies simulating the cutting process of orthogonal turning of metals (*continued*)

<b>- Author(s)/ Reference</b> <b>- Publication year/ Software</b> <b>- Workpiece/Tool materials</b>	<b>- Material model</b> <b>- Friction model</b> <b>- Chip formation model</b>	<b>Outstanding result(s)</b>
- Daoud et al. [21] - 2015/ DEFORM - Al2024-T3, Al6061-T6, and Al7075-T6/ Tungsten carbide	- Johnson-Cook model - Shear friction model - Pure deformation method and Cockroft-Latham damage criterion	The material constants determined using an inverse approach predicted the flow stress more accurate than that reported in the literature.
- Daoud et al. [68] - 2015/ DEFORM - Al2024-T3/ Tungsten carbide	- Johnson-Cook model - Shear friction model - Pure deformation method and Cockroft-Latham damage criterion	Machining with the rake angle of 0° was the nearest cutting condition to the assumption in the analytical model used for estimating the physical quantities such as strains and stresses in the primary shear zone.
- Jomaa et al. [84] - 2016/ DEFORM - Aluminum alloys 6061-T6 and 7075-T651 and AISI 4340 steel/ Tungsten carbide, Al <sub>2</sub> O <sub>3</sub> /TiC and TiN coated ceramics	- Marusich model - Shear friction model - Pure deformation method for AA6061-T6 and Cockroft-Latham damage criterion for AA7075-T651 and AISI 4340 steel	Oxley and Loewen-Shaw temperature models used in the analytical inverse method considerably affected the identified material constants and thereafter predicted dynamic response and machining data.
- Kara et al. [137] - 2016/ DEFORM - AISI 316L steel/ Uncoated, TiCN/Al <sub>2</sub> O <sub>3</sub> /TiN, Al <sub>2</sub> O <sub>3</sub> coated Tungsten carbides	- Johnson-Cook model - Shear friction model - Pure deformation method	Artificial Neural Network is a suitable alternative for other conventional modelling techniques in prediction of cutting temperature.
- Sadeghifar et al. [51] - 2016/ Abaqus/Explicit - AISI 4340 steel/ Tungsten carbide	- Johnson-Cook model - Zorev friction model - Pure deformation method	Low feed and edge radius, a roughly small cutting speed and a medium rake angle minimized cutting temperature in the presence of a confined resultant cutting force.

**Table 3-6**

A summary of FE studies simulating both cutting and stress relaxation processes of orthogonal turning of metals

<b>- Author(s)/ Reference</b> <b>- Publication year/ Software</b> <b>- Workpiece/Tool materials</b>	<b>- Material model</b> <b>- Friction model</b> <b>- Chip formation model</b>	<b>Outstanding result(s)</b>
- Liu and Gua [36] - 2000/ Abaqus/Explicit - 304 stainless steel/ A rigid tool	- Power law model - Zorev friction model - A model based on effective plastic strain	Residual stresses were significantly affected by the sequential cuts, whereas cutting forces, temperature, and chip geometry were slightly influenced.
- Shi and Liu [66] - 2004/ Abaqus/Explicit - HY100 steel/ Tungsten Carbide	- Litonski-Batra, power law, Johnson-Cook, and Bodner-Partom models - Zorev model - A model based on equivalent plastic strain	Machining forces, temperature, and stresses had consistent patterns for all the material models except the Litonski-Batraone model. Predicted chip curls and magnitudes and sign of residual stresses in machined surfaces were different for the four models.
- Outeiro et al. [11] - 2006/ DEFORM - AISI 316L steel/ Uncoated and TiC/Al <sub>2</sub> O <sub>3</sub> /TiN coated tungsten carbides	- Johnson-Cook model - Shear friction model - Cockroft-Latham damage criterion	Superficial residual stresses increased with cutting speed, uncut chip thickness, and tool cutting edge radius and decreased with rake angle.
- Salio et al. [98] - 2006/ Marc - Inconel 718 (AISI 316L steel used for validation)/ TiC/TiCN/TiN coated tungsten carbide	- Johnson-Cook model - A modified Coulomb friction model - Pure deformation method	Among three cases of two sequential cuts with the same total depth of cut (DoC), the superficial residual stress after the second cut was the lowest when the DoCs of the first and second cuts were equal.
- Hua et al. [138] - 2006/ DEFORM - AISI 52100 steel/ PCBN	- A hardness-based model [107] - Shear friction model - Brozzo fracture criterion	Higher feed rate, workpiece hardness, and tool edge radius as well as a chamfer plus hone cutting edge led to more compressive residual stresses.
- Nasr et al. [50] - 2007/ Abaqus/Explicit - AISI H13 steel/ PCBN ; AISI 316L steel/ Tungsten carbide ; AISI 52100 steel/ PCBN ; AISI 4340 steel/ Ceramics	- Johnson-Cook model - Coulomb friction model - Pure deformation method	Impact of initial yield strength on residual stresses was opposite to that of strain hardening parameters.
- Ozel and Zeren [89] - 2007/ Abaqus/Explicit - AISI 4340 steel/ Tungsten carbide	- Johnson-Cook model - Zorev friction model - Pure deformation method	Predicted stresses when the tool had contact with the workpiece were closer to the experimental ones than those when the tool was unloaded.

**Table 3-6**

A summary of FE studies simulating both cutting and stress relaxation processes of orthogonal turning of metals  
(continued)

- Author(s)/ Reference - Publication year/ Software - Workpiece/Tool materials	- Material model - Friction model - Chip formation model	Outstanding result(s)
- Nasr et al. [49] - 2007/ Abaqus/Explicit - AISI 316L steel/ Tungsten carbide	- Johnson-Cook model - Coulomb friction model - Pure deformation method	Increasing edge radius induced higher tensile residual stresses in the near-surface layer, whereas it had almost no impact on the layer's thickness.
- Umbrello et al. [57] - 2007/ DEFORM - AISI 316L steel/ Tungsten Carbide	- Johnson-Cook model - Shear friction model - Cockroft-Latham damage criterion	Reasonable predictions of cutting forces, chip morphology, temperature distributions and residual stresses were achieved when an appropriate set of material constants was chosen.
- Nasr et al. [97] - 2008/ Abaqus /Explicit, Standard - AISI H13 steel/ PCBN ; AISI 316L steel/ Tungsten carbide ; AISI 52100 steel/ PCBN ; AISI 4340 steel/ Ceramics	- Johnson-Cook model - Coulomb friction model - Pure deformation method	A modified FE approach in which explicit and implicit solvers were in turn utilized for cutting (C) and residual stress (RS) steps provided the RS much more time-saving than the traditional approach in which explicit solver was used for both steps.
- Ramesh and Melkote [26] - 2008/ Abaqus/Explicit - AISI 52100 steel/ cBN	- Johnson-Cook model - Zorev friction model - Pure deformation method	Predicted residual stresses were closer qualitatively to the experimental ones when the white layer formation was included in the cutting simulation.
- Mabrouki et al. [27] - 2008/ Abaqus/Explicit - A2024-T351/ Tungsten carbide	- Johnson-Cook model - Coulomb friction model - Johnson-Cook damage criterion	The higher the cutting speed was, the more noticeable the segmentation geometry of the chip was.
- Maranhão and Davim [76] - 2010/ AdvantEdge - AISI 316 steel/ TiCN/Al <sub>2</sub> O <sub>3</sub> /TiN coated tungsten carbide	- Johnson-Cook model - Coulomb friction model - Pure deformation method	The lower the feed rate was, the smaller the residual stresses were. Maximum tensile and compressive circumferential residual stresses were larger for a smaller rake angle. Cutting edge radius did not affect the circumferential residual stresses.
- Mohammadpour et al. [32] - 2010/ SuperForm - AISI 1045 steel/ Tungsten carbide	- Johnson-Cook model - Zorev friction model - Pure deformation method	Maximum value of tensile residual stresses generally increased with increasing cutting speed and feed rate.

**Table 3-6**

A summary of FE studies simulating both cutting and stress relaxation processes of orthogonal turning of metals  
(continued)

<b>- Author(s)/ Reference</b> <b>- Publication year/ Software</b> <b>- Workpiece/Tool materials</b>	<b>- Material model</b> <b>- Friction model</b> <b>- Chip formation model</b>	<b>Outstanding result(s)</b>
- Schulze et al. [100] - 2010/ Abaqus/Standard - AISI 1045 steel/ Tungsten carbide	- A model consisting of thermal and athermal parts - Coulomb friction model - Pure deformation method	A higher cutting edge radius led to deeper tensile residual stresses. Residual stresses were strongly influenced by the initial strength and work hardening of the material.
- Sanchez et al. [34] - 2011/ Abaqus/Explicit, Standard - AISI 316L steel/ Tungsten carbide	- Johnson-Cook model - Coulomb friction model - Pure deformation method	All the three types of tool wear namely flank, rounded cutting edge and crater wears increased residual stresses, compared to the reference geometry.
- Tang et al. [90] - 2011/ Abaqus/Explicit - AISI D2 steel/ cBN	- Johnson-Cook model - Coulomb friction model - Chip separation criterion	The lower the cutting temperature was, the smaller the compressive residual stress was.
- Moussa et al. [18] - 2012/ Abaqus/Explicit - AISI 316L steel/ TiCN/Al <sub>2</sub> O <sub>3</sub> /TiN coated tungsten carbide	- Johnson-Cook model - Zorev model - Pure deformation method	The level of tensile residual stress in the machined subsurface was lower when a high cutting speed and a low depth of cut were utilized.
- Nasr [22] - 2015/ Abaqus/Explicit - AISI 1045 steel/ Tungsten carbide	- Johnson-Cook model - Coulomb friction model - Johnson-Cook damage criterion	The second cut almost had no impact on the shear angle and contact length, while it led to slightly higher temperatures and smaller cutting forces, lower surface tensile residual stresses in the cutting direction and a smaller thickness of tensile layer.
- Sadeghifar et al. [139] - 2017/ Abaqus/Explicit - 300M steel/ Ceramics	- Johnson-Cook model - Zorev friction model - Pure deformation method	The percentage improvement in the objective function in unconstrained optimization problems of residual stresses, cutting temperature, machining forces, and material removal rate is greater than that in optimization problems with constraints on the afore-mentioned response variables.

### 3.4. Sources of error

A number of reasons for discrepancies between finite element predictions and experimental measurements of the machining and surface integrity variables were mentioned in the literature.

Most of the sources of error were reported to be due to:

- Using a simple, inaccurate material constitutive (flow stress) model [13,22,30,42,74,78,83]
- Employing an approximate friction model between the tool and workpiece during machining [13,22,30,33,42,48,49,54,71,78]
- Utilizing an inaccurate material damage model [81]
- Conducting remeshing (and remapping) schemes leading to computational error [49,78]
- Considering the workpiece as a fully homogeneous material [49,54]
- Modeling workpiece as a flat specimen [71]
- Ignoring tool wear during simulations which causes a change in the tool edge radius [49]
- Failing to reach a steady-state condition due to the restricted workpiece length [100]
- Lacking the use of temperature-dependent thermal and mechanical properties [30]
- Lacking a precise 2D plane strain condition in experimental set-ups [71,74]

It can also be added to the above list that in a number of research studies, the predictions did not agree well with the measurements at very low [17] or high [62] cutting speeds, which was attributed to the fact that the employed material constitutive model lost its validity at these levels of cutting speeds [17].

### 3.5. The present finite element modeling

#### 3.5.1. Modeling, element, mesh, and boundary conditions

In the present research, the finite element model of orthogonal turning of 300M steel material has been developed in Abaqus software. Element CPE4RT, which is a 4-nodes isoparametric continuum element with bilinear displacement and temperature is used to mesh both workpiece and tool. This element uses a reduced integration scheme with hourglass control in order to eliminate hourglassing modes resulting from the use of one integration point [140]. The workpiece is meshed using the Structured technique and Enhanced hourglass control, while the tool is meshed using the Free technique and Advancing Front algorithm. The tool material is always much stiffer than the workpiece material, and consequently, can be modeled as a rigid body in two cases. When temperature distribution is sought within the tool while stress distribution is not of concern, the tool should be defined as "Deformable" and "Rigid Body" (Case I), as carried out in the present research. On the other hand, when both temperature and stress distributions inside the tool are not important to the analyst, the tool should be defined as "Discrete Rigid" and "Rigid Body" (Case II). Table 3-7 summarizes the two cases for modeling a rigid tool in Abaqus/Explicit. A reference point is assigned to the tool in order to capture the forces generated during the machining process. A 'Rigid Body' constraint is then applied to the tool to provide a rigid body motion.

**Table 3-7**

Comparison of the required features for modeling a rigid tool

Case	Feature	Objective	
		Temperature distribution	Stress distribution
I	Deformable and Rigid Body	Yes	No
II	Discrete Rigid and Rigid Body	No	No

The thermal and mechanical Boundary Conditions (BCs) are applied as illustrated in Fig 3-6. The cutting tool can move in the horizontal direction with a velocity of  $V_C$ , while it has no vertical translation ( $U_y=0$ ) and no rotation about Z axis ( $UR_z=0$ ). The workpiece is fixed in both horizontal ( $U_x=0$ ) and vertical ( $U_y=0$ ) directions at the bottom and left sides. The ambient temperature ( $T_a = 20\text{ }^\circ\text{C}$ ) is prescribed for the sides of the tool and workpiece far enough from the cutting zone. It is worth noting that using these BCs (considered as pure Lagrangian BCs), the cutting process is simulated from the incipient to the steady state. In addition, the chip shape is not required to be known a priori.

During the relaxation step in the residual stress analysis, the contact between the tool and workpiece is removed by setting it as 'Inactive' boundary condition. Then, the tool is retracted and the mechanical BCs  $U_x=U_y=0$  are removed from the left side of the workpiece (become inactive) so as to allow the workpiece material to relax by cooling down to room temperature. This cooling process is carried out using a Convection heat transfer by applying a 'Film Coefficient' (h) (Eq. (3-9)) to the workpiece including the chip.

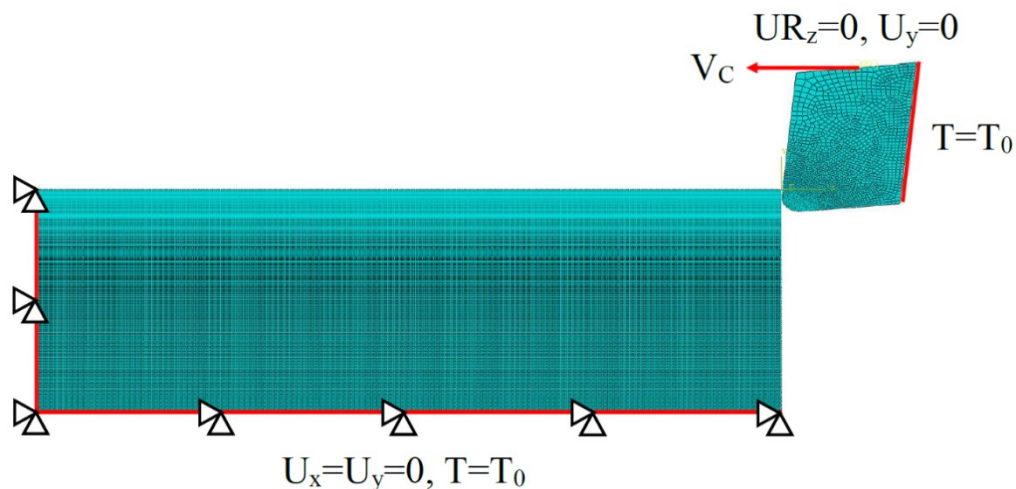


**Fig. 3-6.** Thermal and mechanical boundary conditions during the cutting process.

### 3.5.2. Numerical integration and time increment

The dynamic explicit scheme is used in Abaqus/Explicit to perform the time integration. At each time increment (time step), as mentioned previously, the explicit scheme requires the values of field variables and their time derivatives at the previous increment. A set of finite element equations is directly solved to determine the solution at the end of each increment without iteration. The explicit time integration solver needs a large number of very small time steps, in which little computation is performed, making it suitable for short-duration dynamic problems including machining processes.

The central difference method is one of the numerical integration techniques that has been successfully used with the explicit method to solve metal cutting problems. In the central difference method, the time step  $\Delta t$  should be less than or equal to the time needed for both stress and thermal waves to propagate across the smallest element in the system. If  $\Delta t$  is too large, the explicit method fails, whereas if it is unnecessarily small, the computation becomes too expensive. As a result, the integration scheme should be conditionally stable. The critical stable time increment is definitely a very important parameter in metal cutting simulations which affects the run time and convergence of the program. The critical stable time increment for a pure mechanical analysis  $\Delta t_{M-cr}$  and a pure thermal analysis  $\Delta t_{T-cr}$  are expressed by [97,141]:

$$\Delta t_{M-cr} \cong \frac{L_{\min}}{c_d}, \quad \Delta t_{T-cr} \cong \frac{L_{\min}^2}{2\alpha} \quad (3-11)$$

where  $L_{\min}$ ,  $c_d$ , and  $\alpha$  are the smallest element dimension in the model, the dilatational wave speed, and the thermal diffusivity of the material, respectively.  $c_d$  and  $\alpha$  for isotropic materials are given by:

$$c_d = \sqrt{\frac{E(1-\nu)}{\rho(1+\nu)(1-2\nu)}}, \alpha = \frac{k}{\rho c} \quad (3-12)$$

in which  $E$ ,  $\nu$ ,  $\rho$ ,  $k$  and  $c$  are Young's modulus of elasticity, Poisson's ratio, density, thermal conductivity, and specific heat capacity, respectively. Substituting for  $c_d$  and  $\alpha$  from Eq. (3-12) into Eq. (3-11),  $\Delta t_{M-cr}$  and  $\Delta t_{T-cr}$  are obtained as:

$$\Delta t_{M-cr} \cong L_{\min} \sqrt{\frac{\rho(1+\nu)(1-2\nu)}{E(1-\nu)}}, \Delta t_{T-cr} \cong L_{\min}^2 \frac{\rho c}{2k} \quad (3-13)$$

In a coupled thermo-mechanical analysis such as in metal cutting processes, the overall time step should satisfy the following inequality

$$\Delta t \leq \min (\Delta t_{M-cr}, \Delta t_{T-cr}) \quad (3-14)$$

In the majority of thermo-mechanical problems, we have  $\Delta t_{M-cr} < \Delta t_{T-cr}$  and, therefore, the mechanical analysis governs the overall stability limit, that is  $\Delta t \cong \Delta t_{M-cr}$ . This value for  $\Delta t$  is not a conservative estimate and, in general, the actual stable time increment chosen by Abaqus/Explicit is less than this estimate by a factor between  $1/\sqrt{2}$  and 1 for two-dimensional simulations [141].

In this research,  $L_{\min}$  is equal to  $0.331 \mu m$  at the beginning of the cutting process. Consequently, the initial magnitudes of  $\Delta t_{M-cr}$  (without considering mass scaling effect) and  $\Delta t_{T-cr}$  are calculated as  $5.7224 \times 10^{-11}$  s and  $5.1181 \times 10^{-9}$  s, respectively, confirming that the mechanical analysis governs the overall stability limit of this turning process.

### **3.6. Optimal magnitudes of numerical parameters**

Finite element models developed in Abaqus for simulation of cutting processes are prone to premature termination owing to excessive distortion of elements or an excess of critical stable time increment. Accordingly, various options available in Abaqus software should be fine tuned in order to obtain accurate simulation results without premature termination of the program and having high run time. This includes simultaneously optimizing the number (size) and arrangement of the elements, the adaptive remeshing parameters, and mass scaling factor.

#### ***3.6.1. Size and arrangement of elements***

If the size and arrangement of elements are not properly determined, it is very likely that the FE program will terminate prematurely.

Increasing the number of elements to a certain extent, which is equivalent to decreasing the size of elements, has some advantages and shortcomings as follows:

- It provides a better discretization and therefore more accurate results.
- It declines critical stable time increment, which leads to increasing the probability of premature termination due to exceeding the critical stable time increment (Eq. (3-13)) and augmenting the number of increments inducing round-off errors.
- It raises the number of nodes, thus increasing the computations and the run time of the simulation process.

On the other hand, the arrangement of elements in the workpiece is also as important as the number of elements. Considering that orthogonal turning simulations are conducted for a rectangular workpiece being cut along its length, the arrangement of elements should be such that the ratio of the number of elements to the side dimension is larger for the width of the workpiece than that for the length. Therefore, the number and the arrangement of elements should be optimized to reach an accurate, computationally efficient solution. In the present FE model, the number and arrangement of elements are displayed in Fig. 3-7, showing a strong mesh refinement at and around the cutting zone. With the penetration of the cutting tool into the workpiece, the elements along the workpiece width stretch, whereas the elements along the length and especially at the top of the workpiece contract during cutting. This elongation causes the elements to become larger, particularly at longer machining durations. Consequently, the small elements at the tool tip can penetrate into the enlarged elements of the workpiece in contact with the tool tip, affecting the remeshing process and the results. Moreover, a fine mesh near the workpiece surface allows to extract the profile of residual stresses in the workpiece accurately.

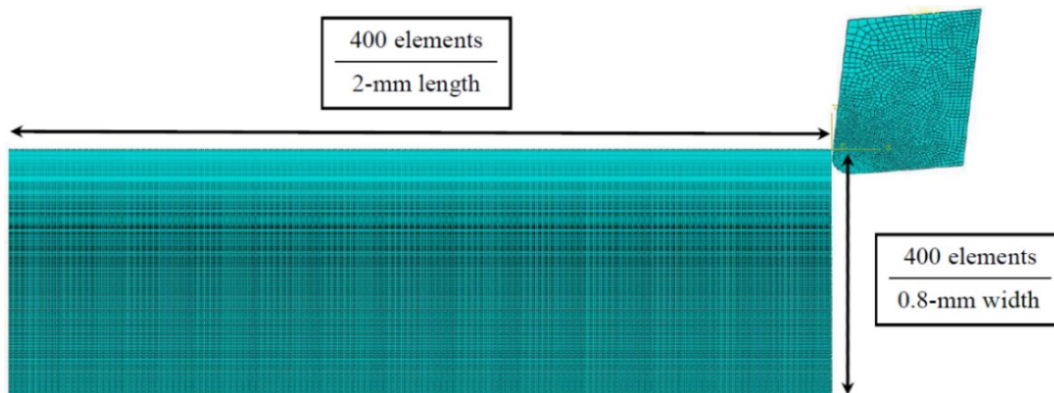


**Fig. 3-7.** Arrangement of elements along the length and width of a rectangular workpiece.

### 3.6.2. Adaptive meshing

Increasing the remeshing and sweep times (increasing the intensity of remeshing process) has a number of benefits and drawbacks as follows:

- It prevents the elements from excessive distortion.
- It provides a better quality of mesh around the tool tip.
- It augments the calculations and run time of the program.
- It increases errors due to the mesh and advection sweeps.

Thus, the magnitudes of remeshing parameters should be optimized to reach an accurate, computationally efficient solution.

Adaptive Meshing consists of two fundamental tasks: Remeshing and Remapping techniques. Creating a new mesh is called Remeshing in general or Mesh Sweep in Abaqus software in order to improve the mesh quality to avoid excessive distortion of elements. Remeshing in Abaqus is a semi-automatic process, in which two key parameters described below are determined by the user:

- ‘Frequency’: indicates how often remeshing is performed, whatever the mesh quality is.
- ‘Remeshing sweeps per increment’: denotes how many times mesh sweep is performed per adaptive mesh increment.

For instance, ‘Frequency=10’ and ‘Remeshing sweeps per increment=4’ represent that remeshing is performed every 10 increments and 4 mesh sweeps are performed every adaptive remeshing increment.

Two main types of Remeshing are commonly utilized:

1. r-adaptively or smoothing, which includes relocating of the nodes to provide better element shapes without altering the topology (elements and connectivity) of the mesh (Fig. 3-8b).

2. h-adaptively or refinement, which includes increasing the number of elements (reducing the size of elements), which leads to changing the topology of the mesh (Fig. 3-8c).

Abaqus uses r-adaptively scheme to perform remeshing process.

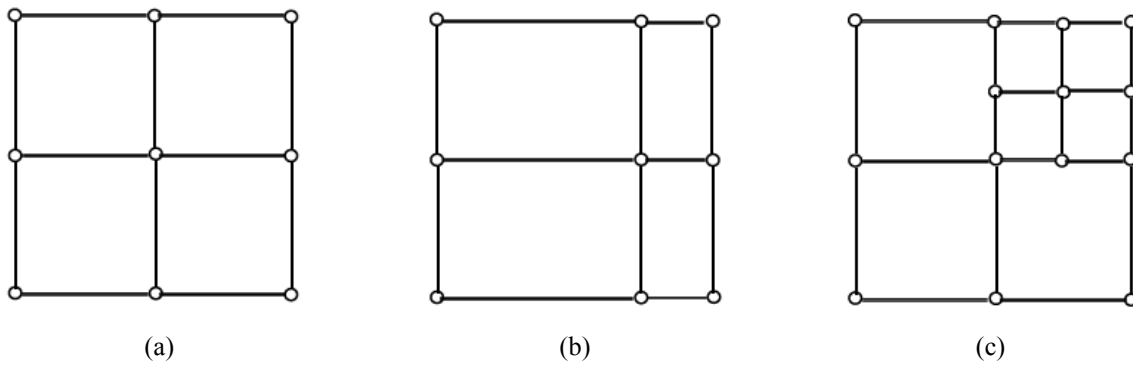


**Fig. 3-8.** Remeshing schemes:

(a) original mesh, (b) r-adaptively: relocating the nodes, and (c) h-adaptively: reducing the size of elements.

Mapping the field variables from the old mesh to a new one is called Remapping/Rezoning in general or Advection Sweep in Abaqus FE program. Remapping in Abaqus is a fully automatic process in which the number of advection sweeps is determined automatically by the software. Ideally, only one advection sweep is performed after all the mesh sweeps for the increment are conducted (the specified number of mesh sweeps is reached). Another advection sweep is performed if the total accumulated displacement of any node in the domain is greater than 50% of the characteristic length of any adjacent element [141].

In the present study, 'Frequency' and 'Remeshing sweeps per increment' parameters are tuned in turn as 5 and 5 for the remeshing process.

### 3.6.3. Mass Scaling

Mass scaling is utilized to augment the length of time increment by adding non-physical mass to the system and consequently reduce the run time of the simulation. Mass scaling must be used with care to ensure that the inertial forces do not dominate and change the solution. The inertial effects are negligible if:

- i. the ratio of the kinetic energy to the internal energy is less than 10%, or
- ii. the results of the analyses for a few cases with and without mass scaling are approximately the same.

In the present research, mass scaling factor of 400 is applied to the whole model at the beginning of the cutting step. The kinetic energy was continuously monitored and was always less than 1% of the total energy during the simulation, ensuring that the applied mass scaling did not affect the predicted state variables.

It should be noted that mass scaling affects  $\Delta t_{M-cr}$  by changing the density of the minimum-size element in the workpiece. In contrast, mass scaling does not affect  $\Delta t_{T-cr}$  as the term of ‘density times specific heat capacity’ is independent of the mass of the element (Eq. (3-13)).

The modeling of cutting and residual stress steps takes in turn about 7 and 67 hours using a computer system of Intel® Core™ i7-2600 CPU with a speed of 3.4 GHz and a memory RAM of 16.0 GB.

## **CHAPTER 4    Experimental Tests**

### **4.1. Introduction**

The machining forces and residual stresses predicted by finite element method need to be validated experimentally in order to be used confidently for subsequent design optimization studies. Machining forces are often measured using a piezoelectric dynamometer during cutting. Among the methods for measuring residual stresses including the X-Ray diffraction, hole drilling, electro-magnetic, and ultrasonic methods, the X-Ray diffraction method is commonly utilized due to being non-destructive, requiring minimal sample preparation, and having higher accuracy.

In this chapter, the experimental tests carried out in the present study, the principles of residual stress measurements, and two different XRD machines are described.

### **4.2. Machining and cutting force measurements**

The work material is a rod bar with 60 mm diameter and 150 mm length made of 300M steel. 300M steel is a high strength low-alloy steel, which has high strength with desirable ductility. Hard radial turning tests are conducted on a Mazak CNC lathe (Fig. 4-1) using a round-edge ceramic inserts (ISO TPGN 160308E Grade CC650 from Sandvik) with an edge radius of 50  $\mu\text{m}$ . The insert is mounted on a right-hand tool holder CTFPR 2020K16 with a back rake angle of  $5^\circ$ . The workpiece is disc-shape, of 47 mm external diameter and 4.5 mm thickness, machined directly on the stock bar. Cutting and thrust forces are measured using a Kistler (type 9121) three-component piezoelectric dynamometer. The acquisition of force signals is conducted with an in-house

LabView code and data treatment is performed using a MATLAB code. The directions of the cutting and thrust forces are displayed in the experimental set-up and also in the corresponding FE model in Fig. 4-2. The chip thickness is measured using a digital micrometer by averaging the values of the chip thickness at three different locations far enough from the two ends. The cutting edge radius was measured using a LEXT OLYMPUS (OLS 4100) laser microscope.



Fig. 4-1. Mazak CNC lathe used for machining of samples.

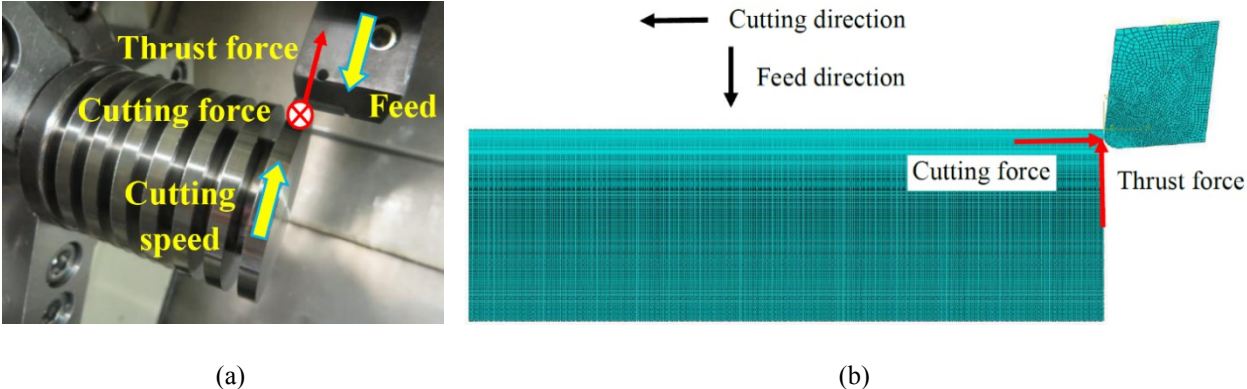
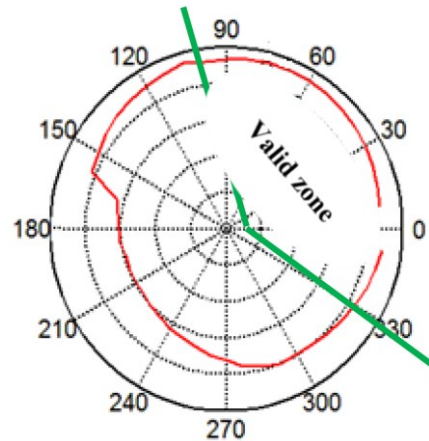


Fig. 4-2. Directions of cutting and thrust forces in (a) the experiment and (b) the FE model.

During radial turning process, the final machined surface is not homogeneous from cutting conditions point of view due to the tool's stop and retraction times at the end of the cutting process. Therefore, before measuring the residual stresses, circularity profile measurements are conducted using a Mitutoyo Coordinate Measuring Machine (CMM) in order to locate the machining zone that is a representative of the actual cutting conditions over the workpiece's circumference [142], as shown in Fig. 4-3.



(a)



(b)

**Fig. 4-3.** (a) Measurement of circularity profile of the specimen using a coordinate measuring machine and (b) the circularity profile and valid zone required for residual stress measurements.

### 4.3. Residual stress measurements

#### 4.3.1. Principles of X-Ray Diffraction Method

X-Ray Diffraction is a versatile, non-destructive method used to measure residual stresses remain in crystalline materials using the distance between crystal planes (lattice spacing or d-spacing) as a strain gage. X-Rays, whose wavelengths are generally on the order of lattice spacing in crystalline materials (about  $10^{-9}$  to  $10^{-10}$  m), can be diffracted from these materials. When the electromagnetic X-Ray waves hit the specimen, the waves scattered by the atoms inside the specimen can interfere destructively or constructively. In the destructive interference, one wave is at maximum amplitude while the other is at minimum amplitude, where the waves are said to be out of phase (Fig. 4-4a). Destructive interference occurs most often, but in specific directions constructive interference takes place. In the constructive interference, the waves travel in the same step as each other, reinforcing one another and are said to be in phase (Fig. 4-4b). This phenomenon, in which the scattered X-Rays are intensified, is called X-Ray Diffraction.

The spacing  $d$  between atomic planes in the specimen material is measured using Bragg's law, which says the difference in the path length between incident and diffracted beams must be an integer multiple of wavelength, as shown in Fig. 4-5. Consequently, Bragg's formula can be obtained as:

$$AB + BC = n\lambda \quad (4-1)$$

which leads to:

$$2d \sin \theta = n\lambda \quad (4-2)$$

where  $n$  is an integer denoting the order of diffraction,  $\lambda$  is the wavelength of the X-Ray beam,  $d$  is the lattice spacing of crystal planes, and  $\theta$  is the diffraction angle. Note that since X-Rays 1

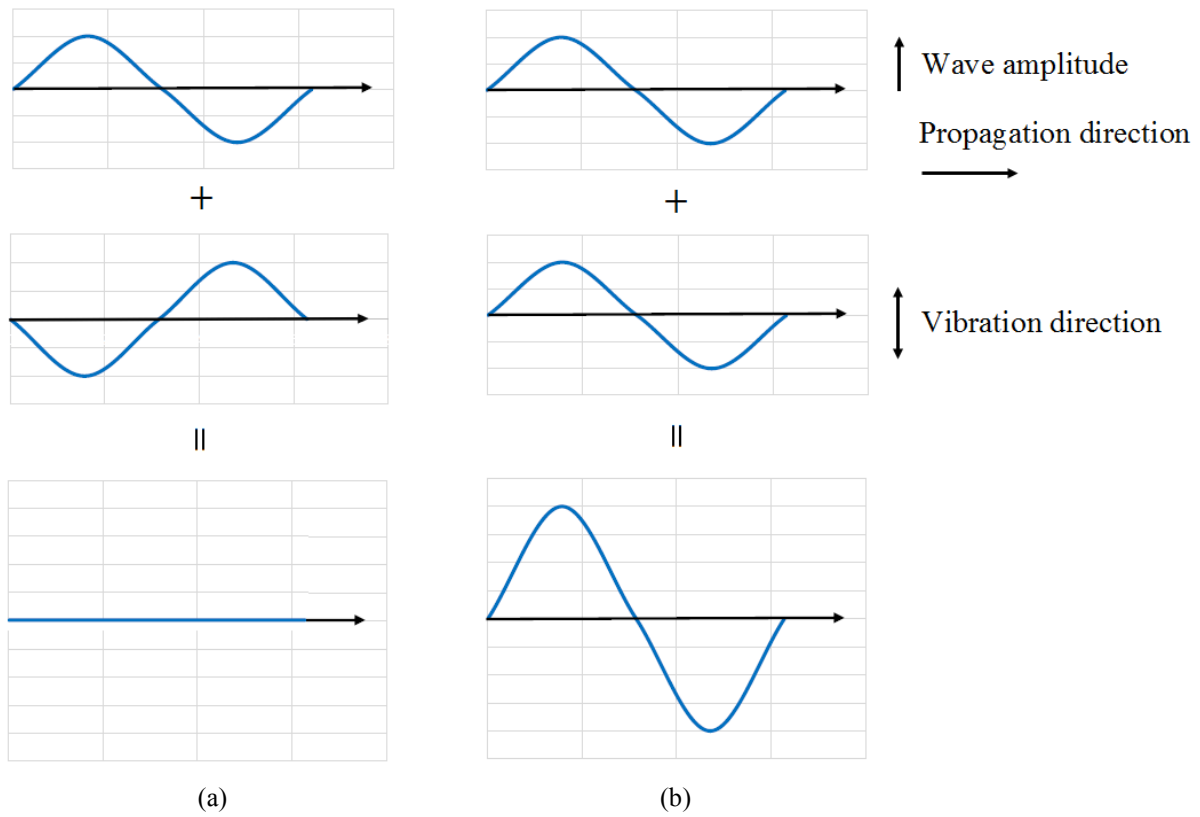


Fig. 4-4. X-Ray waves: (a) Destructive interference and (b) Constructive interference.

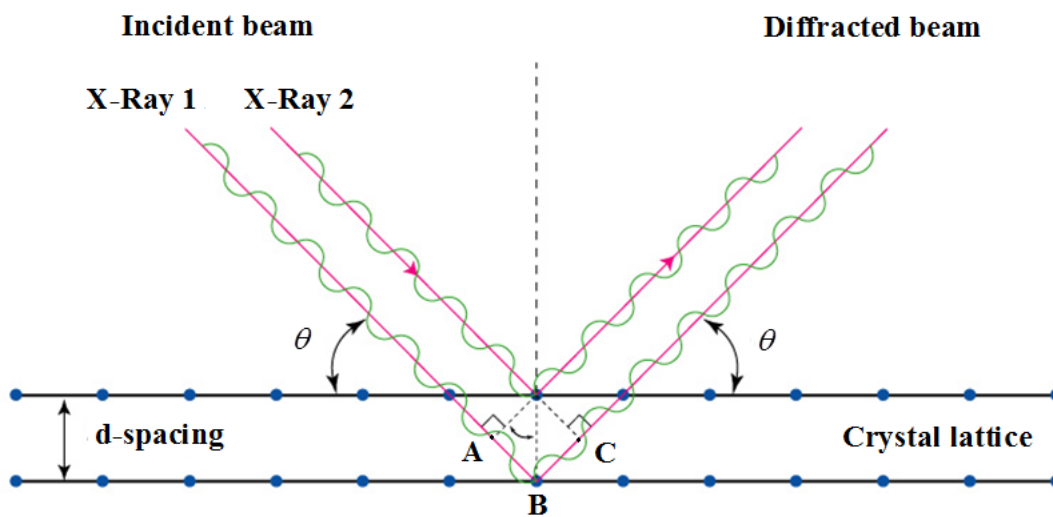


Fig. 4-5. Bragg's law [143].

and  $2$  come from a far distance (compared with interplanar spacing), it is assumed that they are parallel. The strains can be obtained based on the change in spacing  $d$  and the stresses can be calculated from the strain values using Hooke's law.

Any change in the lattice spacing  $d$  leads to a corresponding shift of a few increments of degree in the diffraction angle  $2\theta$ . This can be shown by differentiating the Bragg's formula:

$$\frac{\Delta d}{d} = -\Delta \theta \cot \theta \quad (4-3)$$

where  $\Delta d = d - d_0$  and  $\Delta \theta = \theta - \theta_0$ , where  $d_0$  and  $\theta_0$  are the lattice spacing and diffraction angle of the stress-free material. Eq. (4-3) in terms of  $\Delta 2\theta$  becomes:

$$\frac{\Delta d}{d} = -\frac{\Delta 2\theta}{2} \cot \theta \quad (4-4)$$

where  $\Delta 2\theta = 2\Delta \theta$ .

The elastic strains are measured using X-Ray diffraction method because only these strains change the mean lattice spacing [144]. The inelastic strains lead to dislocation motion and formation of micro-stresses which exist only locally, i.e. either between grains or inside grains. Also, these strains do not increase macroscopic stresses, the stresses created over large regions containing many grains within a material. As a result, although residual stresses are formed due to non-uniform plastic deformation, all macro residual stresses remaining after deformation are elastic [144].

Residual stresses should be measured in round (cylindrical) components such that the X-Ray beams effectively 'see' a flat area [145] so that the angle between the normal to the irradiated (spot) area and the normal to the lattice planes should be constant during measurements [144]. As a result, measurement of residual stress requires a maximum spot size of  $R/4$  and  $R/2$  in turn for the hoop

and axial directions, where R is the radius of the curvature of the component [145]. In the present work, the spot (pocket) area is 2.5 mm × 2.5 mm, which is within the standard range of a spot size for cylindrical components.

#### ***4.3.2. Pulstec and Proto machines for residual stress measurements***

There are two types of machines collecting X-Ray diffracted patterns using two different methods to measure residual stresses [146]. The first machine is Pulstec  $\mu$ -X360n machine which first collects the full diffracted cone (Debye-Scherrer ring) using a two-dimensional highly sensitive detector for a single incident angle of X-Rays (Fig. 4-6a) and then calculates residual stresses based on Cos  $\alpha$  method. The second machine is Proto iXRD machine that captures the diffracted beams on two opposite sides of the diffracted cone through two X-Ray detectors for a number of incident angles of X-Rays (Fig. 4-6b) and then computes residual stresses using Sin<sup>2</sup> $\Psi$  method. The residual stress calculation based on Cos  $\alpha$  method and Sin<sup>2</sup> $\Psi$  method is presented in Refs. [147] and [144], respectively. The time required for measuring each point is about 2 and 10 minutes using Pulstec and Proto machines, respectively, showing that the residual stress measurement using Pulstec machine is much faster than that using Proto machine with almost the same accuracy. This is because the Pulstec machine uses a single exposure of X-Ray beams on the component, while the Proto machine needs multiple exposures (7 to 11 exposures for standard measurements) and subsequent diffracted X-Ray detection at each angle [148].

In the present research, the residual stresses are measured using Pulstec  $\mu$ -X360n machine due to the above-mentioned advantage. The X-Ray diffraction constants and parameters are also listed in Table 4-1.

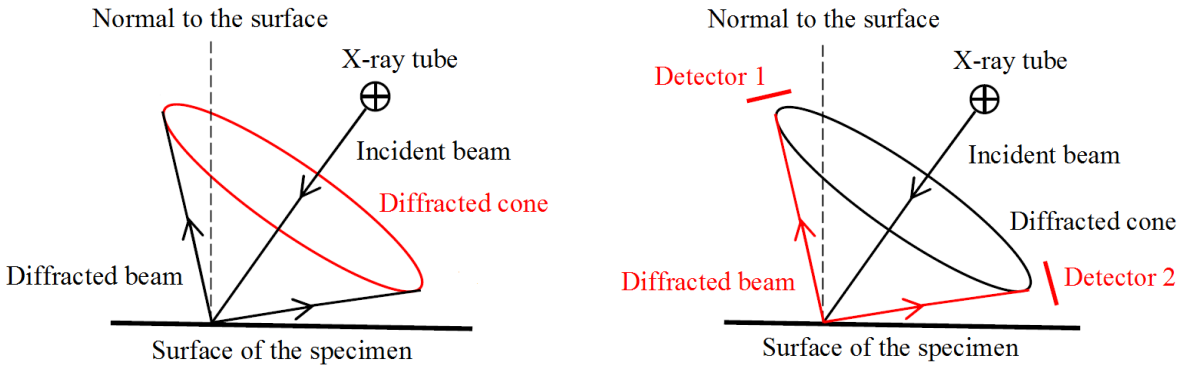
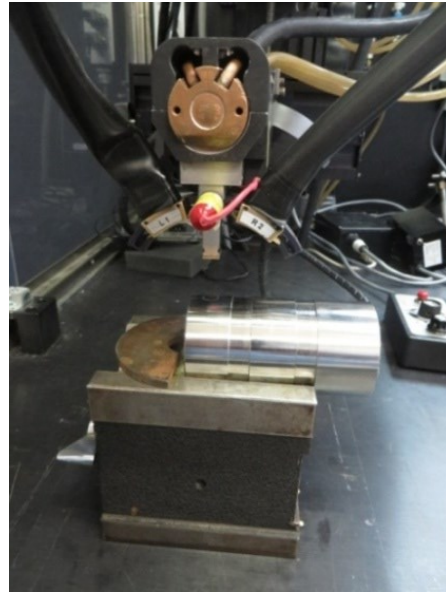
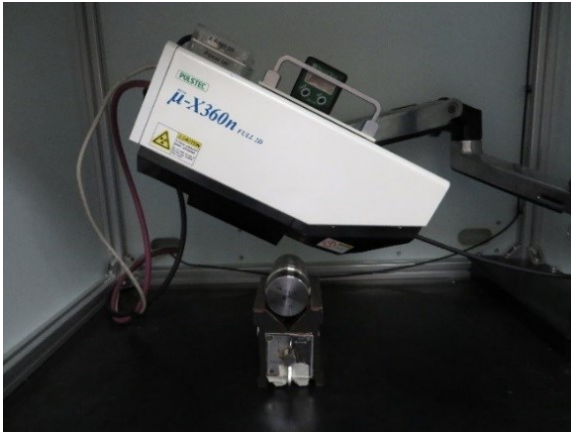


Fig. 4-6. (a) Pulstec  $\mu$ -X360n equipment versus (b) Proto iXRD apparatus.

Table 4-1

Constants and parameters for residual stress measurements using a Pulstec machine

Material	300M Steel (bcc)	Voltage	30 kV
hkl plane	{211}	Current	1 mA
Bragg angle	156.41°	X-Ray incidence angle	35°
Tube	Cr_K $\alpha$	X-Ray irradiation time	30 s
Wavelength	0.2291 nm	Aperture	1 mm

#### **4.4. Electropolishing method**

In order to measure subsurface residual stresses, access to the depth below the workpiece's surface should be provided. Mechanical methods of polishing should be avoided as they will induce additional residual stresses into the component and change the residual stress profile [145]. Electropolishing (electrochemical polishing or electrolytic polishing) is an electrochemical finishing technique that removes material from the surface of a metallic workpiece on the order of micrometer without applying new stresses. When electropolishing is carried out in a large scale, the workpiece is submerged in a bath of electrolyte solution and acts as the anode. This peripheral polishing is a very slow technique. In contrast, on a small (laboratory) scale, which is a fast polishing process and is thus employed in the present research work, the electrolyte is pumped onto a very small part of the workpiece's surface limited with a small mold which builds a local bath (Fig. 4-7). The positive (+) side of a DC power supply is connected to the anode and the negative (-) one is attached to the cathode. A metal plate plays the role of the cathode. A voltage (60 kV) is then applied for a set time which is determined based on the required removal depth. When current is applied, the electrolyte acts as a conductor and allows the current to flow from the anode to the cathode. As a result, the workpiece surface is oxidized and dissolved in the electrolyte solution. Consequently, metal ions are removed from the workpiece and move into the cathode according to Faraday's first law, which expresses that the mass of the removed metal is proportional to the applied current and the exposure time [145]. In addition, the efficiency of the electrolyte solution should also be considered.

In the present study, in-depth residual stress measurements are carried out by removing material using Proto electropolishing machine as illustrated in Fig. 4-7.

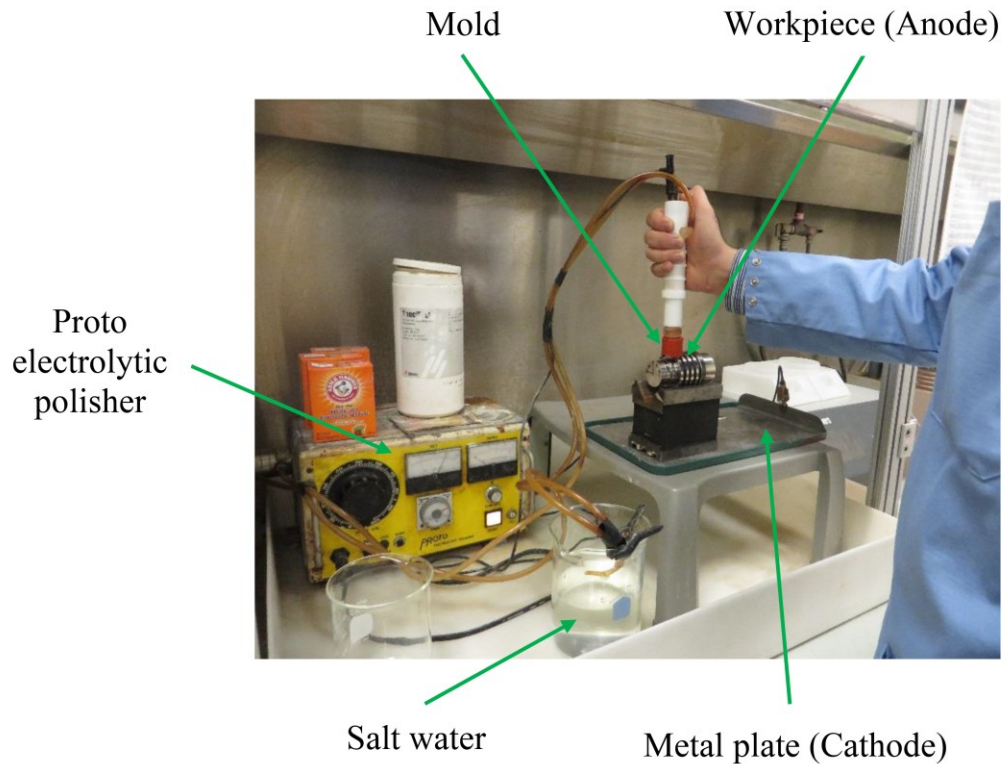


**Fig. 4-7.** Electropolishing process.

#### **4.5. P-profile measurements**

The depth of the removed material should be measured each time the electroplating is done. This process is called P-profile measurement. The depth can be measured using contact or non-contact type instruments. In the contact-type instrument such as profilometer (also called perthometer), the stylus' tip directly touches the sample surface and registers the vertical positions of the points on the sample surface as it travels along the pocket center line. The stylus moves closely on the sample surface, and as a result, the produced profile is highly reliable [149]. In non-contact type machine such as Laser microscope, light is emitted from and reflected back to, the

instrument to measure the depth without touching the sample. This machine never scratches the sample, and consequently, can be used for P-profile measurements in soft materials [149].

In the present research study, a profilometer is used as it provides not only a faster measurement but is also less expensive, compared with a laser microscope. In addition, 300M steel is a very hard material (55 HRC). A measurement using a Mitutoyo SJ-400 profilometer is shown in Fig. 4-8.



**Fig. 4-8.** P-profile measurement.

## **CHAPTER 5    Regression Analysis and Optimization Strategy**

### **5.1. Introduction**

Performing optimization algorithm on the full finite element model of the cutting and stress relaxation processes is computationally very expensive and impractical. This is basically due to the fact that at each optimization iteration, the FE model may be called several times. Due to the coupled thermo-mechanical dynamic and highly nonlinear nature of machining processes, each FE run by itself demands high computational time. Considering above, in this research study, Design of Experiment (DoE) combined with Response Surface Method (RSM) have been utilized to generate smooth response functions which can explicitly relate the desired response variables including cutting temperature, cutting and thrust forces, and surface residual stresses to the identified cutting process and tool geometry parameters. This assists to effectively conduct design optimization problems without executing the FE model during the optimization process.

In this chapter, design of experiment, response surface method, and optimization methods and proposed strategy implemented in this research are explained. Then, the solution procedure to improve response variables in terms of machining parameters is illustrated.

### **5.2. D-optimal Design of Experiment**

Design of Experiment is a statistical technique to maximize the information gain while a minimum number of expensive and/or time-consuming experiments is conducted. DoE can be divided into two main groups: physical and computer experiments. Full or fractional factorial

designs, Box-Behnken design, and Central Composite Design (CCD) are a number of physical (also called classical) DoEs, which include some stochastic noise. In contrast, Point Exchange, D-optimal, and IV-optimal are some of computer-based DoEs, which lack any noise as repeated computer experiments (simulations) with the same inputs always lead to identical outputs [150]. Among the computer-based DoEs, a D-Optimal design, which tries to maximize the determinant of the information matrix of the design  $\left( X^T X \right)$ , is the most well-known, commonly used optimality criterion, where  $X$  is the  $n \times m$  design matrix in which  $n$  is the number of undertaken experiments and  $m$  is the number of unknown model coefficients  $\beta$ .

### 5.3. Response surface method

Response surface method (RSM) is a combination of mathematical and statistical techniques utilized to build response functions fitting to the data. RSM is based on regression analysis to find a suitable approximation, often polynomial functions, to the true relationship between the output quantities and input variables. For instance, a polynomial model can be written as:

$$\hat{y} = X\beta \tag{5-1}$$

where  $\hat{y}$  is the approximation of the true response  $y$  that may be given as:

$$y = \hat{y} + \varepsilon \tag{5-2}$$

in which  $\varepsilon = y - \hat{y}$  is the error between the true response  $y$  and its approximation  $\hat{y}$ . The best approximate model is the one with minimum error  $\varepsilon$ . The problem is then to find the unknown coefficients  $\beta$  that minimize  $\varepsilon$ , which can be achieved using the Least Square Technique.

In this research, a complete quadratic model with five design variables and 21 terms has been utilized as (the number of terms equals  $(5+1)(5+2)/2$ ):

$$\begin{aligned} \hat{y} = & a_0 + a_1 V + a_2 f + a_3 r_\beta + a_4 \gamma_0 + a_5 \alpha_0 + a_6 Vf + a_7 Vr_\beta + a_8 V\gamma_0 + \\ & a_9 V\alpha_0 + a_{10} fr_\beta + a_{11} f\gamma_0 + a_{12} f\alpha_0 + a_{13} r_\beta\gamma_0 + a_{14} r_\beta\alpha_0 + a_{15} \gamma_0\alpha_0 + \\ & a_{16} V^2 + a_{17} f^2 + a_{18} r_\beta^2 + a_{19} \gamma_0^2 + a_{20} \alpha_0^2 \end{aligned} \quad (5-3)$$

where  $a_0$  to  $a_{20}$  are unknown coefficients (elements of  $\beta$ ). This model is the most complete type of quadratic models which includes all constant, linear, interaction, and squared terms. In the present research,  $\hat{y}$  can be superficial residual stress  $\sigma_{surf}$ , cutting temperature  $T$ , cutting force  $F_c$ , and thrust force  $F_t$ , and also design variable  $V$  (or  $x_1$ ) is cutting velocity,  $f$  ( $x_2$ ) feed rate,  $r_\beta$  ( $x_3$ ) edge radius,  $\gamma_0$  ( $x_4$ ) rake angle, and  $\alpha_0$  ( $x_5$ ) clearance angle.

It is important to verify the accuracy of the developed quadratic model in order to use with confidence in the design optimization process. To accomplish this, the coefficient of determination known as  $R^2$  is calculated as:

$$R^2 = 1 - \frac{SSE}{SST} \quad (5-4)$$

in which  $SSE = \sum_{i=1}^n (y_i - \hat{y}_i)^2$  and  $SST = \sum_{i=1}^n (y_i - \bar{y})^2$ , where  $y_i$  is the true output response, here calculated from the FE analysis,  $\hat{y}_i$  is the approximate response computed from RSM,  $\bar{y}$  is the average of the true response, and  $n$  is the number of design points used to generate the model.  $R^2$  varies between 0 and 1, where the more the value of  $R^2$  is close to 1, the more accurate the approximate response function  $\hat{y}$  is modeled by RSM.

#### 5.4. Genetic Algorithm

Genetic Algorithm (GA) is a stochastic search optimization method suitable for solving a variety of optimization problems in which the objective function is discontinuous, nondifferentiable, or highly nonlinear. GA is based on natural selection and biological evolution, which differs from classical, derivative-based optimization algorithms. The following procedure briefly shows how GA works [151]:

- 1- The algorithm commences by creating a random initial population. Each population is an array of individuals (an individual is also called a chromosome or genome or string). Each individual is a vector whose elements are named genes. Note that genes are design variables in the optimization process.
- 2- The algorithm creates a sequence of new populations. At each generation, GA selects certain individuals having better fitness values in the present population. These individual are called parents, by which individuals for the next population, called children, are produced. Three types of children using three genetic operators can be produced:
  - (a) Elite children: Some of the individuals with higher fitness in the current generation are chosen as elite children, which automatically survive to the next population. This operation is termed Reproduction.
  - (b) Crossover children: The genes of a pair of parents are exchanged to create crossover children. This operation is known as Crossover, which is usually applied with a high probability.

(c) Mutation children: Random changes to the genes of a single parent are applied to produce mutation children. This operation is called Mutation, applied with a low probability. Mutation operator prevents GA from being trapped in local extrema.

The algorithm replaces the present population with the children to form the new population.

3- The algorithm stops when one of the stopping criteria is met.

In addition, some important terminology of GA are presented below:

- Population size: specifies how many individuals exist in each generation.
- Elite count: specifies the number of elite children.
- Crossover fraction: specifies the fraction of the next population, except elite individuals, that are generated by Crossover. The remaining individuals in the next population are produced by Mutation.
- Function tolerance: If the cumulative change in the fitness function is less than ‘function tolerance’, the algorithm stops.

### **5.5. Sequential Quadratic Programming Method**

Sequential Quadratic Programming (SQP) is a gradient-based, iterative method suitable for nonlinear optimization problems. In the SQP algorithm, a Quadratic Programming (QP) subproblem is derived to be solved at each optimization iteration. It should be noted that the QP problem has a quadratic cost (fitness) function and linear constraints which represents a convex problem. At each iteration, the approximation of the Hessian of the objective or Lagrangian functions, in turn for unconstrained or constrained optimization problems, is updated using a quasi-

Newton methods such as modified Broyden-Fletcher-Goldfarb-Shanno (BFGS) technique to find the search direction (the descent or downhill direction). The standard BFGS formula is modified to tackle the problem of a singular or indefinite Hessian which arises when the standard BFGS Hessian updating is utilized [152]. The gradients of the objective or Lagrangian functions and the step size (the descent step) can be computed at each iteration using numerical methods such as central difference method and Golden Section Search (GSS) method, respectively. By solving a sequence of QP problems in an iterative process, the solution is converged and the optimum point is found. An overview of SQP can be found in Fletcher [153] and Gill et al. [154]. It needs mentioning that although the derivative-based techniques including SQP are powerful, they have some drawbacks such as getting stuck in local extremum.

## **5.6. Optimization strategy**

Among optimization methods, Genetic Algorithms are stochastic-based optimization tools capable of determining global or near-global optimum solutions. An overview of the literature reveals that GA was widely utilized for optimizations of machining process parameters [103]. However, since GA searches the design space based on random number generation using natural selection, there is no absolute guarantee for GA to obtain accurate global point [152]. On the other hand, sequential quadratic programming is a powerful gradient-based mathematical programming method capable of accurately catching the local optimum point around the given initial point. As a result, if SQP is provided with an initial point given by GA, it is guaranteed that the local optimum point obtained by SQP is the true global optimum point. An illustrative example is displayed in Fig. 5-1(a) to show how this strategy works. The curve in this figure shows the values

of the objective function ( $F$ ), the minimum of which is sought, against the vector of design variables ( $X$ ). When GA is run, it returns one of the points on the curve inside the rectangle such as Point I as the optimal solution, which is not necessarily the global optimal. In contrast, when an initial point such as the small green circle is given to SQP, it returns the nearest local optimum point, i.e. the small blue circle. Accordingly, when a combination of GA and SQP is used as displayed in Fig. 5-1(b), the true global optimum point, i.e. the small red circle is obtained.

### **5.7. Solution procedure**

As mentioned previously, to avoid performing simulation and optimization runs at the same time, which is computationally very expensive, DoE and RSM are utilized initially to relate input parameters including cutting conditions and tool geometry to output quantities namely cutting temperature, machining forces, and residual stresses obtained by the FE model. The developed response meta models are smooth polynomial functions which explicitly relate the desired outputs to the design inputs and thus can effectively be used as the objective and constraint functions in the hybrid GA-SQP method described in the previous section to capture the global optimum point accurately. The flowchart of solution procedure is shown in Fig. 5-2.

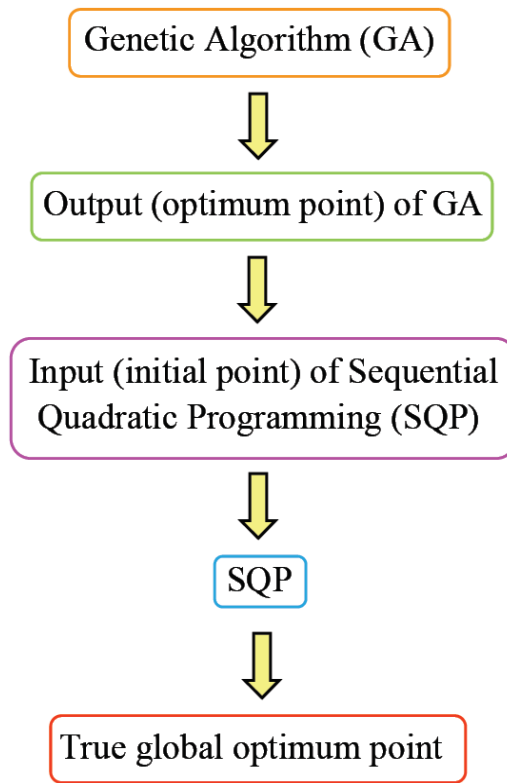
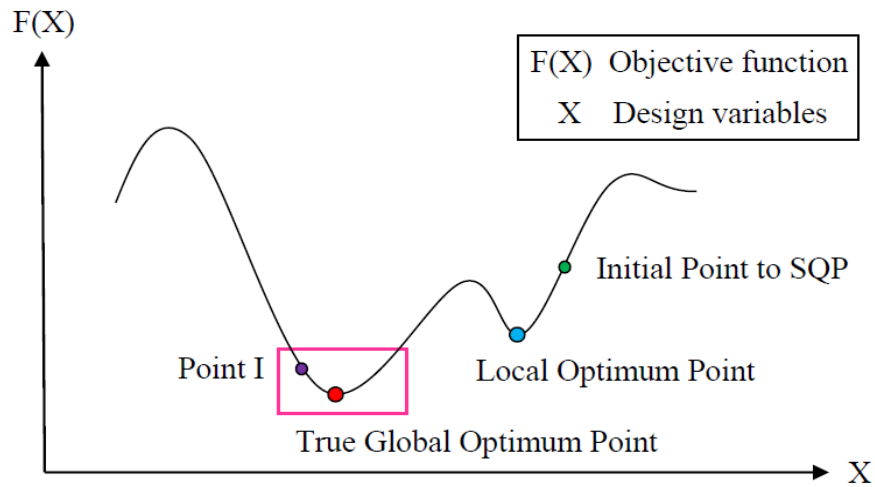


**Fig. 5-1.** Optimization problem strategy: (a) an illustrative example and (b) a flowchart of the GA-SQP method.

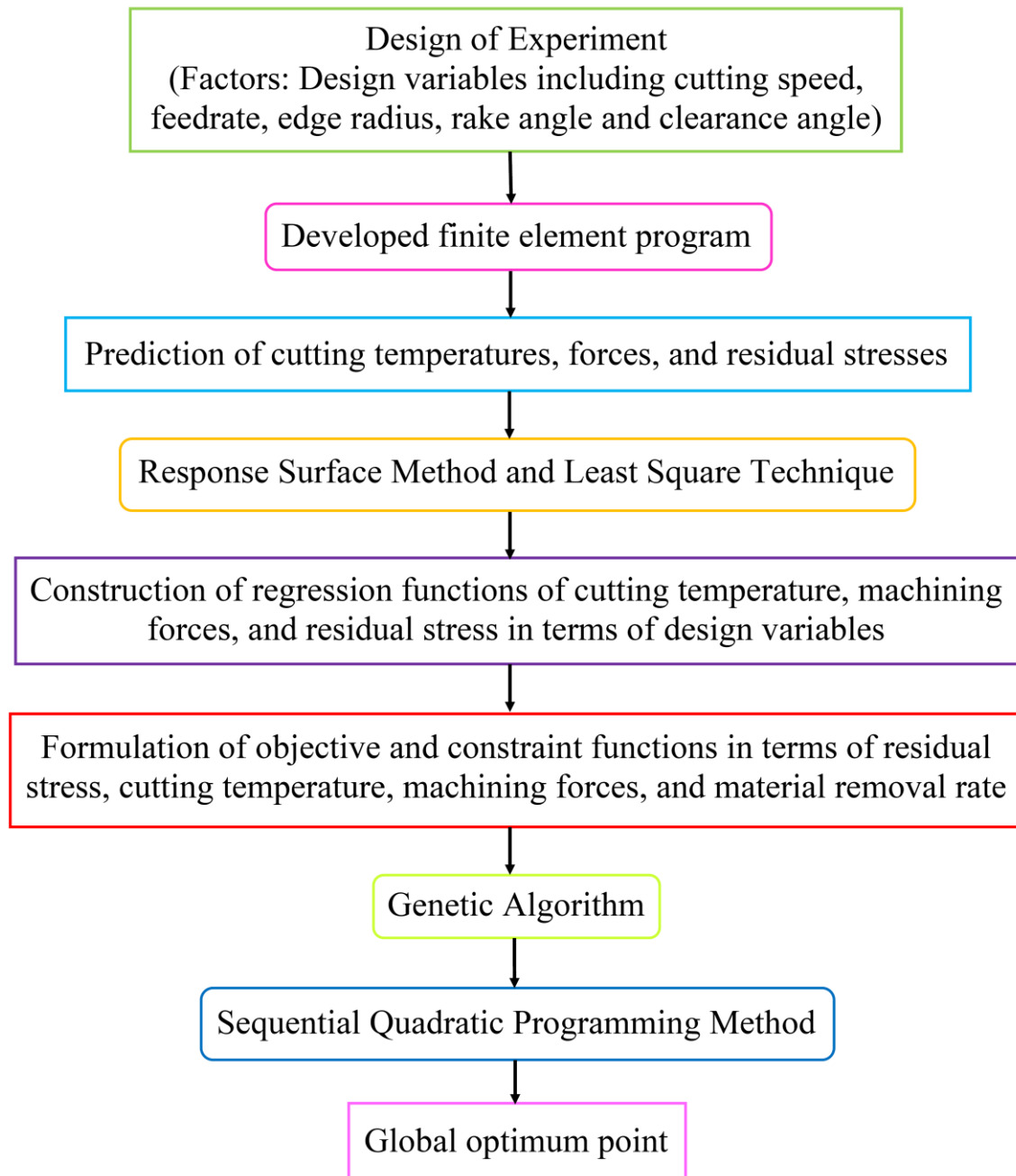


**Fig. 5-2.** The flowchart showing the solution procedure.

## **CHAPTER 6 Discussion of Results**

### **6.1. Introduction**

In this chapter, the developed finite element model is validated by comparison of the simulation results with those obtained using experimental tests. This is then followed by formulating multi-performance optimization problems. Finally, the results of constrained and unconstrained optimization problems are presented and discussed.

### **6.2. Validation of the finite element model**

The developed finite element model is validated using the experimental results of chip thickness, cutting and thrust forces, and residual stresses, as presented in Table 6-1. These experimental results are obtained during radial hard turning under cutting conditions listed in Table 6-2. Table 6-3 provides the mechanical and thermal properties of cutting tool and work materials and Table 6-4 contains the Johnson-Cook constants of 300M steel used in simulations. The results show that the measured and predicted cutting forces and chip thicknesses are in good agreement, whereas there exists small discrepancy between experimental and predicted thrust forces. Previous research [72,84] have demonstrated that there is a general trend to systematically underestimate the thrust force when using FEM for machining simulations, as discussed in more details in Chapter 2.

**Table 6-1**Comparison of average cutting force  $F_c$ , thrust force  $F_t$ , and chip thickness  $t_c$ 

	$F_c$ [N / mm ]	$F_t$ [N / mm ]	$t_c$ [mm ]
Experiment	281	323	0.151
Prediction	284	243	0.137

**Table 6-2**

Cutting conditions and tool geometry

Cutting speed	Feed rate	Edge radius	Rake angle	Clearance angle
$V$ [m / min]	$f$ [mm / rev ]	$r_\beta$ [mm ]	$\gamma_0$ [deg]	$\alpha_0$ [deg]
64	0.07874	0.050	5	6

**Table 6-3**

Mechanical and thermal properties of the workpiece and tool

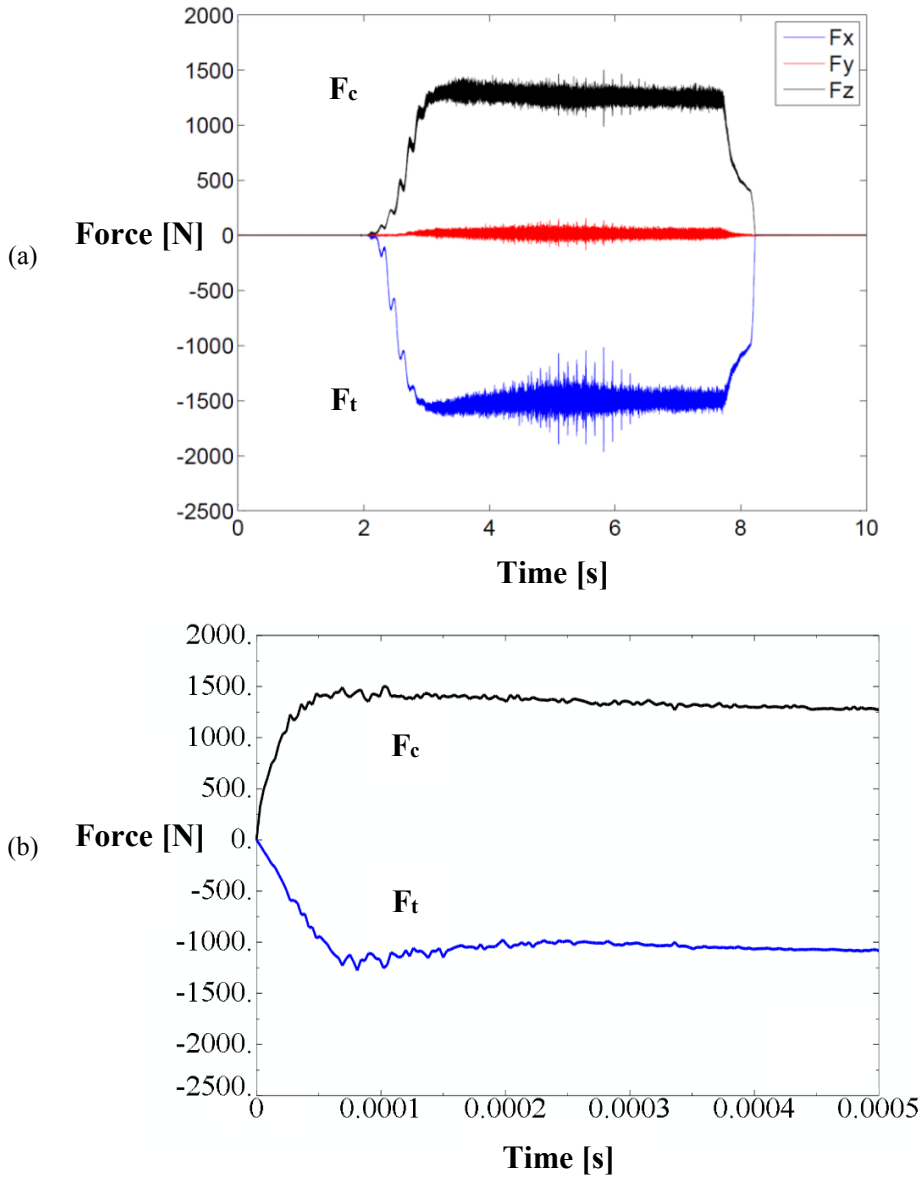
Property	300M Steel [155,156]	Ceramics (CC650) [82,157]
Density $\rho$ [kg / m <sup>3</sup> ]	7833	4270
Young's modulus $E$ [GPa ]	205	420 (Rigid)
Poisson's ratio $\nu$	0.28	0.21
Thermal conductivity $k$ [W / (m °C)]	37.56	18
Specific heat capacity $c$ [J / (kg °C)]	448	880
Thermal expansion coefficient $\alpha$ [1 / °C]	$11.34 \times 10^{-6}$	$8 \times 10^{-6}$

**Table 6-4**

Constants of Johnson-Cook material model of 300M steel [158]

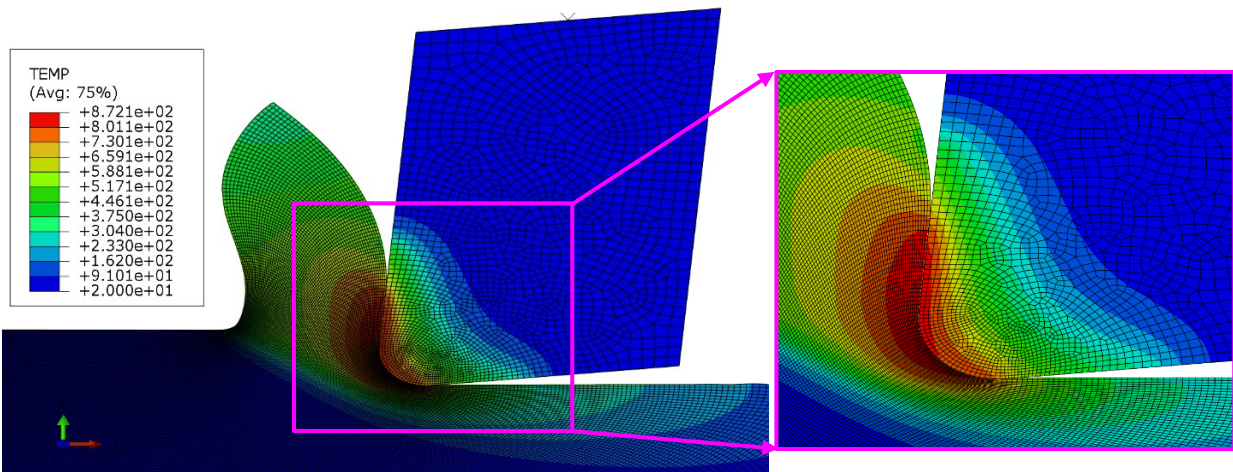
$A$ [MPa ]	$B$ [MPa ]	$n$	$C$	$m$	$\dot{\epsilon}_0$ (1 / s)	$T_m$ [°C]	$T_{room}$ [°C]
1294	1008	0.0383	0.014	1.7362	1	1421	20

Fig. 6-1 shows the variation of simulated and measured cutting and thrust forces with respect to time during the cutting process, in which the steady-state condition of machining forces is reached. The small fluctuation in the force values in the experiment is due to tool vibrations and in the simulation is due to numerical calculations including remeshing and remapping schemes.



**Fig. 6-1.** Variation of cutting and thrust forces with time during the cutting process (for 4.5-mm width of cut): (a) in experiment (Force signals) and (b) in FE modeling.

The distribution of temperature in the workpiece and tool is also illustrated in Fig. 6-2, in which the maximum temperature reaches 872 °C at the tool-chip contact face. This result is comparable with a previous work [159] on orthogonal turning of hard 4340 steel with a similar hardness to 300M steel and under similar cutting conditions including round-edge cutting tool.



**Fig. 6-2.** The distribution of cutting temperature in the workpiece and tool for the steady-state condition.

The numerical residual stress profiles are obtained by averaging the values of ten nodes at the steady-state machining region and far enough from the chip root and the start point of machining simulation. The predicted and measured circumferential residual stresses against the depth under the machined surface are shown in Fig. 6-3. As it can be seen, both predicted and experimental residual stress profiles show the same trend, where the residual stresses are highly compressive on the surface and then increase to reach small magnitudes near the bulk material. Therefore, almost good agreement exists between the simulated and measured residual stresses.

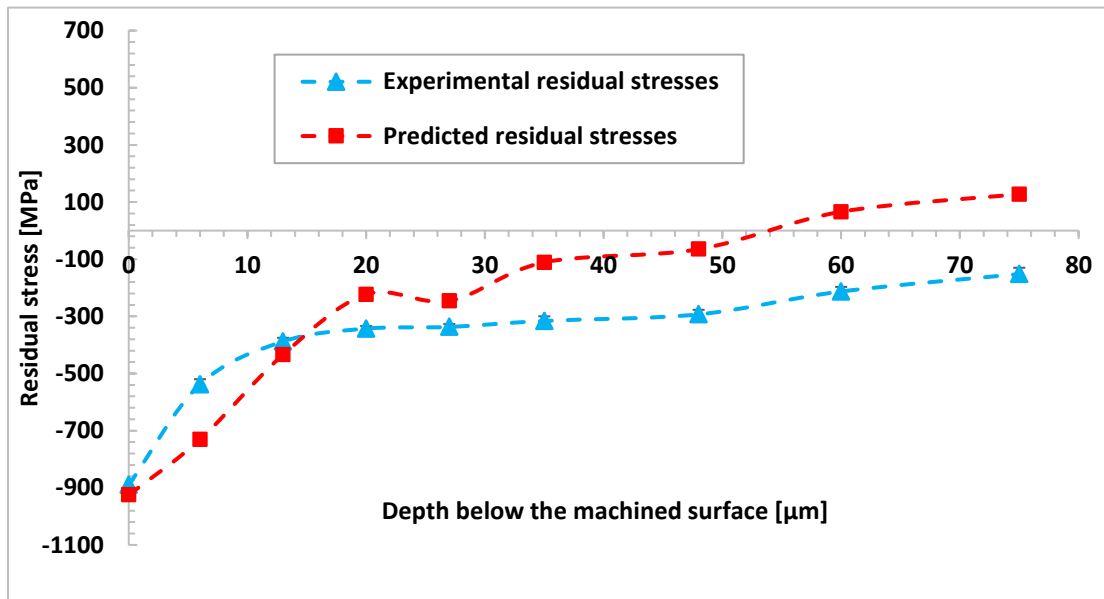


Fig. 6-3. Comparison between the predicted and experimental circumferential residual stresses.

The present simulation results show that the temperature due to cutting on the machined surface is around 450 °C, which is less than the phase transformation temperature of 300M steel, which is 725 °C. As a result, the assumption of ignoring residual stresses due to phase transformation is reasonable. The compressive character of the superficial residual stresses can be attributed to the fact that thermal conductivity of 300M steel is high ( $38 \text{ W/(m} \cdot \text{C)}$ ), and consequently, some part of the produced heat during cutting is evacuated through conduction in the workpiece to its boundaries. Therefore, the expansion due to the generated heat is small and the portion of tensile residual stress in the total stress is low, compared with compressive residual stresses stemming from machining forces (see Section 2.3.4 and Fig. 2-6). This is contrary to the materials with low thermal conductivity such as Inconel 718 ( $12 \text{ W/(m} \cdot \text{C)}$ ), in which the produced heat is entrapped

in the cutting zone, and as a result, the expansion due to heat is high. This leads to forming high tensile residual stresses after the cooling process.

The discrepancy between the finite element and experimental results can be attributed to assumptions such as considering the workpiece as a full homogeneous material, inaccuracies in input data and models including the material constitutive model and friction model, and numerical calculations such as remeshing and remapping schemes as well as round-off errors.

### 6.3. Explicit functions of response variables

The validated FE model combined with DoE and RSM can now be effectively utilized to construct approximate response functions to use in the optimization problems. To obtain the response variables including the cutting temperature, machining forces, and superficial residual stresses as explicit functions for the optimization process, first, a D-optimal design of experiment as a virtual matrix of experiments is built. The factors and levels used in D-optimal DoE are listed in Table 6-5. The machining parameters (run conditions) of the D-optimal DoE are presented in Table 6-6.

**Table 6-5**  
Factors and levels used for design of experiment

Level	Factor				
	$V$ [m / min]	$f$ [mm / rev ]	$r_p$ [mm ]	$\gamma_o$ [deg]	$\alpha_o$ [deg]
1	40	0.075	0.030	0	3
2	60	0.105	0.040	4	7
3	80	0.135	0.050	8	11
4	100	0.165	0.060	12	15

Also, the cutting temperatures, cutting force, thrust force, and superficial residual stresses predicted by finite element simulations and the calculated material removal rate for each virtual experiment are provided in Figs. 6-4 to 6-8. As observed in these figures, the cutting temperature, machining forces, and especially residual stresses change considerably with machining parameters, confirming the importance of optimization of these quantities in terms of machining parameters. It needs mentioning that continuous chip formation is assumed for all the simulations [34,36,37,40,160]. This assumption is based on the continuous chips observed in the machining experiments for FE calibration.

**Table 6-6**

Machining Parameters (MPs) using D-optimal DoE

Run No.	Machining parameters (input data)				
	$V$ [m / min]	$f$ [mm / rev]	$r_p$ [mm]	$\gamma_0$ [deg]	$\alpha_0$ [deg]
MP1	60	0.165	0.03	8	7
MP2	80	0.075	0.03	12	15
MP3	40	0.105	0.03	8	15
MP4	40	0.075	0.06	0	15
MP5	40	0.165	0.06	0	3
MP6	100	0.075	0.06	0	3
MP7	40	0.075	0.04	12	15
MP8	60	0.075	0.04	0	3
MP9	100	0.165	0.05	4	15
MP10	40	0.075	0.03	12	3
MP11	100	0.165	0.06	12	3
MP12	40	0.165	0.06	12	15
MP13	100	0.075	0.03	8	3
MP14	100	0.105	0.04	12	7
MP15	100	0.075	0.06	12	15
MP16	100	0.165	0.03	0	3
MP17	100	0.165	0.06	0	11
MP18	80	0.135	0.06	0	15
MP19	100	0.165	0.03	12	15
MP20	40	0.075	0.06	8	7
MP21	40	0.165	0.03	0	15
MP22	40	0.105	0.03	0	3
MP23	40	0.165	0.03	12	3
MP24	80	0.075	0.06	12	3
MP25	40	0.075	0.03	0	11
MP26	100	0.075	0.03	0	15
MP27	40	0.105	0.06	12	3

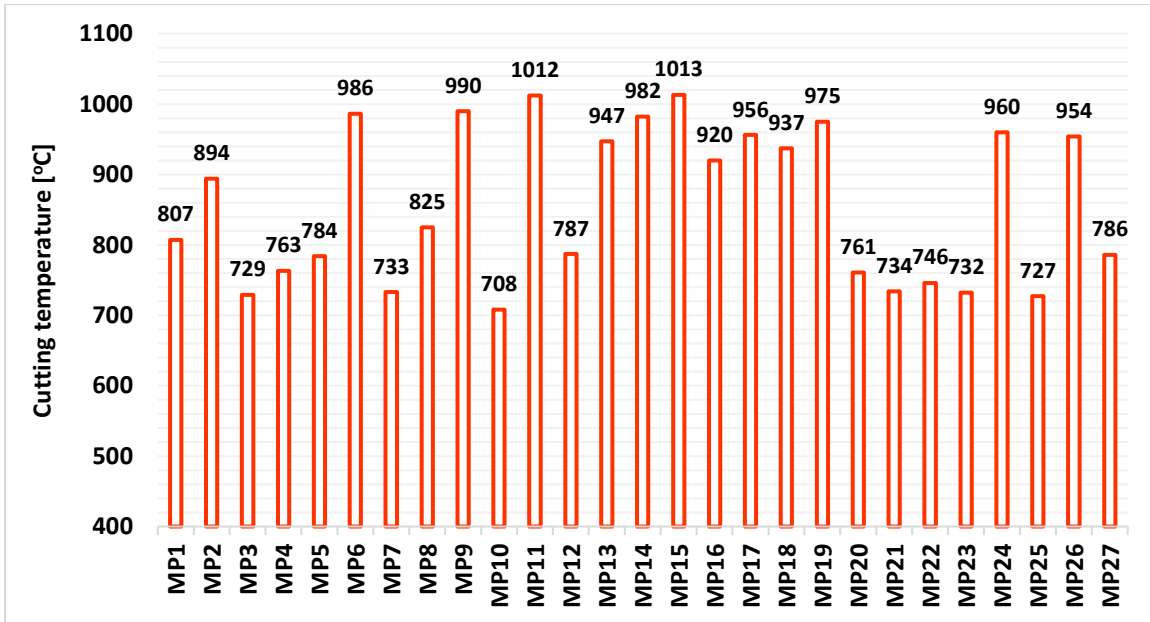


Fig. 6-4. FE predictions of cutting temperature for 27 design points in DoE.

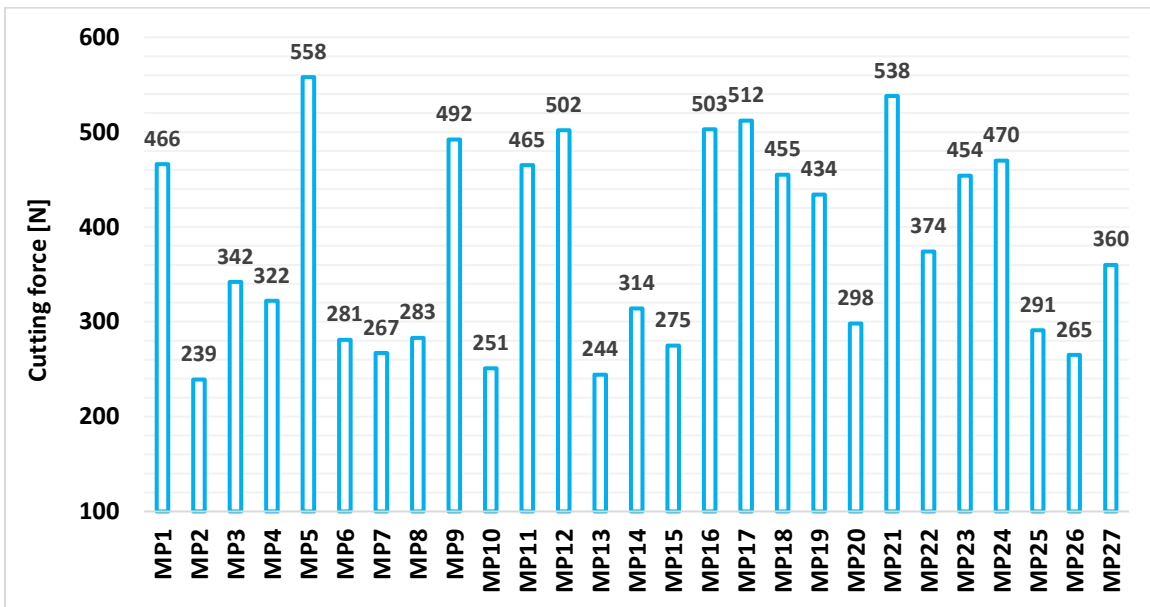


Fig. 6-5. FE predictions of cutting force for 27 design points in DoE.

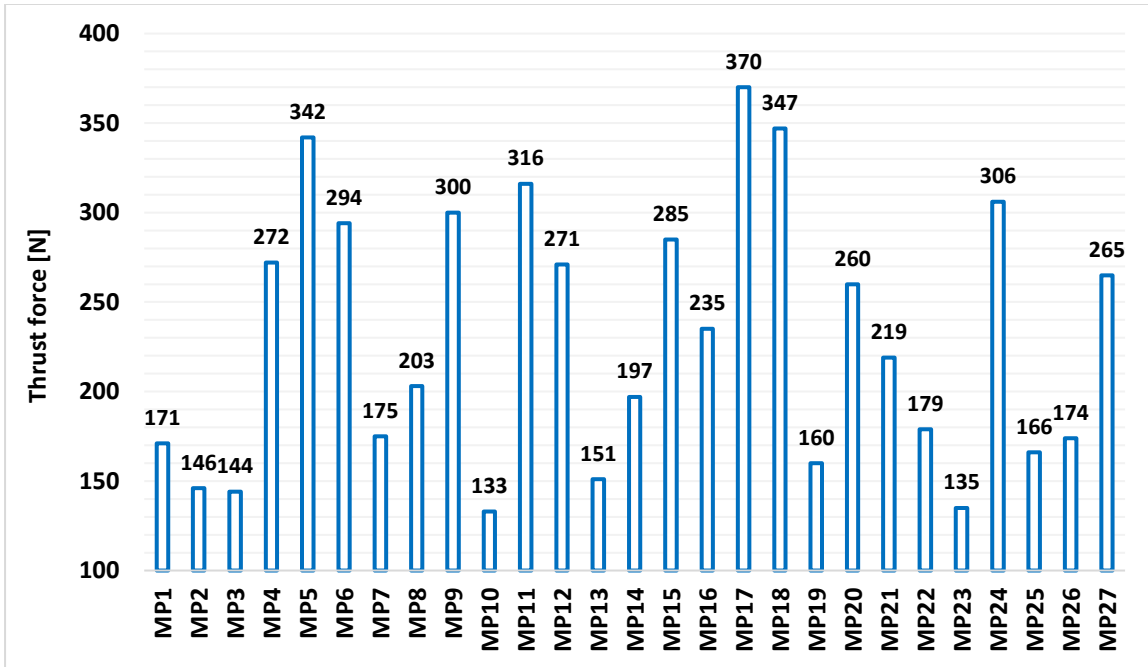


Fig. 6-6. FE predictions of thrust force for 27 design points in DoE.

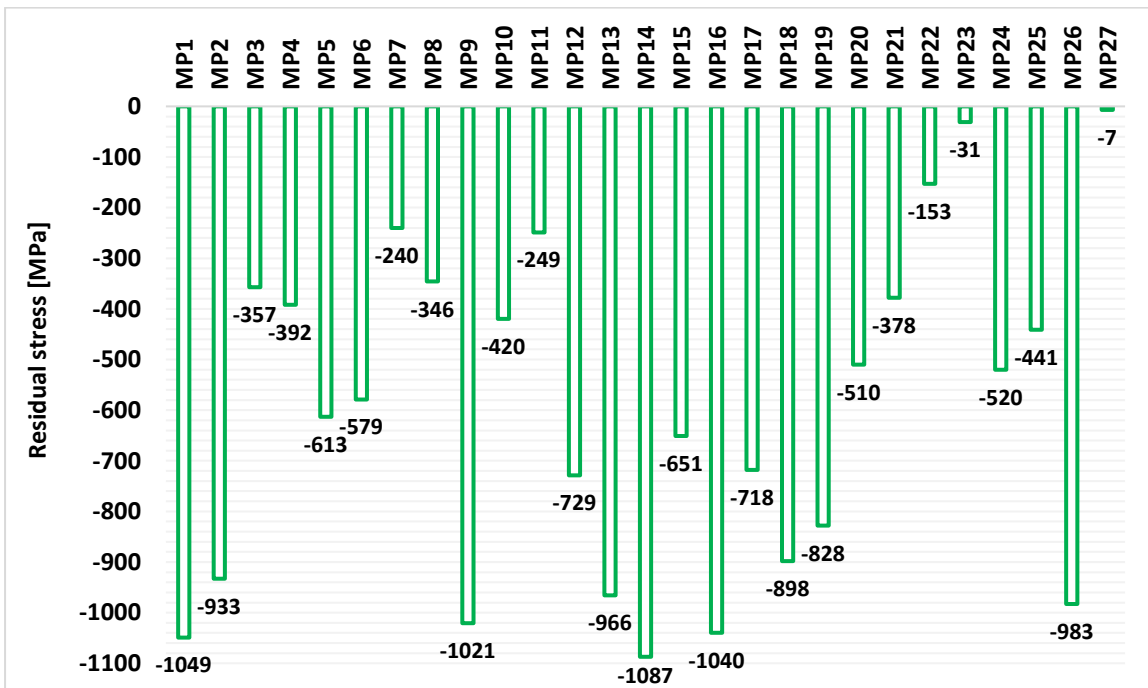


Fig. 6-7. FE predictions of superficial residual stress for 27 design points in DoE.

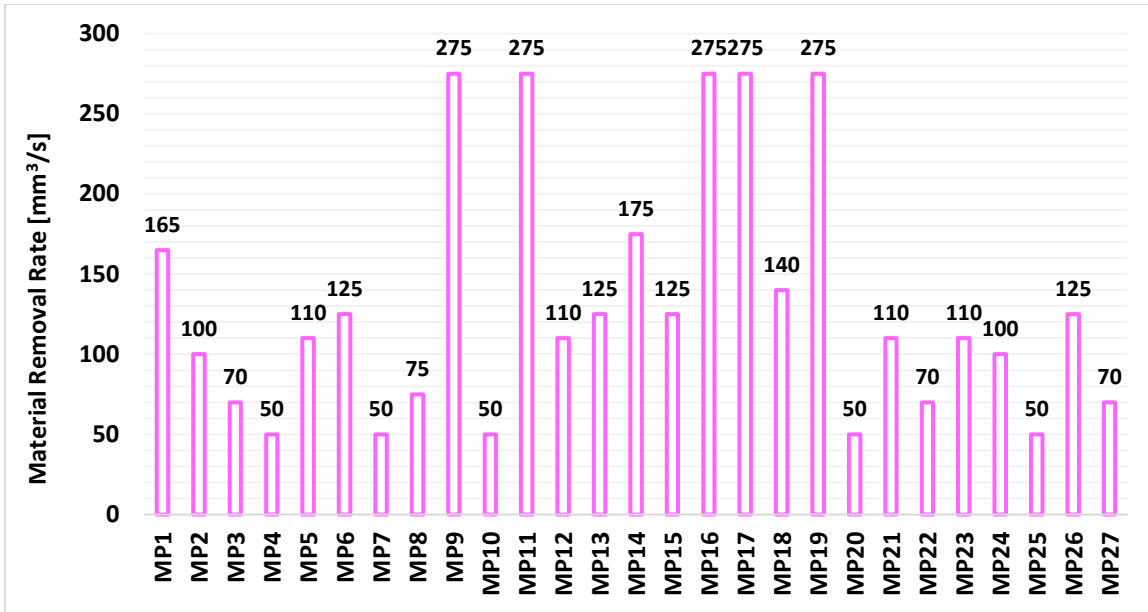


Fig. 6-8. FE predictions of material removal rate for 27 design points in DoE.

The response variables are formulated in terms of cutting speed ( $V$  [mm / s]), feed rate ( $f$  [mm / rev]), edge radius ( $r_\beta$  [mm]), rake angle ( $\gamma_0$  [deg]), and clearance angle ( $\alpha_0$  [deg]) using RSM by the second-order polynomial regression models whose coefficients are calculated using the Least Square Technique and provided in Table 6-7. The values of the coefficients of determination, i.e.  $R^2$  values, are calculated for response functions and furnished in Table 6-7. These values show that the quadratic models of response variables are well approximated by response surface method.

**Table 6-7**

Regression coefficients and coefficients of determination  $R^2$  for the quadratic functions of cutting temperature, machining forces, and residual stresses

Parameter	$T [^{\circ}C]$	$F_c [N]$	$F_t [N]$	$\sigma_{surf} [MPa]$
Intercept	363.8	-0.352239	3.67025	1645
$V$	0.37047	0.3233098	0.0814948	-3.280
$f$	1420	1735	234.7	1381
$r_p$	3912	-808.4	2083	3445
$\gamma_o$	-6.269	-4.691	-1.9286	-67.397
$\alpha_o$	-6.436	-4.3	0.21754	-104.602
$V \times f$	-0.22201	-0.0540837	0.128328	3.011
$V \times r_p$	-0.05001	-0.1127923	0.4682812	18.505
$V \times \gamma_o$	0.003043	0.00197878	0.000651924	0.00127575
$V \times \alpha_o$	0.001485	-0.00163506	-0.000137332	0.00598917
$f \times r_p$	-139.5	-11484	3927	-57076
$f \times \gamma_o$	16.471	-71.406	-52.751	228.914
$f \times \alpha_o$	6.828	30.255	1.5952	-90.854
$r_p \times \gamma_o$	47.729	147.137	56.446	269.731
$r_p \times \alpha_o$	-38.66	-64.705	-17.498	-656.979
$\gamma_o \times \alpha_o$	-0.010871	-0.24942	-0.0663381	-0.658232
$V^2$	-0.000064725	-0.000143179	-0.0000414568	0.000688514
$f^2$	-5292	5502	734.662	-15643
$r_p^2$	-23772	37422	12671	-109158
$\gamma_o^2$	-0.0149546	0.324077	0.157083	3.210
$\alpha_o^2$	0.3332882	0.350505	0.0468066	7.083
$R^2$	0.9984	0.9460	0.9982	0.8936

#### 6.4. Multi-objective optimization problem formulation

Using the response functions obtained in the previous section and  $MRR [mm^3/s] = V [mm/s] \times f [mm] \times 1 [mm]$  (where  $MRR$  is calculated for unit width/depth of cut, which is the case in FE simulations), a general multi-criteria optimization problem based on the desired performances can be formally formulated as follows:

Find  $V, f, r_\beta, \gamma_0$  and  $\alpha_0$  to

$$\text{Minimize } OF = w_{\sigma_{Surf}} \left( \frac{\sigma_{Surf}}{|\sigma_{Surf, avg}|} \right) + w_T \left( \frac{T}{T_{avg}} \right) + w_{F_c} \left( \frac{F_c}{F_{c, avg}} \right) + w_{F_t} \left( \frac{F_t}{F_{t, avg}} \right) + w_{MRR} \left( \frac{MRR_{avg}}{MRR} \right)$$

$$\text{Subject to } CF_1 = \left( \frac{T}{T_{avg}} - 1 \right) \leq 0$$

$$CF_2 = \left( \frac{F_c}{F_{c, avg}} - 1 \right) \leq 0$$

$$CF_3 = \left( \frac{F_t}{F_{t, avg}} - 1 \right) \leq 0$$

$$CF_4 = \left( \frac{MRR_{avg}}{MRR} - 1 \right) \leq 0$$

$$CF_5 = \left( \frac{\sigma_{Surf}}{|\sigma_{Surf, avg}|} + 1 \right) \leq 0$$

$$0 \leq w_{\sigma_{Surf}}, w_T, w_{F_c}, w_{F_t}, w_{MRR} \leq 1 \text{ and } w_{\sigma_{Surf}} + w_T + w_{F_c} + w_{F_t} + w_{MRR} = 1$$

(6-1)

where  $OF$  is the total multi-objective function,  $w_{\sigma_{Surf}}$ ,  $w_T$ ,  $w_{F_c}$ ,  $w_{F_t}$ , and  $w_{MRR}$  are in turn the weighting coefficients (factors) of non-dimensional superficial residual stress, cutting temperature, cutting force, thrust force, and material removal rate. Also, the symbol  $||$  shows an absolute value.

$CF_1$ ,  $CF_2$ ,  $CF_3$ ,  $CF_4$ , and  $CF_5$  are inequality behavior constraints, and  $\sigma_{Surf_{avg}} = -597.7 \text{ MPa}$ ,  $T_{avg} = 857.3 \text{ }^\circ\text{C}$ ,  $F_{c_{avg}} = 379.8 \text{ N}$ ,  $F_{t_{avg}} = 230.2 \text{ N}$ , and  $MRR_{avg} = 130.7 \text{ mm}^3 / \text{s}$  are in turn the average values of the predicted cutting temperatures, cutting forces, thrust forces, and material removal rates presented in Figs. 6-4 to 6-8. The upper and lower bounds of the design variables, known as side constraints, are also provided in Table 6-8. It needs mentioning that when the average values in the constraints in Eq. (6-1) are replaced by the best values of 27 design points in DoE, i.e. minimum values of temperature, cutting force, thrust force, and surface residual stress (the highest compressive residual stress), and maximum value of MRR, the optimization problem cannot find a feasible solution owing to becoming over-constrained.

**Table 6-8**

The upper and lower bounds of the design variables in the optimization process

Design variable	$V$ [m / min]	$f$ [mm / rev]	$r_\rho$ [mm]	$\gamma_o$ [deg]	$\alpha_o$ [deg]
Upper bound	100	0.165	0.060	12	15
Lower bound	40	0.075	0.030	0	3

## 6.5. Optimization results

The present research aims mainly at optimizing surface residual stresses against machining parameters including cutting conditions and tool geometry. Therefore, the optimization of residual stresses is studied separately in the next subsection. Then, multi-objective optimizations of residual stresses, cutting temperature, machining forces, and material removal rate are performed. Since the residual stresses are the key responses for machined component life and performance, their weighting coefficients are considered to be large in order to maintain their contribution to the total objective function high, compared to the other response variables. It should be mentioned that the values of weighting coefficients are generally selected based on the required application and the desired goal. For instance, when the surface integrity and resistance of the machined component to fatigue are the major concerns, the weighting coefficients of residual stresses should be the greatest ones.

### 6.5.1. Optimization of residual stresses

Two cases of constrained and unconstrained optimization of superficial residual stresses are considered ( $w_{\sigma_{Surf}} = 1$  and  $w_T = w_{F_c} = w_{F_t} = w_{MRR} = 0$ ). The constrained optimization problem includes constraints  $CF_1$ ,  $CF_2$ ,  $CF_3$ , and  $CF_4$  in Eq. (6-1). The unconstrained optimization problem is defined as an optimization problem without any behavior constraints on response variables, i.e. without  $CF_1$ ,  $CF_2$ ,  $CF_3$ ,  $CF_4$ , and  $CF_5$ . However, for all the optimization problems in this research, there are side constraints on the design variables. As described earlier, the optimization is carried out using a combination of GA and SQP. Different values of 'Population

Size' from 50 to 400, 'Crossover Fraction' from 0.70 to 0.90, and 'Elite Count' from 2 to 20 are explored in the optimization tool of GA to ensure that the most accurate optimum value is obtained. Moreover, the number of 'Generations', 'Stall Generations', 'Function Tolerance', and 'Constraint Tolerance' as stopping criteria in the GA tool are set to 500, 50,  $1 \times 10^{-6}$ , and  $1 \times 10^{-6}$ , respectively. In the SQP optimization process, 'Maximum Iterations', 'Maximum Function Evaluations', 'Function Tolerance', and 'Constraint Tolerance' as stopping criteria are in turn set to 1000, 5000,  $1 \times 10^{-6}$ , and  $1 \times 10^{-6}$ .

The optimum values of machining parameters, individual objective functions, constraint functions, total objective function ( $OF_{Optimum}$ ) as well as the smallest value of the total objective function ( $OF_{Smallest}$ ) and corresponding Run No. in the 27 design points in DoE, are provided in Table 6-9. The percentage improvement in the total objective function with respect to the smallest value of the total objective function ( $OF_{Smallest}$ ) in the 27 design points in DoE, is calculated as  $((OF_{Optimum} - OF_{Smallest}) / OF_{Smallest}) \times 100$  and also given in Table 6-9. It needs mentioning that the optimum machining parameters of Case A (for instance) using GA are  $V = 1181.93 \text{ mm/s}$  ( $70.9158 \text{ m/min}$ ),  $f = 0.122112 \text{ mm/rev}$ ,  $r_\beta = 0.03 \text{ mm}$ ,  $\gamma_0 = 5.577097 \text{ deg}$ , and  $\alpha_0 = 9.220428 \text{ deg}$ . When this optimum solution is utilized as an initial point for SQP, it provides  $V = 1182 \text{ mm/s}$  ( $70.92 \text{ m/min}$ ),  $f = 0.120200 \text{ mm/rev}$ ,  $r_\beta = 0.03 \text{ mm}$ ,  $\gamma_0 = 5.577100 \text{ deg}$  and  $\alpha_0 = 9.220400 \text{ deg}$  as the global optimum point (the values given in Table 6-9 are rounded off). This confirms that GA provides near optimum solution, while the hybrid GA-SQP strategy catches the true global optimum point.

**Table 6-9**

Optimum values of machining parameters and objective and constraint functions

<b>Machining parameters</b>	<b>Case A</b>	<b>Case B</b>
$V$ [m / min]	71	100
$f$ [mm / rev ]	0.1202	0.075
$r_\rho$ [mm ]	0.03	0.03
$\gamma_0$ [deg]	6	7
$\alpha_0$ [deg]	9	9
<b>Objective function</b>		
$\sigma_{Surf} / \left  \sigma_{Surf_{avg}} \right $	-1.8879	-2.3362
<b>Constraint functions</b>		
$(T / T_{avg}) - 1$	$-6.0895 \times 10^{-5}$	NA
$(F_c / F_{c_{avg}}) - 1$	-0.0061	NA
$(F_t / F_{t_{avg}}) - 1$	-0.2484	NA
$(MRR_{avg} / MRR) - 1$	-0.0941	NA
<b>Total functions</b>		
$OF_{Optimum}$	-1.8879	-2.3362
$OF_{Smallest}$ /Run No.	-1.8186 / 14	-1.8186 / 14
Improvement (%)	3.81	28.46

NA: Not Assigned

As observed in Table 6-9, for the constrained optimization problem, Case A, optimal values for cutting speed and feed rate approach the intermediate values in the given bounds, showing that the lower and upper bounds for the cutting velocity and feed rate are inactive side constraints and have no effect on their optimal values. In contrast, for the unconstrained optimization problem, Case B, the cutting speed converges to the upper bound, while the feed has a tendency toward the lower bound. The optimal values for edge radius for both cases are located at the lower bound, indicating that a smaller edge radius is desirable for improving residual stresses. The optimal values for rake

and clearance angles converge neither to the lower bound nor to the upper one, denoting that the given bounds are inactive side constraints and have less influence on the optimum solution. For Case A, it is observed that the cutting temperature and cutting force constraints are almost zero and hardly satisfied, representing that they are active constraints in the optimization process and have the main competition among the constraints. The constraints of MRR is close to zero, denoting that it is nearly active ( $\epsilon$ -active) and contribute to the optimization process to a certain extent. Moreover, the trust force constraint is an inactive constraint, indicating that it does not affect the optimum results in the presence of the other above-mentioned constraints.

The competing influences of machining parameters operating during cutting can be considered to understand the trends observed herein. For example, a high cutting speed is expected to result in smaller cutting forces, as shown in the flowchart in Fig. 6-9a, in which a higher cutting velocity generates larger frictional and plastic works, leading to more thermal softening, and as a result, produces smaller cutting forces [17]. In contrast, a high cutting speed can also cause a greater material removal rate, yielding a lower cutting temperature [161] and larger cutting forces, as shown in Fig. 6-9b. In a cutting process, based on the findings of the previous studies, the contribution of the former is greater than or almost equal to that of the latter. This means that the cutting forces can decrease [17,117] and/or remain almost constant [71,117] with the cutting velocity, depending on the range in which the magnitude of the cutting velocity changes, as described in Fig. 6-9c. For the cutting feed effects, an increment in feed increases the tool-chip contact area and directly raises the cutting forces [9,62,71,117,159]. In contrast, a rise in feed rate may indirectly decline the cutting forces due to increasing the frictional area, which produces more heat and softens the material [17]. These effects are shown in the flowchart in Fig. 6-10. Therefore,

in a cutting process, the magnitude of cutting temperature and forces depend significantly on the competition between the two afore-mentioned phenomena.

The optimal values of the normalized objective functions are found to be -1.8879 and -2.3362 for Cases A and B, respectively, which is corresponding to the optimal values of the residual stresses equal to -1128.5 and -1396.5 MPa in turn for Cases A and B. As seen in Table 6-9, the percentage improvement when the optimization is carried out without constraints (Case B) is 28.46%, which is much higher than that when the optimization is performed with constraints (Case A), i.e. 3.81%. This can be attributed to the fact that there is more freedom in an unconstrained optimization process for machining parameters to be adjusted to improve residual stresses, compared with a constrained problem.

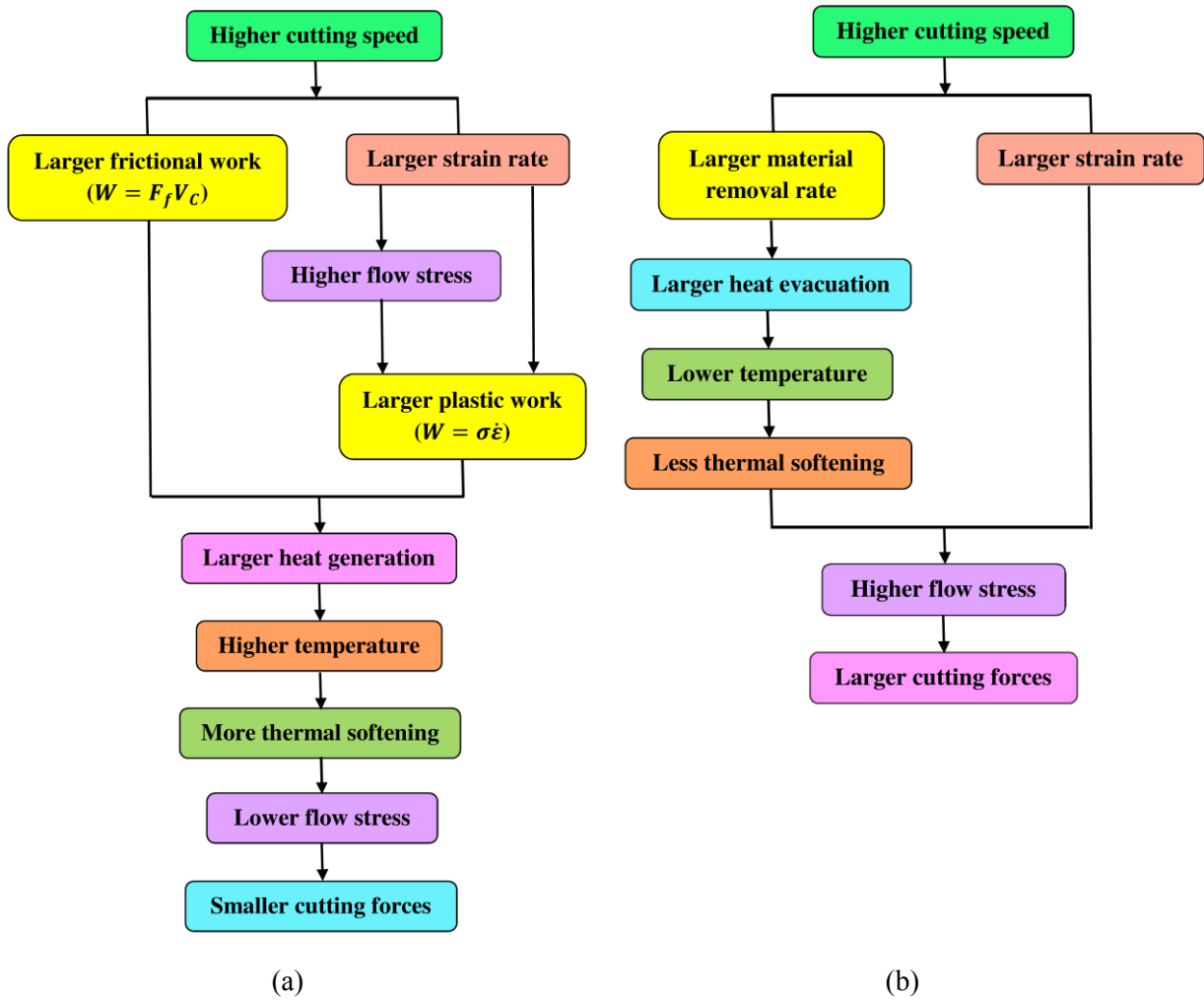
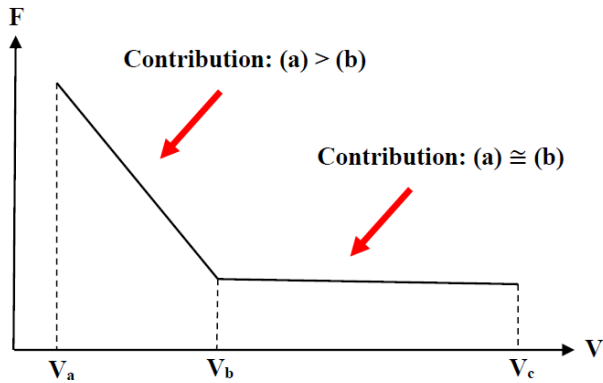


Fig. 6-9. Influence of cutting speed on cutting forces:

(a) via affecting the frictional and plastic works, where  $F_f$  is frictional force,  $V_c$  cutting velocity,  $\sigma$  flow stress,  $\dot{\epsilon}$  strain rate, and  $W$  the work done, and (b) via affecting material removal rate and strain rate.



Three states are possible:

- 1) If the selected cutting speeds ( $V$ ) in DoE are:  $V_a < V < V_b$ , cutting forces decrease.
- 2) If the selected cutting speeds ( $V$ ) in DoE are:  $V_b < V < V_c$ , cutting forces remain almost constant.
- 3) If the selected cutting speeds ( $V$ ) in DoE are:  $V_a < V < V_c$ , cutting forces first decrease and then remain almost constant.

(c)

Fig. 6-9. Influence of cutting speed on cutting forces: (c) the general trend (*continued*).

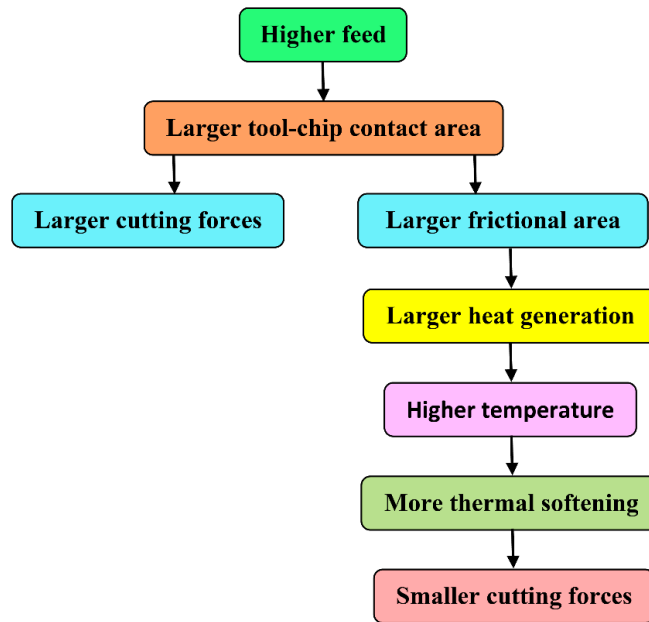


Fig. 6-10. Competing effects of feed on cutting forces.

### ***6.5.2. Optimization of residual stresses, cutting temperature, machining forces, and material removal rate***

In this section, multi-objective optimizations of superficial residual stresses, cutting temperature, cutting and thrust forces, and material removal rate are conducted simultaneously. Three configurations of the total objective function based on different weighting coefficients whose values are given in Table 6-10, are examined. Similar to the single-objective optimization of residual stresses, the percentage improvement in the total objective function for all the multi-criteria optimization problems with constraints  $CF_1$ ,  $CF_2$ ,  $CF_3$ ,  $CF_4$ , and  $CF_5$  in Eq. (6-1) is found to be very small. Hence, the unconstrained optimizations of residual stresses, cutting temperature, machining forces, and material removal rate, which are defined as Cases U, V, and W, are investigated.

The optimum machining parameters and objective and constraint functions, the smallest total objective function in the design space and corresponding Run No, and the percentage improvement in the total objective function are provided in Table 6-11. As observed in this table, for Cases U and V, where the weight of residual stresses in the total objective function is dominant, all the optimal values of machining parameters are the same. This shows the governing effect of residual stresses on the total objective function compared with the other response variables. In contrast, from Cases U and V to Case W, the optimum magnitudes of both feed and rake angle rise with decreasing the weight of superficial residual stress and increasing that of cutting temperature, machining forces, and MRR. The increase in the feed can be due to the increase of the weight of MRR in the objective function. By increasing the feed, the cutting forces can rise. As a result, the rake angle increases to reduce forces. This change in the rake angle can be attributed to the

influence of rake angle on cutting and thrust forces as it is well recognized that cutting forces generally decrease when rake angle rises in the positive direction [62,80]. The equality of optimal values of cutting speed, edge radius, and clearance angle for all the cases under study indicates that the assigned weighting factors have no impact on the optimal values of these machining parameters. However, the weighting factors have a large influence on the total objective function. As seen in Table 6-11, the best optimum value of the total objective function is related to Case U (-1.0628), while the worst one is associated with Case W (0.2095). In addition, the percentage improvement in the total objective function with respect to the smallest value of the total objective function in the 27 design points in DoE is the highest for Case V (about 123%) and lowest for Case W (about 40%).

It should also be mentioned that the individual objective functions of cutting temperature and material removal rate are close to one for all the cases considered, showing that they are hardly optimized, and consequently, the main competition is between these two response variables in the multi-objective optimizations. In contrast, surface residual stress is highly improved, followed by cutting force and then thrust force.

**Table 6-10**

Weighting coefficients of the individual objective functions for multi-objective optimization of residual stresses, cutting temperature, machining forces, and material removal rate

Case	$w_{\sigma_{Surf}}$	$w_T$	$w_{F_c}$	$w_{F_t}$	$w_{MRR}$
U	0.60	0.10	0.10	0.10	0.10
V	0.40	0.15	0.15	0.15	0.15
W	0.20	0.20	0.20	0.20	0.20

**Table 6-11**

Optimum values of machining parameters and the corresponding objective and constraint functions

<b>Machining parameters</b>	Case U	Case V	Case W
$V$ [m / min]	100	100	100
$f$ [mm / rev ]	0.075	0.075	0.081
$r_\beta$ [mm ]	0.03	0.03	0.03
$\gamma_0$ [deg]	7	7	8
$\alpha_0$ [deg]	9	9	9
<b>Objective functions</b>			
$\sigma_{Surf} / \left  \sigma_{Surf_{avg}} \right $	-2.3362	-2.3362	-2.2998
$T / T_{avg}$	1.0993	1.0993	1.1036
$F_c / F_{c_{avg}}$	0.5922	0.5922	0.6223
$F_t / F_{t_{avg}}$	0.6518	0.6518	0.6531
$MRR_{avg} / MRR$	1.0457	1.0457	0.9683
<b>Total functions</b>			
$OF_{Optimum}$	-1.0628	-0.4261	0.2095
$OF_{Smallest}$ /Run No.	-0.7336 / 14	-0.1912 / 14	0.3513 / 14
Improvement (%)	44.87	122.86	40.36

# **CHAPTER 7    Conclusions, Contributions, Future Works, and Outlook**

## **7.1. Introduction**

This chapter highlights the major conclusions of the present research thesis and the main contributions to the advancement of knowledge in the field of FE modeling and optimization of machining processes. Also, it presents future works (extensions of the present research) and some recommendations for possible future studies along this field. Finally, an outlook on FE-based optimizations of machining operations is given.

## **7.2. Summary and Conclusions**

Hard-to-cut materials are frequently used in the automotive and aerospace industries. 300M steel is a high strength difficult-to-machine material, which is used in a variety of applications including landing gears of aircrafts, drive-shafts of automobiles, and high strength bolts and frame parts of airplanes and motorsports due to its high toughness and resistance to fatigue and corrosion. Despite of these applications, 300M steel is not much studied from machining and surface integrity standpoints. Machining hard-to-cut materials produces high cutting temperatures and forces and leaves residual stresses in the machined components. It is well recognized that high temperatures cause inaccuracies in component dimensions and phase transformation. Large machining forces also increase the power consumption of turning machines and cause an excessive deflection and

breakage of the tool. In addition, both high machining temperatures and forces result in tool wear. Most importantly, residual stresses are induced due to machining. It is known that cracks normally initiate at the surface of components. As a result, surface residual stresses are important in assessing the potential for crack initiation and propagation which reduce the resistance of components to fatigue and stress corrosion cracking. On the other hand, the machining process needs to be efficient by removing material as large as possible. Hence, optimization of machining parameters including cutting speed, feed rate, edge radius, rake angle, and clearance angle to improve residual stresses, cutting temperature, machining forces, and material removal rate is greatly desirable and important to the industry. Utilizing optimal machining parameters provide the industry to have more economical, reliable, and thus valuable outcome, increasing the efficiency of production significantly in today's competitive world.

In the present research, first, a predictive finite element tool was developed using Abaqus software to predict machining forces, cutting temperatures, and residual stresses caused by the orthogonal radial turning of 300M steel. This involved applying proper mechanical, thermal, material, and frictional properties; prescribing mechanical and thermal boundary conditions; implementing thermal and mechanical interactions between the workpiece and tool; generating an adaptive mesh, and specifying proper remeshing parameters. The errors generated by the FE model were analyzed and ratified step by step to reach the final solution. Employing predictive FE models allow the experts in industry to conduct a much smaller number of experiments, leading to saving time, money, and energy.

The orthogonal turning experiment was conducted using a CNC lathe and the machining forces were measured using a piezoelectric dynamometer. The thickness of the collected chip was also

measured with a digital micrometer. The machining zone on the workpiece which was a representative of the actual cutting condition was identified by measuring the circularity profile of the workpiece component using a coordinate measuring machine. The residual stress profile in this zone was then experimentally obtained using X-Ray Diffraction, Electropolishing, and Profilometer machines. The finite element model was validated by comparing the predicted foregoing quantities with the measured ones.

Response functions for finite element output quantities were derived using design of experiment and response surface method. A multi-performance optimization problem was formulated and then solved using the combination of genetic algorithm and sequential quadratic programming method. The optimization problems were aimed at reducing superficial residual stresses individually and improving a combination of residual stresses, cutting temperature, cutting and thrust forces, and material removal rate by obtaining optimum values of machining parameters including cutting speed, feed rate, edge radius, rake angle, and clearance angle. Special attention was devoted to minimizing the machining-induced residual stresses.

The optimization results showed that the unconstrained single-objective optimization of residual stresses provided higher cutting speed and lower feed rate than the corresponding constrained one. For the unconstrained problems, the feed had a tendency toward the smallest value in the given bound when the residual stress had a very high contribution to the total objective function. All the single- and multi-objective optimization problems showed that a small edge radius and medium values of rake and clearance angles in the given bound were desirable to decrease residual stresses. It was also found that for the constrained problems, the main competition was mainly between the constraints of cutting temperature and cutting force to be

simultaneously satisfied as they were active constraints. Moreover, the constraint of MRR was nearly active, while the thrust force constraint was inactive, having no effect on the optimum solution. For constrained and unconstrained single- and multi-criteria optimizations, cutting temperature was the most important quantity to be satisfied in the optimization process. The results also demonstrated that the weighting factors had a large impact on the optimum values of the total objective function, showing the importance of assigning proper magnitudes of weighting coefficients in the total objective function depending on the required application and main objectives. Finally, the percentage improvement in the total objective function with respect to the smallest value of the total objective function in the 27 design points in DoE for the unconstrained optimization problem was much larger than that for the constrained one. This can be due to the fact that there are more degrees of freedom for machining parameters to be adjusted in order to improve the total objective function in an unconstrained optimization process than in a constrained one.

Since there are no results on finite element modeling, experimental test, and multi-criteria optimization of machining-induced residual stresses for 300M steel, the findings of the present study can be utilized as a reference for future works along this area of research.

### 7.3. Contributions

The main contributions to the advancement of the field of finite element modeling and optimization of machining operations made by the present study can be summarized as follows:

1. This research is the *first* study on finite element simulation and modeling of both cutting process and residual stresses in radial (orthogonal) turning of a difficult-to-machine material named 300M steel.

In general, there are some FE models of orthogonal turning for other steels, most of which suffer from either using chip separation criteria affecting the residual stresses or using Eulerian and Lagrangian boundaries requiring the knowledge of chip geometry in advance. In addition, the majority of the previous finite element analyses focused only on modeling the cutting process. Also, some of the studies which modeled the residual stress step only validated the residual stresses without validating the cutting forces or chip morphology in the cutting step.

2. The present study provides *new results* on optimization of residual stresses *with* and *without* constraints of cutting temperature, cutting force, thrust force, and material removal rate in turning of 300M steel.
3. This research work presents the *first comprehensive optimization study* of *five response variables* of turning process including residual stresses, cutting temperature, cutting force, thrust force, and material removal rate.
4. This research, contrary to the previous studies, provides *more comprehensive* optimization results by including all the important *tool geometry parameters* in the design variables.

5. This study furnishes a number of *new experimental results* on residual stresses and machining forces for *radial orthogonal turning* of 300M steel.
6. Finite element simulation of turning processes is a challenging, computationally very expensive task due to high material nonlinearity resulting from high strain, strain rate and temperature, high geometrical nonlinearity caused by large element distortion due to chip formation, and a large volume of computations owing to simultaneous calculation of temperatures and displacements in a coupled thermo-mechanical, dynamic process. Hence, performing optimization algorithm on the full finite element model of the cutting and stress relaxation processes will be computationally very expensive and time-consuming as at each optimization iteration, the finite element model may be called several times while each FE run by itself demands high computations and run time. Accordingly, *in this research study, to avoid performing simulation and optimization runs at the same time, design of experiment combined with response surface method have been utilized to accurately generate explicit functions of the desired response variables using the finite element predictions for the identified cutting conditions and tool geometry parameters. Then, these functions are effectively used as the objective and constraint functions in the optimization process* using the hybrid method of Genetic Algorithm - Sequential Quadratic Programming algorithm to capture the global optimum point precisely.

Based on the above-mentioned contributions, some papers are published, under review, or in preparation as follows:

- 1- Morteza Sadeghifar, Ramin Sedaghati, Walid Jomaa, Victor Songmene. Finite element analysis and response surface method for robust multi-performance optimization of radial turning of hard 300M steel. *International Journal of Advanced Manufacturing Technology*, *In press*, DOI: 10.1007/s00170-017-1032-4, 2017.
- 2- M. Sadeghifar, R. Sedaghati, V. Songmene. FE modeling and optimization of cutting temperature in orthogonal turning. In: 24th International Congress of Theoretical and Applied Mechanics (ICTAM 2016), Palais des congrès, Montréal, Canada, August 21-26, 2016.
- 3- Morteza Sadeghifar, Ramin Sedaghati, Walid Jomaa, Victor Songmene. A comprehensive review of finite element modeling of orthogonal machining process: Chip formation and surface integrity predictions. *Submitted to Journal of Manufacturing Science and Engineering*, Paper Number: MANU-17-1555, 2017.
- 4- Morteza Sadeghifar, Ramin Sedaghati, Walid Jomaa, Victor Songmene. Machining forces and residual stresses in nose turning of 300M steel: Experimental measurements and finite element simulations using DEFORM-3D software. *In preparation, to be submitted to International Journal of Machine Tools and Manufacture*, 2017.
- 5- Morteza Sadeghifar, Ramin Sedaghati, Walid Jomaa, Victor Songmene. Experimental analysis and multi-criteria optimization of superficial residual stresses, material removal rate, and machining forces in nose turning of 300M steel. *In preparation, to be submitted to Journal of Manufacturing Processes*, 2017.

#### **7.4. Future Works**

The author of the present thesis, along with his PhD research, has contributed to some other projects on experimental and numerical investigations of machining of two hard-to-cut materials Inconel 718 and 300M steel. These studies are carried out under the industrial project entitled CRIAQ MANU510, funded by CRIAQ, NSERC, and companies Héroux-Devtek Inc. (HD) and Pratt & Whitney Canada (P&WC). The projects will be completed in the future and the tools and results will belong to the industrial partners. Due to confidentiality concerns, the results will be published if official permission is granted by the industrial collaborators. These projects are addressed as follows:

- 1- Influence of tool's edge preparation on machining forces and residual stresses in micro-cutting of Inconel 718
- 2- Effect of tool geometry and material on chip thickness, cutting forces and residual stresses in micro-turning of 300M steel
- 3- Finite element modeling of orthogonal turning of Inconel 718

## **7.5. Recommendations for Future Works**

Future research related to this study is suggested to concentrate on the following aspects:

- i. Finite element simulation of both cutting process and residual stress steps can be conducted for more complex machining operations including milling and drilling of 300M steel. Other cutting tool materials such as PCBN, tungsten carbide, or coated tools can also be utilized and the results can be compared.
- ii. Unconstrained optimization of residual stresses and optimization with constraints of cutting temperature, cutting force, thrust force, and material removal rate can be performed for nose turning, milling, drilling, or micro-cutting of 300M steel.
- iii. Different cases of optimization study of machining processes including optimization of residual stresses and cutting temperature, optimization of residual stresses and machining forces, optimization of residual stresses, cutting temperature, and material removal rate, etc. may be performed. The optimization process can also be carried out with other numerical optimization methods such as simulated annealing, particle swarm, ant colony, and artificial bee colony algorithms.
- iv. An experimental study may be conducted to measure machining forces for different cutting speeds and feed rates in order to identify a more accurate frictional model in terms of cutting conditions to improve the frictional behavior at the tool-chip-workpiece interfaces. This assists to obtain more accurate cutting temperature, machining forces, and residual stresses using finite element method.

## **7.6. Outlook**

The demand for high-quality components with low cost and short production time pushes manufacturing companies to reduce costly, time- and energy-consuming methods for economically and accurately modeling manufacturing processes, and specially, machining operations. This opens up various directions for future research on finite element simulations and optimizations of unresolved machining and surface integrity problems. Challenging tasks are to reduce the high computational time and increase the results' accuracy in simulations. By advancing computer software and improving numerical techniques in the finite element method, the simulation time of machining operations can be decreased. In addition, by modifying and enhancing input physical models into the finite element model such as material constitutive and frictional behaviors, the accuracy of the results can be augmented. On the other hand, the need for decreasing the budget devoted to apparatus, material, and human resources required for experimental measurements in the industry will make the cheap process of model building using FE method and multi-performance optimization of machining and surface integrity characteristics much more desirable. Therefore, considering the practical usage of finite element modeling and simulation-based optimizations, they will receive increasing attention and will be extended to all machining and metal forming processes in the coming years.

## References

- [1] Z.T. Tang, Z.Q. Liu, Y.Z. Pan, Y. Wan, X. Ai, The influence of tool flank wear on residual stresses induced by milling aluminum alloy, *J. Mater. Process. Technol.* 209 (2009) 4502-4508.
- [2] D.W. Tang, C.Y. Wang, Y.N. Hu, Y.X. Song, Finite-element simulation of conventional and high-speed peripheral milling of hardened mold steel, *Metall. Mater. Trans. A* 40 (2009) 3245-3257.
- [3] B. Wang, Zh. Liu, Investigations on the chip formation mechanism and shear localization sensitivity of high-speed machining Ti6Al4V, *Int. J. Adv. Manuf. Technol.* 75 (2014) 1065-1076.
- [4] E. Bagci, B. Ozcelik, Finite element and experimental investigation of temperature changes on a twist drill in sequential dry drilling, *Int. J. Adv. Manuf. Technol.* 28 (2006) 680-687.
- [5] T. Matsumura, S. Tamura, Cutting simulation of titanium alloy drilling with energy analysis and FEM, In: 15th CIRP Conference on Modelling of Machining Operations, *Procedia CIRP* 31 (2015) 252-557.
- [6] S. Eck, H.P. Ganser, S. Marsoner, W. Ecker, Error analysis for finite element simulation of orthogonal cutting and its validation via quick stop experiments, *Mach. Sci. Technol.* 19 (2015) 460-478.
- [7] A.P. Markopoulos, *Finite element method in machining processes*, First Ed., Springer, 2013.
- [8] [www.iscar.com](http://www.iscar.com) – 2017/07/06.
- [9] T. Ozel, T. Altan, Determination of workpiece flow stress and friction at the chip-tool contact for high-speed cutting, *Int. J. Mach. Tools Manuf.* 40 (2000) 133-152.
- [10] Y.B. Guo, Q. Wen, K.A. Woodbury, Dynamic material behavior modeling using internal state variable plasticity and its application in hard machining simulations, *J. Manuf. Sci. Eng.* 128 (2006) 749-759.
- [11] J.C. Outeiro, D. Umbrello, R. M'Saoubi, Experimental and numerical modeling of the residual stresses induced in orthogonal cutting of AISI 316L steel, *Int. J. Mach. Tools Manuf.* 46 (2006) 1786-1794.
- [12] D. Umbrello, Finite element simulation of conventional and high speed machining of Ti6Al4V alloy, *J. Mater. Process. Technol.* 196 (2008) 79-87.

- [13] R. Kountanya, I. Al-Zkeri, T. Altan, Effect of tool edge geometry and cutting conditions on experimental and simulated chip morphology in orthogonal hard turning of 100Cr6 steel, *J. Mater. Process. Technol.* 209 (2009) 5068-5076.
- [14] J.P. Davim, C. Maranhao, P. Faria, A. Abrao, J.C. Rubio, L.R. Silva, Precision radial turning of AISI D2 steel, *Int. J. Adv. Manuf. Technol.* 42 (2009) 842-849.
- [15] F. Jiang, J. Li, J. Sun, S. Zhang, Z. Wang, L. Yan, Al7050-T7451 turning simulation based on the modified power-law material model, *Int. J. Adv. Manuf. Technol.* 48 (2010) 871-880.
- [16] P.J. Arrazola, T. Ozel, Investigations on the effects of friction modeling in finite element simulation of machining, *Int. J. Mech. Sci.* 52 (2010) 31-42.
- [17] I. Uzun, K. Aslantas, Numerical simulation of orthogonal machining process using multilayer and single-layer coated tools, *Int. J. Adv. Manuf. Technol.* 54 (2011) 899-910.
- [18] N.B. Moussa, H. Sidhom, C. Braham, Numerical and experimental analysis of residual stress and plastic strain distributions in machined stainless steel, *Int. J. Mech. Sci.* 64 (2012) 82-93.
- [19] F. Jiang, L. Yan, Y. Rong, Orthogonal cutting of hardened AISI D2 steel with TiAlN-coated inserts - simulations and experiments, *Int. J. Adv. Manuf. Technol.* 64 (2013) 1555-1563.
- [20] S. Atlati, B. Haddag, M. Nouari, M. Zenasni, Thermomechanical modeling of the tool-work material interface in machining and its implementation using the ABAQUS VUINTER subroutine, *Int. J. Mech. Sci.* 87 (2014) 102-117.
- [21] M. Daoud, W. Jomaa, J.F. Chatelain, A. Bouzid, A machining-based methodology to identify material constitutive law for finite element simulation, *Int. J. Adv. Manuf. Technol.* 77 (2015) 2019-2033.
- [22] M.N.A. Nasr, Effects of sequential cuts on residual stresses when orthogonal cutting steel AISI 1045, In: 15th CIRP Conference on Modelling of Machining Operations, *Procedia CIRP* 31 (2015) 118-123.
- [23] A. Raczy, M. Elmadagli, W.J. Altenhof, A.T. Alpas, An Eulerian finite-element model for determination of deformation state of a copper subjected to orthogonal cutting, *Metall. Mater. Trans. A* 35A (2004) 2393-2400.
- [24] H. Bil, S.E. Kılıc, A.E. Tekkaya, A comparison of orthogonal cutting data from experiments with three different finite element models, *Int. J. Mach. Tools Manuf.* 44 (2004) 933-944.

- [25] L. Filice, F. Micari, S. Rizzuti, D. Umbrello, A critical analysis on the friction modelling in orthogonal machining, *Int. J. Mach. Tools Manuf.* 47 (2007) 709-714.
- [26] A. Ramesh, S.N. Melkote, Modeling of white layer formation under thermally dominant conditions in orthogonal machining of hardened AISI 52100 steel, *Int. J. Mach. Tools Manuf.* 48 (2008) 402-414.
- [27] T. Mabrouki, F. Girardin, M. Asad, J.F. Rigal, Numerical and experimental study of dry cutting for an aeronautic aluminium alloy (A2024-T351), *Int. J. Mach. Tools Manuf.* 48 (2008) 1187-1197.
- [28] S. Subbiah, S.N. Melkote, Effect of finite edge radius on ductile fracture ahead of the cutting tool edge in micro-cutting of Al2024-T3, *Mater. Sci. Eng. A* 474 (2008) 283-300.
- [29] S. Ranganath, C. Guo, P. Hegde, A finite element modeling approach to predicting white layer formation in nickel superalloys, *CIRP Ann. Manuf. Technol.* 58 (2009) 77-80.
- [30] I. Al-Zkeri, J. Rech, T. Altan, H. Hamdi, F. Valiorgue, Optimization of the cutting edge geometry of coated carbide tools in dry turning of steels using a finite element analysis, *Mach. Sci. Technol.* 13 (2009) 36-51.
- [31] J. Lorentzon, N. Järveström, B.L. Josefson, Modelling chip formation of alloy 718, *J. Mater. Process. Technol.* 209 (2009) 4645-4653.
- [32] M. Mohammadpour, M.R. Razfar, R. Jalili Saffar, Numerical investigating the effect of machining parameters on residual stresses in orthogonal cutting, *Simul. Model. Pract. Th.* 18 (2010) 378-389.
- [33] F. Akbar, P.T. Matienga, M.A. Sheikh, An experimental and coupled thermo-mechanical finite element study of heat partition effects in machining, *Int. J. Adv. Manuf. Technol.* 46 (2010) 491-507.
- [34] A. Muñoz-Sánchez, J.A. Canteli, J.L. Cantero, M.H. Miguélez, Numerical analysis of the tool wear effect in the machining induced residual stresses, *Simul. Model. Pract. Th.* 19 (2011) 872-886.
- [35] C. Shet, X. Deng, Finite element analysis of the orthogonal metal cutting process, *J. Mater. Process. Technol.* 105 (2000) 95-109.

- [36] C.R. Liu, Y.B. Guo, Finite element analysis of the effect of sequential cuts and tool-chip friction on residual stresses in a machined layer, *Int. J. Mech. Sci.* 42 (2000) 1069-1086.
- [37] G. Shi, X. Deng, C. Shet, A finite element study of the effect of friction in orthogonal metal cutting, *Finite Elem. Anal. Des.* 38 (2002) 863-883.
- [38] M. Barge, H. Hamdi, J. Rech, J.-M. Bergheau, Numerical modelling of orthogonal cutting: influence of numerical parameters, *J. Mater. Process. Technol.* 164-165 (2005) 1148-1153.
- [39] A.G. Mamalis, M. Horvath, A.S. Branis, D.E. Manolakos, Finite element simulation of chip formation in orthogonal metal cutting, *J. Mater. Process. Technol.* 110 (2001) 19-27.
- [40] Y.B. Guo, C.R. Liu, FEM analysis of mechanical state on sequentially machined surfaces, *Mach. Sci. Technol.* 6 (2002) 21-41.
- [41] M.R. Vaziri, M. Salimi, M. Mashayekhi, Evaluation of chip formation simulation models for material separation in the presence of damage models, *Simul. Model. Pract. Th.* 19 (2011) 718-733.
- [42] L.-J. Xie, J. Schmidt, C. Schmidt, F. Biesinger, 2D FEM estimate of tool wear in turning operation, *Wear* 258 (2005) 1479-1490.
- [43] T. MacGinley, J. Monaghan, Modelling the orthogonal machining process using coated cemented carbide cutting tools, *J. Mater. Process. Technol.* 118 (2001) 293-300.
- [44] H.Y. Wu, W.B. Lee, C.F. Cheung, S. To, Y.P. Chen, Computer simulation of single-point diamond turning using finite element method, *J. Mater. Process. Technol.* 167 (2005) 549-554.
- [45] K. Khalili, M. Safaei, FEM analysis of edge preparation for chamfered tools, *Int. J. Mater. Form.* 2 (2009) 217-224.
- [46] U.M. Reddy Paturi, S.K. Reddy Narala, R. Singh Pundir, Constitutive flow stress formulation, model validation and FE cutting simulation for AA7075-T6 aluminum alloy, *Mater. Sci. Eng. A* 605 (2014) 176-185.
- [47] R.T. Coelho, E.G. Ng, M.A. Elbestawi, Tool wear when turning hardened AISI 4340 with coated PCBN tools using finishing cutting conditions, *Int. J. Mach. Tools. Manuf.* 47 (2007) 263-272.

- [48] W. Grzesik, M. Bartoszek, P. Nieslony, Finite element modelling of temperature distribution in the cutting zone in turning processes with differently coated tools. *J. Mater. Process. Technol.* 164-165 (2005) 1204-1211.
- [49] M.N.A. Nasr, E.-G. Ng, M.A. Elbestawi, Modelling the effects of tool-edge radius on residual stresses when orthogonal cutting AISI 316L, *Int. J. Mach. Tools. Manuf.* 47 (2007) 401-411.
- [50] M.N.A. Nasr, E.-G. Ng, M.A. Elbestawi, Effects of strain hardening and initial yield strength on machining-induced residual stresses. *ASME J. Eng. Mater. Technol.* 129 (2007) 567-579.
- [51] M. Sadeghifar, R. Sedaghati, V. Songmene, FE modeling and optimization of cutting temperature in orthogonal turning, In: 24th International Congress of Theoretical and Applied Mechanics (ICTAM), Montreal, Canada, August 21-26, 2016.
- [52] Y.B. Guo, D.W. Yen, A FEM study on mechanisms of discontinuous chip formation in hard machining, *J. Mater. Process. Technol.* 155-156 (2004) 1350-1356.
- [53] Ch. Hortig, B. Svendsen, Simulation of chip formation during high-speed cutting, *J. Mater. Process. Technol.* 186 (2007) 66-76.
- [54] F. Klocke, D. Lung, S. Buchkremer, I.S. Jawahir, From orthogonal cutting experiments towards easy-to-implement and accurate flow stress data, *Mater. Manuf. Process.* 28 (2013) 1222-1227.
- [55] F. Ducobu, E. Rivière-Lorphèvre, E. Filippi, Numerical contribution to the comprehension of saw-toothed Ti6Al4V chip formation in orthogonal cutting, *Int. J. Mech. Sci.* 81 (2014) 77-87.
- [56] F. Ducobu, E. Rivière-Lorphèvre, E. Filippi, On the introduction of adaptive mass scaling in a finite element model of Ti6Al4V orthogonal cutting, *Simul. Model. Pract. Th.* 53 (2015) 1-14.
- [57] D. Umbrello, R. M'Saoubi, J.C. Outeiro, The influence of Johnson-Cook material constants on finite element simulation of machining of AISI 316L steel, *Int. J. Mach. Tools Manuf.* 47 (2007) 462-470.
- [58] Y. Xi, M. Bermingham, G. Wang, M. Dargusch, Finite Element modeling of cutting force and chip formation during thermally assisted machining of Ti6Al4V alloy, *J. Manuf. Sci. Eng.* 135 (2013) 061014-1:9.
- [59] M. Issa, C. Labergere, K. Saanouni, A. Rassineux, Numerical prediction of thermomechanical field localization in orthogonal cutting, *J. Manuf. Sci. Technol.* 5 (2012) 175-195.

- [60] M. Calamaz, D. Coupard, F. Girot, A new material model for 2D numerical simulation of serrated chip formation when machining titanium alloy Ti-6Al-4V, *Int. J. Mach. Tools Manuf.* 48 (2008) 275-288.
- [61] M. Sima, T. Ozel, Modified material constitutive models for serrated chip formation simulations and experimental validation in machining of titanium alloy Ti-6Al-4V, *Int. J. Mach. Tools Manuf.* 50 (2010) 943-960.
- [62] M. Calamaz, D. Coupard, F. Girot, Numerical simulation of titanium alloy dry machining with a strain softening constitutive law, *Mach. Sci. Technol.* 14 (2010) 244-257.
- [63] M. Calamaz, D. Coupard, M. Nouari, F. Girot, Numerical analysis of chip formation and shear localization processes in machining the Ti-6Al-4V titanium alloy, *Int. J. Adv. Manuf. Technol.* 52 (2011) 887-895.
- [64] F. Klocke, H.-W. Raedt, S. Hoppe, 2D-FEM simulation of the orthogonal high speed cutting process, *Mach. Sci. Technol.* 5 (2001) 323-340.
- [65] W. Jomaa, M. Daoud, V. Songmene, P. Bocher, J.F. Châtelain, Identification and validation of marusich's constitutive law for finite element modeling of high speed, In: *Proceedings of the ASME 2014 International Mechanical Engineering Congress and Exposition IMECE2014*, Montreal, QC, Canada, November 14-20, 2014.
- [66] J. Shi, C.R. Liu, The influence of material models on finite element simulation of machining, *J. Manuf. Sci. Eng.* 126 (2005) 849-857.
- [67] N. Fang, Q. Wu, A comparative study of the cutting forces in high speed machining of Ti-6Al-4V and Inconel 718 with a round cutting edge tool, *J. Mater. Process. Technol.* 209 (2009) 4385-4389.
- [68] M. Daoud, J.F. Chatelain, A. Bouzid, Effect of rake angle on Johnson-Cook material constants and their impact on cutting process parameters of Al2024-T3 alloy machining simulation, *Int. J. Adv. Manuf. Technol.* 81 (2015) 1987-1997.
- [69] A. Nordgren, B. Zargari Samani, R. M'Saoubi, Experimental study and modelling of plastic deformation of cemented carbide tools in turning, In: *6th CIRP International Conference on High Performance Cutting (HPC2014)*, *Procedia CIRP* 14 (2014) 599-604.

- [70] N.A. Abukhshim, P.T. Mativenga, M.A. Sheikh, An investigation of the tool-chip contact length and wear in high-speed turning of EN19 steel, In: Proceedings of the Institution of Mechanical Engineers, Part B: J. Eng. Manuf. 218 (2004) 889-903.
- [71] P. Sartkulvanich, T. Altan, A. Gocmen, Effects of flow stress and friction models in finite element simulation of orthogonal cutting - A sensitivity analysis, Mach. Sci. Technol. 9 (2007) 1-26.
- [72] A.J. Haglund, H.A. Kishawy, R.J. Rogers, An exploration of friction models for the chip-tool interface using an Arbitrary Lagrangian-Eulerian finite element model, Wear 265 (2008) 452-460.
- [73] P. Pres, W. Skoczyński, K. Jaśkiewicz, Research and modeling workpiece edge formation process during orthogonal cutting, Arch. Civil Mech. Eng. 14 (2014) 622-635.
- [74] C. Bonnet, F. Valiorgue, J. Rech, H. Hamdi, Improvement of the numerical modeling in orthogonal dry cutting of an AISI316L stainless steel by the introduction of a new friction model, J. Mater. Process. Technol. 1 (2008) 114-118.
- [75] T.I. El-Wardany, H.A. Kishawy, M.A. Elbestawi, Surface integrity of die material in high speed hard machining, Part 2: microhardness variations and residual stresses, J. Manuf. Sci. Eng. 122 (2000) 632-641.
- [76] C. Maranhao, J. Paulo Davim, Finite element modelling of machining of AISI 316 steel: Numerical simulation and experimental validation, Simul. Model. Pract. Th. 18 (2010) 139-156.
- [77] F. Klocke, S. Rizzuti, P. Frank, K. Gerschwiler, D. Lung, L. Settineri, Experimental and numerical investigation on the delamination behaviour of PVD-coated tools in turning of austenitic steel, Int. J. Mater. Form. 3 (2010) 435-438.
- [78] Y.C. Yen, A. Jain, T. Altan, A finite element analysis of orthogonal machining using different tool edge geometries, J. Mater. Process. Technol. 146 (2004) 72-81.
- [79] L. Qian, M.R. Hossan, Effect on cutting force in turning hardened tool steels with cubic boron nitride inserts, J. Mater. Process. Technol. 191 (2007) 274-278.
- [80] P.L. Menezes, I.V. Avdeev, M.R. Lovell, C.F. Higgs III, An explicit finite element model to study the influence of rake angle and friction during orthogonal metal cutting, Int. J. Adv. Manuf. Technol. 73 (2014) 875-885.

- [81] Y. Long, C. Guo, Finite element modeling of burr formation in orthogonal cutting, *Mach. Sci. Technol.* 16 (2012) 321-336.
- [82] Y.-C. Yen, A. Jain, P. Chigurupati, W.-T. Wu, T. Altan, Computer Simulation of Orthogonal Cutting using a Tool with Multiple Coatings, *Mach. Sci. Technol.* 8 (2004) 305-326.
- [83] T. Ozel, The influence of friction models on finite element simulations of machining, *Int. J. Mach. Tools Manuf.* 46 (2006) 518-530.
- [84] W. Jomaa, V. Songmene, P. Bocher, An hybrid approach based on machining and dynamic tests data for the identification of material constitutive equations, *J. Mater. Eng. Perform.* 25 (2016) 1010-1027.
- [85] E. Ceretti, A. Attanasio, C. Giardini, L. Filice, S. Rizzuti, D. Umbrello, Evaluation of accuracy in 2D and 3D simulation of orthogonal cutting processes, In: *Proceedings of 11th CIRP Conference on modeling of machining operations*, 2008.
- [86] T. Ozel, E. Zeren, Finite element modeling of stresses induced by high speed machining with round edge cutting tools, In: *Proceedings of the ASME 2005 International Mechanical Engineering Congress and Exposition IMECE2005*, Orlando, FL, USA, November 5-11, 2005.
- [87] P. Majumdar, R. Jayaramachandran, S. Ganesan, Finite element analysis of temperature rise in metal cutting processes, *Appl. Therm. Eng.* 25 (2005) 2152-2168.
- [88] L. Filice, D. Umbrello, F. Micari, L. Settineri, On the finite element simulation of thermal phenomena in machining processes, In: *Proceedings of the Eighth ESAFORM Conference*, 729-732, 2005.
- [89] T. Ozel, E. Zeren, Finite element modeling the influence of edge roundness on the stress and temperature fields induced by high-speed machining, *Int. J. Adv. Manuf. Technol.* 35 (2007) 255-267.
- [90] L. Tang, J. Huang, L. Xie, Finite element modeling and simulation in dry hard orthogonal cutting AISI D2 tool steel with CBN cutting tool, *Int. J. Adv. Manuf. Technol.* 53 (2011) 1167-1181.
- [91] P.J. Arrazola, T. Ozel, D. Umbrello, M. Davies, I.S. Jawahir, Recent advances in modelling of metal machining processes, *CIRP Ann. Manuf. Technol.* 62 (2013) 695-718.

- [92] W. Grzesik, *Advanced Machining Processes of Metallic Materials*, Elsevier, Amsterdam, 2008.
- [93] *Surface Integrity in Machining*, Springer, London, 2010.
- [94] D. Ulutan, T. Ozel, Machining induced surface integrity in titanium and nickel alloys: A review, *Int. J. Mach. Tools Manuf.* 51 (2011) 250-280.
- [95] J.C. Outeiro, D. Umbrello, R. M'Saoubi, I.S. Jawahir, Evaluation of present numerical models for predicting metal cutting performance and residual stresses, *Mach. Sci. Technol.* 19 (2015) 183-216.
- [96] N. Stenberg, J. Proudian, Numerical modelling of turning to find residual stresses, In: 14th CIRP Conference on Modeling of Machining Operations (CIRP CMMO), *Procedia CIRP* 8 (2013) 258-264.
- [97] M.N.A. Nasr, E.-G. Ng, M.A. Elbestawi, A modified time-efficient FE approach for predicting machining-induced residual stresses, *Finite Elem. Anal. Des.* 44 (2008) 149-161.
- [98] M. Salio, T. Berruti, G. De Poli, Prediction of residual stress distribution after turning in turbine disks, *Int. J. Mech. Sci.* 48 (2006) 976-984.
- [99] K.C. Ee, O.W. Dillon Jr., I.S. Jawahir, Finite element modeling of residual stresses in machining induced by cutting using a tool with finite edge radius, *Int. J. Mech. Sci.* 47 (2005) 1611-1628.
- [100] V. Schulze, H. Autenrieth, M. Deuchert, H. Weule, Investigation of surface near residual stress states after micro-cutting by finite element simulation, *CIRP Ann. Manuf. Technol.* 59 (2010) 117-120.
- [101] J.C. Outeiro, K.C. Ee, O.W. Dillon Jr., P.C. Wanigarathne, I.S. Jawahir, Some observations on comparing the modelled and measured residual stresses on the machined surface induced by orthogonal cutting of AISI 316L steel, In: 9th CIRP International Workshop on Modeling of Machining Operations, Bled, Slovenia, May 11-12, 2006.
- [102] Z. Pu, D. Umbrello, O.W. Dillon Jr., I.S. Jawahir, Finite element simulation of residual stresses in cryogenic machining of AZ31B Mg alloy, In: 2nd CIRP Conference on Surface Integrity (CSI), *Procedia CIRP* 13 (2014) 282-287.

- [103] N. Yusup, A.M. Zain, S.Z.M. Hashim, Evolutionary techniques in optimizing machining parameters: Review and recent applications, *Expert Syst. Appl.* 39 (2012) 9909-9927.
- [104] A.D. Prete, T. Primo, R. Franchi, Super-Nickel Orthogonal Turning Operations Optimization, In: 14th CIRP Conference on Modeling of Machining Operations (CIRP CMMO), *Procedia CIRP* 8 (2013) 163-168.
- [105] I.W. Park, A. Dornfeld, A study of burr formation processes using the finite element method: Part I, *J. Eng. Mater. Technol.* 122 (2000) 221-228.
- [106] S.H. Rhim, S.I. Oh, Prediction of serrated chip formation in metal cutting process with new flow stress model for AISI 1045 steel, *J. Mater. Process. Technol.* 171 (2006) 417-422.
- [107] D. Umbrello, J. Hua, R. Shivpuri, Hardness-based flow stress and fracture models for numerical simulation of hard machining of AISI 52100 bearing steel, *Mater. Sci. Eng. A* 374 (2004) 90-100.
- [108] J. Hua, R. Shivpuri, X. Cheng, V. Bedekar, Y. Matsumoto, F. Hashimoto, T.R. Watkins, Effect of feed rate, workpiece hardness and cutting edge on subsurface residual stress in the hard turning of bearing steel using chamfer+hone cutting edge geometry, *Mater. Sci. Eng. A* 394 (2005) 238-248.
- [109] K. Liu, S.N. Melkote, Finite element analysis of the influence of tool edge radius on size effect in orthogonal micro-cutting process, *Int. J. Mech. Sci.* 49 (2007) 650-660.
- [110] K.S. Woon, M. Rahman, F.Z. Fang, K.S. Neo, K. Liu, Investigations of tool edge radius effect in micromachining: A FEM simulation approach, *J. Mater. Process. Technol.* 195 (2008) 204-211.
- [111] W.J. Deng, W. Xia, Y. Tang, Finite element simulation for burr formation near the exit of orthogonal cutting, *Int. J. Adv. Manuf. Technol.* 43 (2009) 1035-1045.
- [112] T.D. Marusich, S. Usui, R.J. McDaniel, Three-dimensional finite element prediction of machining-induced stresses, In: Proceedings of the ASME 2003 International Mechanical Engineering Congress and Exposition IMECE2003, Washington, DC, USA, November 15-21, 2003.

- [113] B. Haddag, S. Atlati, M. Nouari, M. Zenasni, Analysis of the heat transfer at the tool-workpiece interface in machining: determination of heat generation and heat transfer coefficients. *Heat Mass Transfer* 51 (2015) 1355-1370.
- [114] M.N.A. Nasr, On modelling of machining-induced residual stresses, PhD Dissertation, McMaster University, Canada, 2007.
- [115] M.R. Movahhedy, M.S. Gadala, Y. Altintas, Simulation of chip formation in orthogonal metal cutting process: An ALE finite element approach, *Mach. Sci. Technol.* 4 (2000) 15-42.
- [116] G. Fang, P. Zeng, Three-dimensional thermo-elastic-plastic coupled FEM simulations for metal oblique cutting processes, *J. Mater. Process. Technol.* 168 (2005) 42-48.
- [117] M. Baker. Finite element simulation of high-speed cutting forces, *J. Mater. Process. Technol.* 176 (2006) 117-126.
- [118] H. Chandrasekaran, R. M'Saoubi, H. Chazal, Modelling of material flow stress in chip formation process from orthogonal milling and split Hopkinson bar tests, *Mach. Sci. Technol.* 9 (2005) 131-145.
- [119] R. M'Saoubi, Aspects Thermiques et Microstructuraux de la coupe. Application a` la coupe orthogonale des aciers auste´ nitiques, PhD Dissertation, Ecole nationale sup´erieure d'arts et m´etiers, France, 1998.
- [120] B. Changeux, M. Touratier, J.L. Lebrun, T. Thomas, J. Clisson, High-speed shear tests for the identification of the Johnson-Cook law, In: Fourth International ESAFORM Conference, Liege, Belgium, April 23-25, 2001.
- [121] N. Tounsi, J. Vincenti, A. Otho, M.A. Elbestawi, From the basics of orthogonal metal cutting toward the identification of the constitutive equation, *Int. J. Mach. Tools Manuf.* 42 (2002) 1373-1383.
- [122] H. Chandrasekeran, D.V. Kapoor, Photoelastic analysis of tool-chip interface stress, *J. Eng. Ind.* 87B (1965) 495-502.
- [123] T.H.C. Childs, M.I. Mahdi, On the stress distribution between the chip and tool during metal turning. *CIRP Ann. Manuf. Technol.* 38 (1989) 55-58.
- [124] Y.B. Guo, C.R. Liu, 3D FEA modeling of hard turning, *J. Manuf. Sci. Eng.* 124 (2002) 189-199.

- [125] J.S. Strenkowski, J.T. Carroll, A finite element model of orthogonal metal cutting. *J. Eng. Ind.* 107 (1985) 349-354.
- [126] P. Lorong, J. Yvonnet, G. Coffignal, S. Cohen, Contribution of computational mechanics in numerical simulation of machining and blanking: State-of-the-Art. *Arch. Comput. Meth. Eng.* 13 (2006) 45-90.
- [127] D.J. Bammann, M.L. Chiesa, G.C. Johnson, Modeling large deformation and failure in manufacturing process, *Th. Appl. Mech.* (1996) 359-376.
- [128] K. Maekawa, T. Shirakashi, E. Usui, Flow stress of low carbon steel at high temperature and strain rate (Part 2) - Flow stress under variable temperature and variable strain rate, *B. Jpn. Soc. Prec. Eng.* 17 (1983) 167-172.
- [129] J. Sartkulvanich, F. Koppka, T. Altan, Determination of flow stress for metal cutting simulation- A progress report, *J. Mater. Process. Technol.* 146 (2004) 61-71.
- [130] V. Schulze, O. Vohringer, Influence of alloying elements on the strain rate and temperature dependence of the flow stress of steels, *Metall. Mater. Trans. A* 31 (2000) 825-830.
- [131] S.H. Rhim, S.I. Oh, Simulation of serrated chip formation in metal cutting process by using a new flow stress model, *CIRP January Meeting, Paris, 2002.*
- [132] S.H. Rhim, S.I. Oh, Prediction of serrated chip formation in metal cutting process, In: *US-Korea Workshop on Advance in Metallic Structural Materials, Hawaii, 2003.*
- [133] D.J. Bammann, Modeling temperature and strain rate dependent large deformation of metals, *Appl. Mech. Rev.* 43 (1990) 312-319.
- [134] Y. Huang, S.Y. Liang, Cutting forces modeling considering the effect of tool thermal property-application to CBN hard turning, *Int. J. Mach. Tools Manuf.* 43 (2003) 307-315.
- [135] J.O. Hallquist, *LS-DYNA theory manual*, Livermore Software Technology Corporation, USA, 2006.
- [136] J. Lemaitre, How to use damage mechanics, *Nucl. Eng. Des.* 80 (1984) 233-245.
- [137] F. Kara, K. Aslantas, A. Cicek, Prediction of cutting temperature in orthogonal machining of AISI316L using artificial neural network, *Appl. Soft Comput.* 38 (2016) 64-74.

- [138] J. Hua, D. Umbrello, R. Shivpuri, Investigation of cutting conditions and cutting edge preparations for enhanced compressive subsurface residual stress in the hard turning of bearing steel, *J. Mater. Process. Technol.* 171 (2006) 180-187.
- [139] M. Sadeghifar, R. Sedaghati, W. Jomaa, V. Songmene, Finite element analysis and response surface method for robust multi-performance optimization of radial turning of hard 300M steel, In press, *Int. J. Adv. Manuf. Technol.*, DOI: 10.1007/s00170-017-1032-4, 2017.
- [140] W. Jomaa, O. Mechri, J. Lévesque, V. Songmene, P. Bocher, A. Gakwaya, Finite element simulation and analysis of serrated chip formation during high-speed machining of AA7075-T651 alloy, *J. Manuf. Process.* 26 (2017) 446-458.
- [141] Abaqus/Explicit User's Manual, Version 6.11, 2011.
- [142] W. Jomaa, Contributions to understanding the high speed machining effects on aeronautic part surface integrity, PhD Dissertation, École de technologie supérieure, Canada, 2015.
- [143] Nicolas Barth, X-Ray Diffraction, University of California, Santa Barbara, 2007.
- [144] P.S. Prevéy, X-ray diffraction residual stress techniques, Lambda Research, Inc., 1986.
- [145] M.E. Fitzpatrick, A.T. Fry, P. Holdway, F.A. Kandil, J. Shackleton, L. Suominen, Measurement good practice guide No. 52: Determination of residual stresses by X-ray diffraction - Issue 2, National Physical Laboratory, 2005.
- [146] Proto residual stress analyzer: Theory of operational manual, Proto Manufacturing Limited, Version 4.7, 1999.
- [147] K. Hiratsuka, T. Sasaki, K. Seki, Y. Hirose, Development of measuring system for stress by means of image plate for laboratory X-ray experiment, *Int. Centre Diffr. Data - Advances in X-ray analysis* 46 (2003) 61-67.
- [148] User's manual for  $\mu$ -X360, First Ed., Pulstec Industrial Co., Ltd., Japan, 2013.
- [149] <http://www.olympus-ims.com/en/knowledge/metrology/roughness/> - 2017/07/09.
- [150] Y.B. Gianchandani, S.B. Crary, Parametric modeling of a microaccelerometer: Comparing I- and D-optimal design of experiments for finite element analysis, *J. Microelectromech. Syst.* 7 (1998) 274-282.

- [151] M. Sadeghifar, M. Bagheri, A.A. Jafari, Multiobjective optimization of orthogonally stiffened cylindrical shells for minimum weight and maximum axial buckling load, *Thin Wall. Struct.* 48 (2010) 979-988.
- [152] J.S. Arora, *Introduction to optimum design*, Third Ed., Elsevier, 2012.
- [153] R. Fletcher, *Practical methods of optimization*, John Wiley and Sons, 1987.
- [154] P.E. Gill, W. Murray, M.H. Wright, *Practical Optimization*, London, Academic Press, 1981.
- [155] *Aerospace Structural Metals handbook*, 1987.
- [156] <http://www.azom.com> - 2017/03/20.
- [157] V.A.A. Godoy, A.E. Diniz, Turning of interrupted and continuous hardened steel surfaces using ceramic and CBN cutting tools, *J. Mater. Process. Technol.* 211 (2011) 1014-1025.
- [158] S. Lin, F. Peng, Y. Liu, S. Yang, R. Yan, Finite element research on cutting force and temperature in milling 300M steel, In: *Proceedings of the 6th International Conference on Intelligent Robotics and Applications (ICIRA)*, Busan, South Korea, 481-490, 2013.
- [159] W. Jomaa, V. Songmene, P. Bocher, An investigation of machining-induced residual stresses and microstructure of induction-hardened AISI 4340 steel, *Mater. Manuf. Process.* 31 (2016) 838-844.
- [160] M. Khajezadeh, M. Akhlaghi, M. R. Razfar, Finite element simulation and experimental investigation of tool temperature during ultrasonically assisted turning of aerospace aluminum using multicoated carbide inserts, *Int. J. Adv. Manuf. Technol.* 75 (2014) 1163-1175.
- [161] R.S. Pawade, S.S. Joshi, P.K. Brahmkar, Effect of machining parameters and cutting edge geometry on surface integrity of high-speed turned Inconel 718, *Int. J. Mach. Tools. Manuf.* 48 (2008) 15-28.